UPPSALA
UNIVERSITET

Digital Comprehensive Summaries of Uppsala Dissertations from the Faculty of Science and Technology 2067

Selfconsistent theory of superconductivity in unconventional superconductors

FABIAN SCHRODI

ACTA
UNIVERSITATIS
UPSALIENSIS
UPPSALA
2021

ISSN 1651-6214
ISBN 978-91-513-1278-1
URN urn:nbn:se:uu:diva-451373

Dissertation presented at Uppsala University to be publicly examined in Å4001, Ångströmlaboratoriet, Lägerhyddsvägen 1, Uppsala, Friday, 22 October 2021 at 13:15 for the degree of Doctor of Philosophy. The examination will be conducted in English. Faculty examiner: Professor Jörg Schmalian (Karlsruhe Institute of Technology (KIT)).

Zoom-Link for the defense: https://uu-se.zoom.us/j/66803247841

Abstract

Schrodi, F. 2021. Selfconsistent theory of superconductivity in unconventional superconductors. *Digital Comprehensive Summaries of Uppsala Dissertations from the Faculty of Science and Technology* 2067. 126 pp. Uppsala: Acta Universitatis Upsaliensis. ISBN 978-91-513-1278-1.

Superconductivity is broadly believed to stem from either electron-phonon interaction (EPI) or from purely electronic mechanisms, such as antiferromagnetic spin fluctuations. For many materials the discussion about which of these interactions is the dominant "pairing glue" is still ongoing. This is particularly the case for unconventional superconductors, such as the high-T_c cuprates, where the origin of superconductivity is still not known after 30 years of intense research.

This thesis, which is split into two parts, aims at contributing to unveiling the role of these Cooper pairing mediators in unconventional superconductors by applying a powerful state-of-the-art method, self-consistent calculations on the basis of Eliashberg's theory.

In the first part we employ Eliashberg theory under Migdal's approximation for the electron-phonon interaction, and apply a similar level of approximation for spin fluctuations. For monolayer FeSe on $SrTiO_3$, the record holder for T_c in Fe-based superconductors, we show that EPI is responsible for the large critical temperature and key spectral features, while spin fluctuations induce an unconventional symmetry of the superconducting order parameter. For the recently discovered superconductor Twisted Bilayer Graphene we explain the main characteristics of the superconducting state by assuming isotropic EPI, and predict various spectral features, which are expected to be measurable in tunneling experiments. We further discuss superconductivity in high-pressure materials as atomic metallic hydrogen and LaH_{10}, introduce a numerical method for making Eliashberg calculations more efficient, and give an overview of possible effects due to phonon renormalization.

The second part of the thesis emphasizes the role of EPI in unconventional superconductors. By deriving a self-consistent set of Eliashberg equations beyond Migdal's approximation, we show that isotropic EPI causes unconventional symmetries of the superconducting gap in three representative examples, the Fe-based, cuprate and heavy fermion superconductors. Therefore, our results prove that unconventional order parameters are not a sufficient criterion to assume purely electronic mechanisms, and establish conventional EPI as potential mediator of superconductivity. With the Fe-based compound ThFeAsN we identify a real physical system in which such effects might play an important role. We conclude by presenting an induced subordinate odd-frequency superconducting state that coexists with its primary even-frequency counterpart, solely due to vertex corrections beyond Migdal's approximation in a cuprate model system.

Keywords: superconductivity, unconventional, Eliashberg theory

Fabian Schrodi, Department of Physics and Astronomy, Materials Theory, Box 516, Uppsala University, SE-751 20 Uppsala, Sweden.

© Fabian Schrodi 2021

ISSN 1651-6214
ISBN 978-91-513-1278-1
URN urn:nbn:se:uu:diva-451373 (http://urn.kb.se/resolve?urn=urn:nbn:se:uu:diva-451373)

To my parents and brothers

List of papers

This thesis is based on the following papers, which are referred to in the text by their Roman numerals.

I **Self-consistent temperature dependence of quasiparticle bands in monolayer FeSe on $SrTiO_3$**
Fabian Schrodi, Alex Aperis and Peter M. Oppeneer
*Physical Review B **98**, 094509 (2018).*

II **Eliashberg theory for spin fluctuation mediated superconductivity: Application to bulk and monolayer FeSe**
Fabian Schrodi, Alex Aperis and Peter M. Oppeneer
*Physical Review B **102**, 014502 (2020).*

III **Multichannel superconductivity of monolayer FeSe on $SrTiO_3$: Interplay of spin fluctuations and electron-phonon interaction**
Fabian Schrodi, Alex Aperis and Peter M. Oppeneer
*Physical Review B **102**, 180501(R) (2020).*

IV **Prominent Cooper Pairing Away From the Fermi Level and its Spectroscopic Signature in Twisted Bilayer Graphene**
Fabian Schrodi, Alex Aperis and Peter M. Oppeneer
*Physical Review Research **2**, 012066(R) (2020).*

V **Cascade of replica bands in flat band systems: predictions for twisted bilayer graphene**
Fabian Schrodi, Alex Aperis and Peter M. Oppeneer
*Physical Review B **103**, 144505 (2021).*

VI **Phonon-mode specific contributions to room-temperature superconductivity in atomic hydrogen at high pressures**
Ashok K. Verma, P. Modak, Fabian Schrodi, Alex Aperis and Peter M. Oppeneer
*Physical Review B **103**, 094505 (2021).*

VII **Prediction of unusual trigonal phase of superconducting LaH_{10} stable from 250 to 425 GPa pressure**
Ashok K. Verma, P. Modak, Fabian Schrodi, Alex Aperis and Peter M. Oppeneer
arXiv:2107.04776 (2021).

VIII **Increased performance of Matsubara space calculations: A case study within Eliashberg theory**
Fabian Schrodi, Alex Aperis and Peter M. Oppeneer
*Physical Review B **99**, 184508 (2019).*

IX **Influence of phonon renormalization in Eliashberg theory for superconductivity in two- and three-dimensional systems**
Fabian Schrodi, Alex Aperis and Peter M. Oppeneer
*Physical Review B **103**, 064511 (2021).*

X **Full-bandwidth Eliashberg theory of superconductivity beyond Migdal's approximation**
Fabian Schrodi, Peter M. Oppeneer and Alex Aperis
*Physical Review B **102**, 024503 (2020) – editor's suggestion.*

XI **Unconventional superconductivity mediated solely by isotropic electron-phonon interaction**
Fabian Schrodi, Peter M. Oppeneer and Alex Aperis
arXiv:2106.12319 (2021).

XII **Exploring multichannel superconductivity in ThFeAsN**
Fabian Schrodi, Fairoja Cheenicode-Kabeer, Alex Aperis and Peter M. Oppeneer
arXiv:2103.16928 (2021).

XIII **Induced odd-frequency superconducting state in vertex-corrected Eliashberg theory**
Fabian Schrodi, Alex Aperis and Peter M. Oppeneer
arXiv:2108.08124 (2021).

Reprints were made with permission from the publishers.

Author's contributions

In most of the above Papers I performed all computations and the subsequent numerical analyses, namely in Papers I, II, III, IV, V, VIII, IX, X, XI and XIII. In Papers VI, VII and XII I carried out the superconductivity calculations. I contributed the part about superconductivity in Papers VI and VII, wrote the first draft in each of Papers IV, V, X and XI, and was the main contributor in the writing process of Papers I, II, III, VIII, IX, XII and XIII. Papers VIII, IX and XIII were developed on basis of my own ideas.

Contents

1 Introduction 9

2 Theoretical background 13
  2.1 Eliashberg theory 13
    2.1.1 Derivation under Migdal's approximation 13
    2.1.2 Spectral properties 18
  2.2 Simplified approaches 21
    2.2.1 Fermi surface restricted Eliashberg theory 22
    2.2.2 Isotropic Eliashberg theory 23
    2.2.3 Linearized Eliashberg theory 23
    2.2.4 McMillan equation for T_c 24
    2.2.5 BCS theory 25

Part I: Applications of Eliashberg theory 27

3 Monolayer FeSe on $SrTiO_3$ 29
  3.1 Electron-phonon interactions 31
  3.2 Spin fluctuations 35
    3.2.1 Superconductivity in bulk FeSe 35
    3.2.2 Spin fluctuations in FeSe/STO 38
  3.3 Multichannel superconductivity 42

4 Twisted bilayer graphene 45
  4.1 Superconductivity from electron-phonon interaction 46
  4.2 Replica bands 49

5 Additional examples 53
  5.1 Atomic hydrogen 53
  5.2 A new trigonal phase in LaH_{10} 56
  5.3 Reducing the computational costs 58
  5.4 Phonon renormalization 61

Part II: Vertex-corrected Eliashberg theory 67

6 Formalism and exploration 69
  6.1 Extended Eliashberg theory 69
    6.1.1 First and second order Feynman diagrams 69
    6.1.2 Levels of approximation 72
    6.1.3 Numerical solution 76

6.2 Phase space exploration 79

7 Exotic superconducting states 85
  7.1 Unconventional superconducting gap 85
    7.1.1 System properties and self-consistent solutions 86
    7.1.2 Deeper analysis of the superconducting state 90
  7.2 The case of ThFeAsN 94
  7.3 Odd-frequency superconductivity 99
    7.3.1 Further theoretical extension 99
    7.3.2 Odd-frequency state in a cuprate superconductor 102

8 Conclusions and outlook 105

Popular science summary 108

Populärvetenskaplig sammanfattning 111

Populärwissenschaftliche Zusammenfassung 114

Acknowledgments 117

References 118

1. Introduction

Superconductivity is a macroscopic phenomenon that can occur in certain types of materials upon sufficient cooling. When the temperature is smaller than the superconductor's critical temperature T_c, the material looses its electric resistance as was first discovered in mercury [1]. Microscopically, pairs of electrons feel an attractive force via an exchange boson that overcomes their Coulomb repulsion, leading to the formation of so-called Cooper pairs. In contrast to single electrons, Cooper pairs behave like bosons which allows for a collective condensation into a macroscopic ground state. It follows that all Cooper pairs can be described by a single collective wave function governing their microscopic behavior in the superconductor. For the condensate as a whole it is energetically favorable to avoid single-particle scattering, which explains the absence of resistivity in the superconducting state.

A remarkable property of superconductors, which is often used to rigorously certify the existence of a superconducting state, is the Meissner effect [2]: Below the critical temperature external magnetic fields are expelled from the material, making superconductors perfect diamagnets. Once the temperature is increased above T_c, the magnetic field lines can penetrate the material, which marks the phase transition to the normal state. Another indicator for superconductivity in a material is the opening of an energy gap Δ in the electronic dispersion. This gap is characteristic for each material with respect to its magnitude and symmetry in reciprocal space, and it will be a recurrent property of interest throughout this thesis.

The first successful microscopic theory of superconductivity was introduced by Bardeen, Cooper and Schrieffer, the so-called BCS theory [3]. By assuming weak electron-phonon interaction (EPI) it was possible to explain the ground state of conventional, mostly elemental superconductors. In these systems the characteristic ratio Δ/k_BT_c is close to 1.76, and the gap function has plain s-wave symmetry in reciprocal space. It should further be noted that the BCS formalism is a static mean-field theory, i.e. it does not take into account the time delay of the two Cooper pair electrons that occurs upon exchange of a boson. The dynamical extension of BCS theory, i.e. including time retardation, was done briefly after, triggered by the milestone work by Migdal on EPI in metals, where he introduced his famous theorem [4]. Eliashberg applied these very ideas to the superconducting state, thereby developing what came to be known as Migdal-Eliashberg theory [5]. It is worth noting that, from these advances, an approximate closed expression for the superconducting critical temperature has been derived by McMillan [6], for which different extensions have been proposed subsequently [7, 8].

Needless to say, the development of theories for superconductors was driven by experimental discoveries, and it is worth mentioning the findings that are relevant for this thesis. In the early days of superconductivity research, most known examples were elemental and/or weak coupling superconductors. These materials are well explained by BCS theory and the McMillan equation [9]. There is consensus that EPI is the driving mediator of Cooper pairing in this class of 'conventional' superconductors. As concerns the gap symmetry, these materials show relatively isotropic s-wave spin-singlet pairing. Over the years the highest possible values for T_c within this class of materials increased, but they are nevertheless considered being low temperature superconductors.

About half a century after the discovery of superconductivity the first so-called heavy-fermion superconductor $CeCu_2Si_2$ came into the picture [10]. Even though these rare-earth compounds exhibited very low critical temperatures, they appeared puzzling to theorists due to the inexplicable sign change of the superconducting order parameter on the Fermi surface (FS). This 'unconventional' superconductivity could not be understood with the attractive isotropic EPI in BCS theory, which is why the concept of purely electronic mechanisms for superconductivity was introduced, with the most famous example being antiferromagnetic spin fluctuations [11, 12]. In these theories the interaction is repulsive and, given sufficiently coherent FS nesting conditions which leads to a strongly peaked electronic susceptibility, it can produce a sign change of Δ on the FS [13, 14].

A few years later the theory of spin fluctuations became extremely popular upon the discovery of high-T_c cuprate superconductors, exceeding transition temperatures of 100 K [15]. Many of these compounds showed unconventional Cooper pairing and additionally they were found, just like the heavy-fermion compounds, in close vicinity of magnetism [16]. This led to the common conception that unconventional superconductivity is mediated by electronic mechanisms. More recently this believe has been strengthened by the family of Fe-based compounds, which similarly exhibit high transition temperatures and unconventional superconducting gap symmetries [17].

In the meantime it was realized that applying high pressure to hydrogen-rich compounds, so-called (super)hydrides, can drastically increase the critical temperature. Examples of this family of high temperature superconductors are the recently discovered LaH_{10} with $T_c \simeq 250\,\mathrm{K}$ at $170\,\mathrm{GPa}$ pressure [18] and a carbonaceous sulfur hydride, which is the current record holder of highest $T_c \simeq 15^\circ\mathrm{C}$ at approximately $270\,\mathrm{GPa}$ [19]. Hydrides show conventional s-wave symmetry of the order parameter and EPI is generally accepted as the dominant mediator of superconductivity. However, these compounds fall into the strong coupling regime which requires to go beyond BCS theory to describe the superconducting state accurately.

The papers summarized in this thesis touch upon many of the above mentioned topics. Some of the works were very materials specific, where we tried to explain superconductivity with EPI, antiferromagnetic spin fluctuations, or both of these mediators on the same footing. We explicitly considered the Fe-based compounds bulk FeSe, monolayer FeSe on a $SrTiO_3$ substrate and ThFeAsN, the hydrides atomic metallic hydrogen and LaH_{10}, as well as the heavy-fermion superconductor $CeCoIn_5$. Other studies were performed for model systems representative for whole families of compounds, e.g. cuprate, Fe-based and Holstein like systems.

Another dimension of the presented work is that of method development. Here, to describe the superconducting state of a given system we almost exclusively use Eliashberg theory. We introduce different extensions to this formalism that go beyond standard approximations and methodology. For example, we put forward an analytic tail scheme to reduce the computational costs of Matsubara space calculations, developed a sophisticated formalism to consider spin and charge fluctuations in Eliashberg theory, and studied the effect of phonon renormalization. Most notably, our extended Eliashberg equations obtained by fully self-consistently including vertex corrections beyond Migdal's approximation are unprecedented and provide surprising new insights.

Structure of the thesis

In the following Chapter 2 we go through the details of Migdal-Eliashberg theory by deriving the self-consistent Eliashberg equations under Migdal's approximation. It is shown how to compute spectral properties that can be compared to different kinds of experiment. We continue by applying various approximations that lead to a simplified version of Eliashberg equations. Further we review the famous BCS theory, as well as the McMillan equation for T_c. This chapter provides the theoretical foundation for Part I of the thesis, and introduces concepts and terminology also relevant for Part II.

In Part I we discuss the projects in which we used the standard Eliashberg formalism or extensions of it that fall into the same category. The first material under consideration is monolayer FeSe on a $SrTiO_3$ substrate, Chapter 3, a high-T_c superconductor in which the pairing mechanism is still under debate. In Section 3.1 we discuss the results of Paper I, where we assumed EPI as mediator of superconductivity. As an alternative approach we introduce a new formalism to include spin and charge fluctuations into a full bandwidth Eliashberg framework in Section 3.2. Following the key results of Paper II, we benchmark our method successfully with bulk FeSe and afterwards apply it to the monolayer case. Paper III and Section 3.3 are the natural next step of these earlier advances, in that we combine EPI with the purely electronic mechanism into a multichannel framework to study their interplay in monolayer FeSe.

We continue in Chapter 4 by exploring the effects of EPI on the interacting state of Twisted Bilayer Graphene. The findings of Paper IV are discussed in Section 4.1, where we focus on the superconducting state in this system. In Section 4.2 we introduce the phenomenon of replica bands in flat band systems with Twisted Bialyer Graphene as an explicit example, which is the content of Paper V.

In the next Chapter 5 we summarize additional somewhat isolated projects that fall under the umbrella of standard Eliashberg theory. In Section 5.1 we touch upon the topic of high pressure superconductivity by discussing atomic metallic hydrogen and its superconducting properties (Paper VI). Next, from Paper VII we discuss our prediction of a new structural phase in the high temperature superconductor LaH_{10} in Section 5.2. Afterwards we address the topic of reducing the computational costs of solving Eliashberg equations, and of Matsubara space calculations more generally. To do so we introduce the analytic tail scheme from Paper VIII in Section 5.3. We end this Chapter with Section 5.4, in which we give an overview of effects that can occur upon self-consistent inclusion of phonon renormalization in the Eliashberg framework, which usually is neglected, and show various results from Paper IX.

The following Part II of the thesis contains theoretical and numerical results for vertex-corrected Eliashberg theory, i.e. a self-consistent version of the Eliashberg equations that goes beyond Migdal's so-called adiabatic approximation.

In Chapter 6 we formally introduce the theory and method, starting by deriving the nonadiabatic Eliashberg equations and different simplifications thereof in Section 6.1. Additionally we comment on important computational aspects needed for obtaining numerical results efficiently. The phase space exploration of Paper X, which was done with respect to electron-phonon coupling strength, dimensionality of the system and the degree of nonadiabaticity, is presented in Section 6.2.

Different rather unusual phenomena can occur due to vertex corrections and we present those in Chapter 7. As we have shown in Paper XI, isotropic EPI can lead to unconventional symmetries of the superconducting gap in Fe-based, cuprate and heavy-fermion superconductors. This proves that unconventional symmetries can be induced solely by the conventional EPI and are not necessarily a signature of an electronic pairing mechanism. We summarize our model studies in Section 7.1, and argue in Section 7.2 that ThFeAsN is a likely candidate for this scenario, as was put forward in Paper XII. Unexpectedly, vertex corrections can also lead to a coexistence of even- and odd-frequency superconductivity, see Paper XIII. A slight extension of the theory and a benchmark result is presented in Section 7.3.

The final Chapter 8 gives a very short summary of all results of this thesis and their significance for the field. Lastly, we comment on possible future directions and extensions of the work.

2. Theoretical background

> *Everything is complicated if no one explains it to you.*
>
> Fredrik Backman

Here we provide the basic theory needed to understand the remaining chapters and papers of this thesis. We introduce the Migdal-Eliashberg theory in Section 2.1 and briefly discuss the commonly employed BCS formalism in Section 2.2.5, while we mainly used the former in our work.

As mentioned in the Introduction, we want to describe superconductivity on a microscopic level. Concerning the mediator of Cooper pairing, we focus on a simple model of electron-phonon interactions (EPI), meaning that we assume an interaction $g_{\mathbf{q},\nu}$ with momentum $\mathbf{q}$ and phonon branch ν. We further use a one-band electron dispersion $\xi_{\mathbf{k}}$ for spin-singlet electrons, and phonon frequencies $\omega_{\mathbf{q},\nu}$. The generalization to multiple energy bands is straightforward, and the interested reader is referred to our papers. The main focus lies on EPI as bosonic mediator of superconductivity, but other mechanisms such as antiferromagnetic spin fluctuations can similarly cause Cooper pairing. Even though we will not go into detail with respect to other bosons, we comment on it where appropriate.

2.1 Eliashberg theory

We start by giving an overview of the Migdal-Eliashberg formalism as it is commonly used. The most general equations in this context, that take into account the full electron bandwidth, are derived in Section 2.1.1. The solutions on the imaginary frequency axis can be analytically continued in a self-consistent way, which is the topic of Section 2.1.2. We continue by showing different levels of approximation to Eliashberg theory, as they are broadly used, in Section 2.2.

2.1.1 Derivation under Migdal's approximation

Electrons moving in a lattice of atoms can be described by a Hamiltonian $H = H_{\mathrm{el}} + H_{\mathrm{el-ph}} + H_{\mathrm{ph}} + H_{\mathrm{C}}$. Here H_{el} is the non-interacting electronic part,

H_{ph} is a sum over microscopic harmonic oscillators describing the lattice vibrations, $H_{\text{el-ph}}$ describes the interaction between lattice and electrons, and H_{C} is the electron Coulomb repulsion. Let us denote $c^\dagger_{\mathbf{k},\sigma}$ and $c_{\mathbf{k},\sigma}$ as creation and annihilation operators of electrons with momentum $\mathbf{k}$ and spin $\sigma \in \{\uparrow,\downarrow\}$. Further, let $\xi_{\mathbf{k}}$ be the electronic energy dispersion and $V^{\text{C}}_{\mathbf{q}}$ the Coulomb interaction. The lattice is described in terms of phonon creation ($b^\dagger_{\mathbf{q},\nu}$) and annihilation ($b_{\mathbf{q},\nu}$) operators, with frequencies $\omega_{\mathbf{q},\nu}$ where ν is a phonon branch index. By modeling the electron-phonon scattering via $g_{\mathbf{q},\nu}$, $\mathbf{q} = \mathbf{k} - \mathbf{k}'$, we can write the full Hamiltonian as

$$\begin{aligned} H =& \sum_{\mathbf{k},\sigma} \xi_{\mathbf{k}} c^\dagger_{\mathbf{k},\sigma} c_{\mathbf{k},\sigma} + \sum_{\mathbf{k},\sigma}\sum_{\mathbf{q},\nu} g_{\mathbf{q},\nu} c^\dagger_{\mathbf{k}-\mathbf{q},\sigma} c_{\mathbf{k},\sigma} \big(b^\dagger_{\mathbf{q},\nu} + b_{\mathbf{q},\nu}\big) \\ &+ \sum_{\mathbf{q},\nu} \omega_{\mathbf{q},\nu} \big(b^\dagger_{\mathbf{q},\nu} b_{\mathbf{q},\nu} + \frac{1}{2}\big) + \sum_{\mathbf{k},\mathbf{k}',\mathbf{q}} \sum_{\sigma,\sigma'} c^\dagger_{\mathbf{k}+\mathbf{q},\sigma} c^\dagger_{\mathbf{k}'+\mathbf{q},\sigma'} V^{\text{C}}_{\mathbf{q}} c_{\mathbf{k}',\sigma'} c_{\mathbf{k},\sigma}. \end{aligned} \tag{2.1}$$

The spin degree of freedom in Eq. (2.1) can be hidden in so-called Nambu spinors, $\Psi^\dagger_{\mathbf{k}} = (c^\dagger_{\mathbf{k},\uparrow}, c_{-\mathbf{k},\downarrow})$ [20], leading to[1]

$$\begin{aligned} H =& \sum_{\mathbf{k}} \xi_{\mathbf{k}} \Psi^\dagger_{\mathbf{k}} \hat{\rho}_3 \Psi_{\mathbf{k}} + \sum_{\mathbf{k}}\sum_{\mathbf{q},\nu} g_{\mathbf{q},\nu} u_{\mathbf{q},\nu} \Psi^\dagger_{\mathbf{k}'} \hat{\rho}_3 \Psi_{\mathbf{k}} \\ &+ \sum_{\mathbf{q},\nu} \hbar\omega_{\mathbf{q},\nu} \big(b^\dagger_{\mathbf{q},\nu} b_{\mathbf{q},\nu} + \frac{1}{2}\big) + \sum_{\mathbf{k},\mathbf{k}',\mathbf{q}} \Psi^\dagger_{\mathbf{k}'} \hat{\rho}_3 \Psi^\dagger_{\mathbf{k}'} V^{\text{C}}_{\mathbf{q}} \Psi_{\mathbf{k}} \hat{\rho}_3 \Psi_{\mathbf{k}}. \end{aligned} \tag{2.2}$$

As a next step we write the electron operators (and implicitly the Nambu spinors) in the Heisenberg picture

$$c_{\mathbf{k},\sigma}(\tau) = e^{H\tau} c_{\mathbf{k},\sigma} e^{-H\tau}, \tag{2.3}$$

with imaginary time $\tau = it$. We can now use the similarity of Eq. (2.3) to grand canoncial thermal averages, governed by the factor $e^{-\beta H}$ where β is the inverse temperature [8]. The imaginary time τ is defined in a range $[-\beta, \beta]$, while the generalized 2×2 matrix Green's function of the system can be expressed as

$$\begin{aligned} \hat{G}_{\mathbf{k}}(\tau) &= -\begin{pmatrix} \langle T_\tau c_{\mathbf{k},\uparrow}(\tau) c^\dagger_{\mathbf{k},\uparrow}(0)\rangle & \langle T_\tau c_{\mathbf{k},\uparrow}(\tau) c_{-\mathbf{k},\downarrow}(0)\rangle \\ \langle T_\tau c^\dagger_{-\mathbf{k},\downarrow}(\tau) c^\dagger_{\mathbf{k},\uparrow}(0)\rangle & \langle T_\tau c^\dagger_{-\mathbf{k},\downarrow}(\tau) c_{-\mathbf{k},\downarrow}(0)\rangle \end{pmatrix} \\ &= -\langle T_\tau \Psi_{\mathbf{k}}(\tau) \Psi^\dagger_{\mathbf{k}}(0)\rangle, \end{aligned} \tag{2.4}$$

---

[1] The Nambu spinors span a 2×2 matrix space in which we can choose the basis as Pauli matrices:

$$\hat{\rho}_0 = \begin{pmatrix} 1 & 0 \\ 0 & 1 \end{pmatrix}, \quad \hat{\rho}_1 = \begin{pmatrix} 0 & 1 \\ 1 & 0 \end{pmatrix}, \quad \hat{\rho}_2 = \begin{pmatrix} 0 & -i \\ i & 0 \end{pmatrix}, \quad \hat{\rho}_3 = \begin{pmatrix} 1 & 0 \\ 0 & -1 \end{pmatrix}.$$

with T_τ the Wick time ordering operator. The periodicity property $\hat{G}_{\mathbf{k}}(\tau+\beta)=-\hat{G}_{\mathbf{k}}(\tau)$ can be used to define $\hat{G}$ also outside $[-\beta,\beta]$ [8].

The off-diagonal terms in Eq. (2.4) are associated with superconductivity, while the diagonal entries describe the 'standard' quasiparticle spectrum. From the above-mentioned periodicity of the τ-dependent Green's function it is convenient to express $\hat{G}_{\mathbf{k}}(\tau)$ in terms of its Fourier components:

$$\hat{G}_{\mathbf{k}}(\tau)=T\sum_m e^{-i\omega_m\tau}\hat{G}_{\mathbf{k},m}. \tag{2.5}$$

Here we use the notation $f_{\mathbf{k},m}=f_{\mathbf{k}}(i\omega_m)$ for brevity, to write the dependence on fermionic Matsubara frequencies $\omega_m=\pi T(2m+1)$, and any sum over index m is to be understood as $\sum_{m=-\infty}^{\infty}$. By inverting Eq. (2.5) we get

$$\hat{G}_{\mathbf{k},m}=\frac{1}{2}\int_{-\beta}^{\beta}\mathrm{d}\tau e^{i\omega_m\tau}\hat{G}_{\mathbf{k}}(\tau). \tag{2.6}$$

In the simplest case of a non-interacting system, where only H_{el} has to be considered in Eq. (2.6), it can be shown that $\hat{G}^0_{\mathbf{k},m}=[i\omega_m\hat{\rho}_0-\xi_{\mathbf{k}}\hat{\rho}_3]^{-1}$, i.e. the quasiparticle spectrum is only given by the poles due to the electron energies.

When considering the fully interacting system, the electron Green's function can be determined by the Dyson equation shown in Fig. 2.1(a), which translates to $\hat{G}_{\mathbf{k},m}=\hat{G}^0_{\mathbf{k},m}+\hat{G}^0_{\mathbf{k},m}\hat{\Sigma}_{\mathbf{k},m}\hat{G}_{\mathbf{k},m}$. Solving this relation for the inverse Green's function gives

$$\hat{G}^{-1}_{\mathbf{k},m}=[\hat{G}^0_{\mathbf{k},m}]^{-1}-\hat{\Sigma}_{\mathbf{k},m}, \tag{2.7}$$

where $\hat{\Sigma}_{\mathbf{k},m}$ is the electron self-energy. Within the 2×2 Nambu formalism employed here, the most general form of $\hat{\Sigma}_{\mathbf{k},m}$ may be expressed as

$$\hat{\Sigma}_{\mathbf{k},m}=i\omega_m(1-Z_{\mathbf{k},m})\hat{\rho}_0+\chi_{\mathbf{k},m}\hat{\rho}_3+\phi_{\mathbf{k},m}\hat{\rho}_1+\zeta_{\mathbf{k},m}\hat{\rho}_2, \tag{2.8}$$

where $Z_{\mathbf{k},m}$ is the electron mass renormalization, $\chi_{\mathbf{k},m}$ acts as a chemical potential, and $\phi_{\mathbf{k},m}$ is the superconductivity order parameter. Particularly, this means that $\phi_{\mathbf{k},m}\neq 0$ in the superconducting state, and $\phi_{\mathbf{k},m}=0$ for $T>T_c$. The role of $\zeta_{\mathbf{k},m}$ on the other hand depends on the approach we are using, as will become clear below. Next we insert Eq. (2.8) into Eq. (2.7), which leads to the electron Green's function

$$\hat{G}_{\mathbf{k},m}=\left[i\omega_m Z_{\mathbf{k},m}\hat{\rho}_0+(\xi_{\mathbf{k}}+\chi_{\mathbf{k},m})\hat{\rho}_3+\phi_{\mathbf{k},m}\hat{\rho}_1+\zeta_{\mathbf{k},m}\hat{\rho}_2\right]\Theta^{-1}_{\mathbf{k},m}, \tag{2.9a}$$

$$\Theta_{\mathbf{k},m}=\left[i\omega_m Z_{\mathbf{k},m}\right]^2-\left[\xi_{\mathbf{k}}+\chi_{\mathbf{k},m}\right]^2-\phi^2_{\mathbf{k},m}-\zeta^2_{\mathbf{k},m}. \tag{2.9b}$$

To proceed we need to dedicate some comments to the phonon and electron self-energies. Starting with the latter, we note that Eq. (2.8) is only a matrix decomposition of $\hat{\Sigma}_{\mathbf{k},m}$, i.e. a definition. However, Migdal has shown that

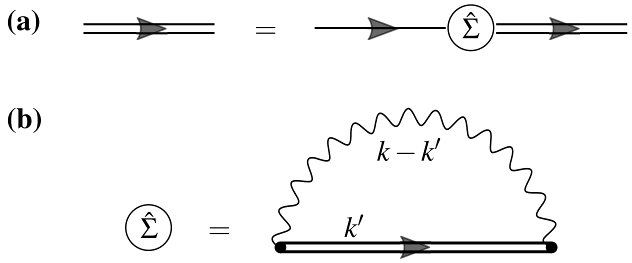

Figure 2.1. (a) Dyson equation for the electron Green's function. Double lines refer to the fully interacting, single lines to the non-interacting Green's function. (b) Electron self-energy under Migdal's approximation, using the notation $k = (\mathbf{k}, i\omega_m)$. The wavy lines represent the phonon propagator.

the electron self-energy can be calculated as a series of infinitely many Feynman diagrams with expansion parameter $\lambda\alpha$ [4]. Here λ is the FS-averaged electron-phonon coupling strength (defined below) and $\alpha = \Omega/\varepsilon_F$ with Ω the relevant phonon energy scale and ε_F the shallowness of the electron dispersion (smallest distance between bottom/top of $\xi_{\mathbf{k}}$ to the Fermi level). Under Migdal's approximation it is justified to keep only the first electron-phonon scattering diagram, compare the 'rainbow diagram' in Fig. 2.1(b), which includes all processes of first order. This is not to be confused with Migdal's theorem, which states that higher-order diagrams, or vertex corrections, and processes away from the Fermi level are negligible in 3D systems with $\alpha \ll 1$ [4]. While here and in Part I we consider the diagram in Fig. 2.1(b), we show possible effects due to higher order Feynman diagrams in Part II of the thesis.

As concerns the phonon self-energy $\Pi_{\mathbf{q},l}$, we follow the commonly accepted approximation of $\Pi_{\mathbf{q},l} = 0$. This means that the phonon propagator, which follows a Dyson equation similar to that of the electron Green's function, becomes $D_{\mathbf{q},l,\nu} = D^0_{\mathbf{q},l,\nu} = [iq_l - \omega_{\mathbf{q},\nu}]^{-1} - [iq_l + \omega_{\mathbf{q},\nu}]^{-1}$, with bosonic Matsubara frequency $q_l = 2\pi T l$. Note, that we have explored the effects of this approximation in Paper IX, see Section 5.4, where we keep a finite phonon self-energy that results in a backreaction of the electrons onto the phonon spectrum and electron-phonon coupling. Finally, we make here the assumption that the frequency independent and Cooper pair breaking Coulomb interaction is effectively included in our electron-phonon coupling strength and in the electron energies.

Under the above mentioned approximations we can now evaluate the Feynman diagram in Fig. 2.1(b) as

$$\hat{\Sigma}_{\mathbf{k},m} = -T \sum_{\mathbf{k}',m',\nu} |g_{\mathbf{k}-\mathbf{k}',\nu}|^2 D_{\mathbf{k}-\mathbf{k}',m-m',\nu} \hat{\rho}_3 \hat{G}_{\mathbf{k}',m'} \hat{\rho}_3, \tag{2.10}$$

where we used momentum and energy conservation. The electron-phonon coupling is defined as

$$V_{\mathbf{q},l} = -\sum_{\nu} |g_{\mathbf{q},\nu}|^2 D_{\mathbf{q},l,\nu}, \tag{2.11}$$

leading to the electron self-energy

$$\hat{\Sigma}_{\mathbf{k},m} = T \sum_{\mathbf{k}',m'} V_{\mathbf{k}-\mathbf{k}',m-m'} \hat{\rho}_3 \hat{G}_{\mathbf{k}',m'} \hat{\rho}_3. \tag{2.12}$$

The final step is to insert the electron Green's function of Eq. (2.9) into Eq. (2.12). We then have, together with Eq. (2.8) two expressions for $\hat{\Sigma}_{\mathbf{k},m}$, which we both multiply by each of $\hat{\rho}_i$, $i \in \{0,1,2,3\}$, and take the matrix trace. The resulting self-consistent equations read

$$Z_{\mathbf{k},m} = 1 - \frac{T}{\omega_m} \sum_{\mathbf{k}',m'} V_{\mathbf{k}-\mathbf{k}',m-m'} \frac{\omega_{m'} Z_{\mathbf{k}',m'}}{\Theta_{\mathbf{k}',m'}}, \tag{2.13a}$$

$$\chi_{\mathbf{k},m} = T \sum_{\mathbf{k}',m'} V_{\mathbf{k}-\mathbf{k}',m-m'} \frac{\xi_{\mathbf{k}'} + \chi_{\mathbf{k}',m'}}{\Theta_{\mathbf{k}',m'}}, \tag{2.13b}$$

$$\phi_{\mathbf{k},m} = -T \sum_{\mathbf{k}',m'} V_{\mathbf{k}-\mathbf{k}',m-m'} \frac{\phi_{\mathbf{k}',m'}}{\Theta_{\mathbf{k}',m'}}, \tag{2.13c}$$

$$\zeta_{\mathbf{k},m} = -T \sum_{\mathbf{k}',m'} V_{\mathbf{k}-\mathbf{k}',m-m'} \frac{\zeta_{\mathbf{k}',m'}}{\Theta_{\mathbf{k}',m'}}. \tag{2.13d}$$

These equations are accompanied by the electron filling

$$n = 1 - 2T \sum_{\mathbf{k},m} \frac{\xi_{\mathbf{k}} + \chi_{\mathbf{k},m}}{\Theta_{\mathbf{k},m}}, \tag{2.14}$$

where $\xi_{\mathbf{k}}$ is assumed to contain any rigid chemical potential shift. Note that one may include the Coulomb repulsion explicitly in Eqs. (2.13) by replacing the EPI by $V_{\mathbf{q},l} - V^C_{\mathbf{q}}$ in the expressions for $\phi_{\mathbf{k},m}$ and $\zeta_{\mathbf{k},m}$. The normal state functions $Z_{\mathbf{k},m}$ and $\chi_{\mathbf{k},m}$ on the other hand are commonly assumed to already include the electron-electron interaction [8]. However, since the Coulomb term is frequency independent it is rather difficult to implement numerically. For this reason we assumed an electron-phonon coupling that effectively includes a Coulomb repulsion part when considering the level of approximation leading to Eqs. (2.13).

Under Migdal's approximation the function $\zeta_{\mathbf{k},m}$ can be interpreted as the imaginary part of the superconducting gap. Due to the fact that Eqs. (2.13c) and (2.13d) have equivalent functional forms, we can expect that their self-consistent solutions will differ only by a proportionality factor. In such a case it is common practice to break the gauge freedom with respect to the quantum mechanical phase factor of the Cooper pairs, which allows us to set $\zeta_{\mathbf{k},m} = 0$. In this case the superconducting energy gap can be calculated by $\Delta_{\mathbf{k},m} = \phi_{\mathbf{k},m}/Z_{\mathbf{k},m}$. However, for Part II of this thesis it is important to keep in mind that this choice is motivated by the current level of approximation. As we show in Section 7.3 and Paper XIII, when vertex corrections to the EPI are considered $\zeta_{\mathbf{k},m}$ can describe a spin-triplet pair condensate that coexists with the one modeled by $\phi_{\mathbf{k},m}$.

As mentioned earlier, other bosons than EPI can possibly mediate superconductivity. In the prominent example of spin fluctuations the interaction kernel in Eqs. (2.13a) and (2.13b) may be replaced by a function $V^{(+)}_{\mathbf{q},l}$ but otherwise the functional form does not change. For the superconductivity order parameter one uses a different interaction, $V^{(-)}_{\mathbf{q},l}$, and acquires a minus sign in the equivalent of Eq. (2.13c),

$$\phi_{\mathbf{k},m} = T \sum_{\mathbf{k}',m'} V^{(-)}_{\mathbf{k}-\mathbf{k}',m-m'} \frac{\phi_{\mathbf{k}',m'}}{\Theta_{\mathbf{k}',m'}}, \tag{2.15}$$

which stems from the repulsive nature of spin fluctuations interactions. For explicit examples of kernels due to spin and charge fluctuations we refer to Sections 3.2 or 7.2. Even though such a formalism is commonly employed, either on the level of Eliashberg theory or under various approximations, there is no formal justification of keeping only the lowest order in the electron-boson scattering diagrams, since no analogue of Migdal's theorem exists for purely electronic mechanisms [21].

Before we move on to the calculation of spectral properties, it is worth commenting briefly on the generalization to multiple electron bands. The most straightforward case would be to consider band n dependent electron energies $\xi_{\mathbf{k},n}$ but a global coupling to the boson degree of freedom. In such a case we simply get a band-dependent Green's function in Eqs. (2.9), and this index is summed over when inserting into Eq. (2.12). In particular, this means that $Z_{\mathbf{k},m}$, $\chi_{\mathbf{k},m}$ and $\phi_{\mathbf{k},m}$ are calculated as described above due to the fact that the electron-phonon coupling and the purely electronic parts in Eqs. (2.13) are decoupled with respect to the energy band index. If, on the other hand, we want to include a band-dependency in the coupling via $V^{n,n'}$, all functions in Eq. (2.13) acquire an explicit band dependence on index n, while we have to sum over index n'. For more details we refer e.g. to the Papers I, II and III.

2.1.2 Spectral properties

So far we considered the description of the superconducting state on the Matsubara frequency axis. However, to obtain spectral properties that can directly be compared to experiment we need to analytically continue the results to real frequencies. The starting point of this procedure is the electron self-energy in

Eq. (2.10). For simplicity let us assume from here on a single isotropic optical phonon branch Ω. Following Ref. [22], we use the spectral representations

$$\hat{G}_{\mathbf{k},m} = \int \mathrm{d}z \frac{\hat{A}_{\mathbf{k}}(z)}{i\omega_m - z}, \tag{2.16a}$$

$$D_{\mathbf{q},l} = \int \mathrm{d}z \frac{B_{\mathbf{q}}(z)}{iq_l - z}, \tag{2.16b}$$

for the electron and phonon Green's functions. With Eqs. (2.16) we write the self-energy as

$$\hat{\Sigma}_{\mathbf{k},m} = -\frac{1}{2}\sum_{\mathbf{k}'} |g_{\mathbf{k}-\mathbf{k}'}|^2 \iint \mathrm{d}z\mathrm{d}z' B_{\mathbf{k}-\mathbf{k}'}(z)\hat{\rho}_3 \frac{\hat{A}_{\mathbf{k}'}(z')}{i\omega_m - z - z'}\hat{\rho}_3 \left(\tanh\frac{z'}{2T} + \coth\frac{z}{2T}\right), \tag{2.17}$$

where the sum over Matsubara frequencies m' has been evaluated analytically.

Next we make use of the relation $\hat{A}_{\mathbf{k}}(z) = -\pi^{-1}\mathrm{Im}[\hat{G}_{\mathbf{k}}(z)]$ for the electron spectral density, where $\hat{G}_{\mathbf{k}}(z)$ is the retarded Green's function [22], and carry out the analytic continuation by letting $i\omega_m \to \omega + i\delta$. We then can write the fraction in Eq. (2.17) as

$$\begin{aligned}
\frac{\hat{A}_{\mathbf{k}'}(z')}{\omega + i\delta - z - z'} &= -\frac{1}{\pi}\mathrm{Im}[\hat{G}_{\mathbf{k}'}(z')]\frac{1}{\omega + i\delta - z - z'} \\
&= \frac{1}{2\pi}\mathrm{Im}\Big[\hat{G}_{\mathbf{k}'}(z')\big(\frac{1}{\omega + i\delta - z - z'} + \frac{1}{\omega - i\delta - z - z'}\big)\Big] \\
&\quad - \frac{1}{2\pi}\mathrm{Re}\Big[\hat{G}_{\mathbf{k}'}(z')\big(\frac{1}{\omega + i\delta - z - z'} - \frac{1}{\omega - i\delta - z - z'}\big)\Big].
\end{aligned} \tag{2.18}$$

The last step of Eq. (2.18) can be proven by using ordinary arithmetic. As an integration path in z' we choose a closed contour in the upper half plane where the retarded Green's function is analytic. There the only poles are given by $z' = \omega - z + i\delta$ from the fraction in Eq. (2.18), and $z' = i\omega_m$ for $m \geq 0$ from the hyperbolic tangent. Using Cauchy's residue theorem, we perform the integration over z' to get

$$\begin{aligned}
\hat{\Sigma}_{\mathbf{k}}(\omega) =& \frac{1}{2}\sum_{\mathbf{k}'} |g_{\mathbf{k}-\mathbf{k}'}|^2 \int \mathrm{d}z B_{\mathbf{k}-\mathbf{k}'}(z)\hat{\rho}_3 \Big[\hat{G}_{\mathbf{k}'}(\omega - z)\big(\tanh\frac{\omega - z}{2T} \\
&+ \coth\frac{z}{2T}\big) - 2T\sum_{m,\omega_m>0}\big(\frac{\hat{G}_{\mathbf{k}',m}}{\omega - z - i\omega_m} + \frac{\hat{G}^*_{\mathbf{k}',m}}{\omega - z + i\omega_m}\big)\Big]\hat{\rho}_3,
\end{aligned} \tag{2.19}$$

where '*' denotes complex conjugations. To arrive at Eq. (2.19) the result has been simplified by using basic properties of the real and imaginary part of complex functions. After performing the integration we set $\delta = 0$, which is allowed due to the fact that ω_m is always finite.

The conjugated electron Green's function fulfills the property $\hat{G}^*_{\mathbf{k},m} = \hat{G}_{\mathbf{k},-m}$ [22], which allows us to express Eq. (2.19) as

$$\begin{aligned} \hat{\Sigma}_{\mathbf{k}}(\omega) = -\sum_{\mathbf{k}'} |g_{\mathbf{k}-\mathbf{k}'}|^2 \int \mathrm{d}z B_{\mathbf{k}-\mathbf{k}'}(z) \hat{\rho}_3 \Big[T \sum_m \frac{\hat{G}_{\mathbf{k}',m}}{\omega - z - i\omega_m} \\ - \frac{1}{2} \hat{G}_{\mathbf{k}'}(\omega - z) \big(\tanh\frac{\omega - z}{2T} + \coth\frac{z}{2T} \big) \Big] \hat{\rho}_3 . \end{aligned} \tag{2.20}$$

We now make a case distinction between the two terms in the square brackets of Eq. (2.20). The phonon spectral function can be expressed as $B_{\mathbf{k}-\mathbf{k}'}(z) = \delta(z - \Omega) - \delta(z + \Omega)$, which we insert for the first term. Due to the delta functions we can easily evaluate the integration over z analytically. For the second term we insert the Eliashberg function $\alpha^2 F_{\mathbf{k}-\mathbf{k}'}(z)$, which is connected to $B_{\mathbf{k}-\mathbf{k}'}(z)$ via

$$\alpha^2 F_{\mathbf{k}-\mathbf{k}'}(z) = N_0 |g_{\mathbf{k}-\mathbf{k}'}|^2 B_{\mathbf{k}-\mathbf{k}'}(z). \tag{2.21}$$

The result reads

$$\begin{aligned} \hat{\Sigma}_{\mathbf{k}}(\omega) = T \sum_{\mathbf{k}'} \sum_{m} V_{\mathbf{k}-\mathbf{k}'}(\omega - i\omega_m) \hat{\rho}_3 \hat{G}_{\mathbf{k}',m} \hat{\rho}_3 \\ + \int \mathrm{d}z \sum_{\mathbf{k}'} \frac{\alpha^2 F_{\mathbf{k}-\mathbf{k}'}(z)}{2N_0} \hat{\rho}_3 \hat{G}_{\mathbf{k}'}(\omega - z) \hat{\rho}_3 \big(\tanh\frac{\omega - z}{2T} + \coth\frac{z}{2T} \big), \end{aligned} \tag{2.22}$$

where we used a similar definition for the electron-phonon coupling as before, $V_{\mathbf{k}-\mathbf{k}'}(\omega - i\omega_m) = 2|g_{\mathbf{k}-\mathbf{k}'}|^2 \Omega / (\Omega^2 + (\omega - i\omega_m)^2)$.

From here we follow the derivation of Section 2.1.1, using Eq. (2.22) and the real-frequency analogue of Eq. (2.8) to arrive at self-consistent Eliashberg equations by selecting the different functions via $\mathrm{Tr}[\hat{\rho}_i \hat{\Sigma}_{\mathbf{k}}(\omega)]$. The result reads

$$\begin{aligned} Z_{\mathbf{k}}(\omega) = & 1 - \frac{T}{\omega} \sum_{\mathbf{k}',m} V_{\mathbf{k}-\mathbf{k}'}(\omega - \omega_m) \frac{i\omega_m Z_{\mathbf{k}',m}}{\Theta_{\mathbf{k}',m}} - \int_{-\infty}^{\infty} \frac{\mathrm{d}z}{2\omega} \sum_{\mathbf{k}'} \frac{\alpha^2 F_{\mathbf{k}-\mathbf{k}'}(z)}{N_0} \\ & \times \left(\tanh\frac{\omega - z}{2T} + \coth\frac{z}{2T} \right) \frac{[\omega - z] Z_{\mathbf{k}'}(\omega - z)}{\Theta_{\mathbf{k}'}(\omega - z)}, \end{aligned} \tag{2.23a}$$

$$\begin{aligned} \chi_{\mathbf{k}}(\omega) = & T \sum_{\mathbf{k}',m} V_{\mathbf{k}-\mathbf{k}'}(\omega - \omega_m) \frac{\xi_{\mathbf{k}'} + \chi_{\mathbf{k}',m}}{\Theta_{\mathbf{k}',m}} + \int_{-\infty}^{\infty} \frac{\mathrm{d}z}{2} \sum_{\mathbf{k}'} \frac{\alpha^2 F_{\mathbf{k}-\mathbf{k}'}(z)}{N_0} \\ & \times \left(\tanh\frac{\omega - z}{2T} + \coth\frac{z}{2T} \right) \frac{\xi_{\mathbf{k}'} + \chi_{\mathbf{k}'}(\omega - z)}{\Theta_{\mathbf{k}'}(\omega - z)}, \end{aligned} \tag{2.23b}$$

$$\begin{aligned} \phi_{\mathbf{k}}(\omega) = & -T \sum_{\mathbf{k}',m} V_{\mathbf{k}-\mathbf{k}'}(\omega - \omega_m) \frac{\phi_{\mathbf{k}',m}}{\Theta_{\mathbf{k}',m}} - \int_{-\infty}^{\infty} \frac{\mathrm{d}z}{2} \sum_{\mathbf{k}'} \frac{\alpha^2 F_{\mathbf{k}-\mathbf{k}'}(z)}{N_0} \\ & \times \left(\tanh\frac{\omega - z}{2T} + \coth\frac{z}{2T} \right) \frac{\phi_{\mathbf{k}'}(\omega - z)}{\Theta_{\mathbf{k}'}(\omega - z)}. \end{aligned} \tag{2.23c}$$

It is important to note that the Matsubara frequency dependent terms in Eqs. (2.23) are assumed to be known, as they are calculated from the solutions to Eqs. (2.13). The self-consistency condition is to be understood here only in terms of functions $Z_{\mathbf{k}}(\omega)$, $\chi_{\mathbf{k}}(\omega)$ and $\phi_{\mathbf{k}}(\omega)$.

In deriving Eqs. (2.23) we have set the parameter of the analytic continuation $\delta = 0$. However, it should be noted that a finite δ is often needed to ensure numerical stability when solving the above equations in an iterative loop. The numerical implementation in our work was done by using Fast Fourier Transforms (FFTs) to speed up the iterative cycle. To be explicit, in the self-consistent equations (real and Matsubara frequency dependent) it is computationally expensive to evaluate sums of the form $\sum_{\mathbf{k}',m'} g_{\mathbf{k}-\mathbf{k}',m-m'} f_{\mathbf{k}',m'}$. In momentum space this expression equals a convolution due to the periodicity of the BZ and can therefore be evaluated by FFTs. On the frequency axis this convolution is mathematically not exact but a good approximation, provided that sufficiently large grids are used. We can therefore write

$$\sum_{\mathbf{k}',m'} g_{\mathbf{k}-\mathbf{k}',m-m'} f_{\mathbf{k}',m'} \simeq \mathscr{F}^{-1}\big\{\mathscr{F}\big(g_{\mathbf{k}-\mathbf{k}',m-m'}\big) \star \mathscr{F}\big(f_{\mathbf{k}',m'}\big)\big\}, \tag{2.24}$$

which significantly reduces the numerical workload. For additional computational details of the here-employed Eliashberg theory, we refer to Paper VIII.

The main purpose of the analytic continuation introduced here is that we want to compare our model with experimentally accessible quantities. Besides basic properties of the superconducting state, such as the critical temperature or the gap edge $\Delta_{\mathbf{k}}(0)$, we can use the spectral function to compare our theory to Angular Resolved Photoemission Spectroscopy and Tunneling spectra:

$$A_{\mathbf{k}}(\omega) = -\frac{1}{\pi}\mathrm{Im}\big[\hat{G}_{\mathbf{k}}(\omega + i\delta)\big]_{11}, \tag{2.25a}$$

$$\frac{\mathrm{d}I}{\mathrm{d}V} \propto A(\omega) = \sum_{\mathbf{k}} A_{\mathbf{k}}(\omega). \tag{2.25b}$$

Here $A_{\mathbf{k}}(\omega)$ describes the momentum and energy resolved quasiparticle spectrum, and $\mathrm{d}I/\mathrm{d}V$ is the differential conductance that can directly be measured in experiment. As a side note, these are only a few examples of measurement quantities; since we know the electron Green's function it is possible to derive equations for all thermodynamic properties of the system.

2.2 Simplified approaches

We now want to look into various approaches to describe the superconducting state of a given system in a more approximate way. We start by deriving anisotropic FS restricted equations, which are then simplified to the isotropic case. Afterwards we show how the linearized gap equation can be derived at temperatures close to T_c. Finally, we discuss the McMillan equation for the critical temperature and the famous BCS formalism.

2.2.1 Fermi surface restricted Eliashberg theory

Let us consider again the electron self-energy in Eq. (2.12). We assume now that only processes close to the Fermi level play a significant role to accurately describe the superconducting state. If we assume that the product under the momentum sum in Eq. (2.12) is separable we can use

$$\sum_{\mathbf{k}'} \hat{G}_{\mathbf{k}',m'}(\xi_{\mathbf{k}'}) = \int_{-\infty}^{\infty} \mathrm{d}\varepsilon \sum_{\mathbf{k}'} \delta(\xi_{\mathbf{k}'} - \varepsilon) \hat{G}_{\mathbf{k}',m'}(\varepsilon), \tag{2.26}$$

where we imposed infinite electron bandwidth. Now we can make explicit use of the FS restriction of electron degrees of freedom by setting $\varepsilon = 0$ in the delta function of Eq. (2.26). The self-energy can then be written as

$$\begin{aligned} \hat{\Sigma}_{\mathbf{k},m} &= T \sum_{\mathbf{k}',m'} \frac{\delta(\xi_{\mathbf{k}'})}{N_0} N_0 V_{\mathbf{k}-\mathbf{k}',m-m'} \hat{\rho}_3 \int_{-\infty}^{\infty} \mathrm{d}\varepsilon \hat{G}_{\mathbf{k}',m'}(\varepsilon) \hat{\rho}_3 \\ &= T \sum_{\mathbf{k}',m'} \frac{\delta(\xi_{\mathbf{k}'})}{N_0} \lambda_{\mathbf{k}-\mathbf{k}',m-m'} \hat{\rho}_3 \hat{g}_{\mathbf{k}',m'} \hat{\rho}_3, \end{aligned} \tag{2.27}$$

employing the definition $\lambda_{\mathbf{k}-\mathbf{k}',m-m'} = N_0 V_{\mathbf{k}-\mathbf{k}',m-m'}$ of the electron-phonon coupling.

By using the explicit form of the electron Green's function, Eqs. (2.9), we can split the reduced Green's function into prefactors of the Pauli matrices. With a change of variables $\varepsilon \to \varepsilon + \chi_{\mathbf{k},m}$ it becomes apparent that the prefactor of $\hat{\rho}_3$ vanishes because the integrand is an odd function. On the other hand, for $\hat{\rho}_0$ and $\hat{\rho}_1$ the integrals can be evaluated via the residue theorem, leading to

$$\hat{g}_{\mathbf{k},m} = -\pi \left[i\omega_m Z_{\mathbf{k},m} \hat{\rho}_0 + \phi_{\mathbf{k},m} \hat{\rho}_1 \right] \theta_{\mathbf{k},m}^{-1}, \tag{2.28a}$$

$$\theta_{\mathbf{k},m} = \sqrt{\omega_m^2 Z_{\mathbf{k},m}^2 + \phi_{\mathbf{k},m}^2}. \tag{2.28b}$$

The next step is to insert Eqs. (2.28) into Eq. (2.27), set the result equal to Eq. (2.8) and perform the Nambu traces as before. We then find two self-consistent equations

$$Z_{\mathbf{k},m} = 1 + \frac{\pi T}{\omega_m} \sum_{\mathbf{k}',m'} \frac{\delta(\xi_{\mathbf{k}'})}{N_0} \lambda_{\mathbf{k}-\mathbf{k}',m-m'} \frac{\omega_{m'}}{\sqrt{\omega_{m'}^2 + \Delta_{\mathbf{k}',m'}^2}}, \tag{2.29a}$$

$$\Delta_{\mathbf{k},m} = \frac{\pi T}{Z_{\mathbf{k},m}} \sum_{\mathbf{k}',m'} \frac{\delta(\xi_{\mathbf{k}'})}{N_0} \left[\lambda_{\mathbf{k}-\mathbf{k}',m-m'} - \mu^\star(\omega_c) \right] \frac{\Delta_{\mathbf{k}',m'}}{\sqrt{\omega_{m'}^2 + \Delta_{\mathbf{k}',m'}^2}}, \tag{2.29b}$$

and now solve explicitly for the superconducting gap $\Delta_{\mathbf{k},m} = \phi_{\mathbf{k},m}/Z_{\mathbf{k},m}$ instead of the order parameter $\phi_{\mathbf{k},m}$.

In Eq. (2.29b) we have explicitly added the Anderson-Morel pseudopotential $\mu^\star$, which is the momentum averaged and renormalized Coulomb repulsion [8]. This quantity is commonly treated as free parameter and enters the

Eliashberg equations with a frequency cutoff ω_c, i.e. $\mu^\star$ is considered finite in the interval $[-\omega_c, \omega_c]$ and zero otherwise. As it was described in Section 2.1.1, it is possible to use Eqs. (2.29) also for spin fluctuation mediated superconductivity when an additional minus sign in front of the coupling is inserted in the gap equation.

2.2.2 Isotropic Eliashberg theory

When the electron-phonon coupling can be considered isotropic throughout the BZ, $\lambda_{\mathbf{k}-\mathbf{k}',m-m'} = \lambda_{m-m'}$, the mass renormalization and gap function similarly become momentum independent. This is due to the relation $\sum_{\mathbf{k}} \delta(\xi_{\mathbf{k}}) = N_0$, leading to

$$Z_m = 1 + \frac{\pi T}{\omega_m} \sum_{m'} \lambda_{m-m'} \frac{\omega_{m'}}{\sqrt{\omega_{m'}^2 + \Delta_{m'}^2}}, \tag{2.30a}$$

$$\Delta_m = \frac{\pi T}{Z_m} \sum_{m'} \left[\lambda_{m-m'} - \mu^\star(\omega_c)\right] \frac{\Delta_{m'}}{\sqrt{\omega_{m'}^2 + \Delta_{m'}^2}}. \tag{2.30b}$$

These equations form the next level of simplification of the full, anisotropic Eliashberg equations.

2.2.3 Linearized Eliashberg theory

Considering Eqs. (2.30), it can be useful to assume the limit $T \to T_c$ which results in a vanishing superconducting gap. It is therefore justified to set $\Delta_m^2 = 0$ leading to the mass renormalization

$$Z_m = 1 + \frac{\pi T_c}{\omega_m} \sum_{m'} \lambda_{m-m'} \mathrm{sign}[\omega_{m'}]. \tag{2.31}$$

It is important to note that Eq. (2.31) is a closed expression, i.e. Z_m is no longer a function of the superconducting gap and can hence be evaluated individually. The Matsubara frequency sum can be carried out analytically, and in the limit $T_c \ll \Omega$ one can show that $Z_m \simeq 1 + \lambda \arctan(\omega_m/\Omega)/(\omega_m/\Omega)$ [23], with $\lambda = \lambda_{m-m'=0}$. Here Ω is the relevant phonon energy scale. For frequencies close to the Fermi level one can therefore write $Z_m \simeq 1 + \lambda$.

However the mass renormalization is approximated in the above, the self-consistency condition for the interacting state reduces to the single gap equation

$$\Delta_m Z_m = \pi T_c \sum_{m'} \left[\lambda_{m-m'} - \mu^\star(\omega_c)\right] \frac{\Delta_{m'}}{|\omega_{m'}|}, \tag{2.32}$$

which can be recast as an eigenvalue problem, greatly reducing the numerical complexity. As a side remark, even though Eq. (2.32) is isotropic, an anisotropic analogue can be derived by following the same steps as above.

2.2.4 McMillan equation for T_c

So far we have derived different kinds of self-consistent equations for the superconducting gap and normal state properties. In each of theses cases T_c is determined indirectly via the superconductivity order parameter. In practice this means that the equations have to be solved at different temperatures, and T_c is defined as the largest temperature that leads to a finite gap. As first pointed out by McMillan, under some additional approximations it is possible to find a closed formula for the critical temperature, that works reasonably well for weak-coupling elemental superconductors [6].

Starting with the mass renormalization in Eq. (2.31), we apply a square-well approximation to the electron-phonon coupling, $\lambda_l = \lambda\Theta(\omega_D - |q_l|)$, i.e. we assume a constant interaction λ in $[-\omega_D, \omega_D]$ and neglect contributions outside this interval. Here ω_D describes the Debye frequency [8]. For the mass renormalization

$$Z_m = 1 + \lambda\frac{\pi T_c}{\omega_m}\sum_{m'}\Theta(\omega_D - |q_{m-m'}|)\mathrm{sign}[\omega_{m'}] \tag{2.33}$$

it follows that the summation over Matsubara frequency index m' is restricted to a finite region. The corresponding lower and upper bound of this sum are determined from $q_l = \pm\omega_D$, with $l = m - m'$. It follows that m' must lie in $[m + \omega_D/2\pi T_c, m - \omega_D/2\pi T_c]$, and since $\omega_D > 0$ we choose to write the sum as $\sum_{m'=m-\omega_D/2\pi T_c}^{m+\omega_D/2\pi T_c}$. We can now separately consider the intervals $m' \in [m - \omega_D/2\pi T_c, -1]$ and $m' \in [0, m + \omega_D/2\pi T_c]$, where the sign function in Eq. (2.33) gives (-1) and $(+1)$, respectively. It is straightforward to write the approximate mass renormalization as

$$\begin{aligned} Z_m &= 1 + \lambda\frac{\pi T_c}{\omega_m}\Big[(-1)\big(-m + \frac{\omega_D}{2\pi T_c}\big) + (+1)\big(m + \frac{\omega_D}{2\pi T_c} + 1\big)\Big] \\ &= 1 + \lambda. \end{aligned} \tag{2.34}$$

Next we insert Eq. (2.34) into Eq. (2.32) and apply the square-well assumption $\lambda_{m-m'} = \lambda\Theta(\omega_D - |\omega_m|)\Theta(\omega_D - |\omega_{m'}|)$. Further we adjust the frequency cutoff ω_c entering the Coulomb pseudopotential to coincide with ω_D, which yields

$$\Delta_m = \pi T_c\frac{\lambda - \mu^\star}{1+\lambda}\sum_{m'}(\lambda - \mu^\star)\Theta(\omega_D - |\omega_m|)\Theta(\omega_D - |\omega_{m'}|)\frac{\Delta_{m'}}{|\omega_{m'}|}. \tag{2.35}$$

When neglecting any impurities in the system [8] the superconducting gap can be expressed as $\Delta_m = \Delta\Theta(\omega_D - |\omega_m|)$, allowing us to cancel the gap magnitude Δ on both sides of Eq. (2.35). For the low energy spectrum we therefore get

$$\frac{1+\lambda}{\lambda - \mu^\star} = \sum_{m'}\Theta(\omega_D - |\omega_{m'}|)\frac{1}{|2m'+1|}. \tag{2.36}$$

The Matsubara sum in Eq. (2.36) can be evaluated analytically, which yields digamma functions that take the approximate form

$$\frac{1+\lambda}{\lambda-\mu^\star} \simeq \log\big(\frac{\omega_D}{2\pi T_c}\big) - \log\big(\frac{e^{-\gamma}}{4}\big), \tag{2.37}$$

with γ the Euler-Mascheroni constant [8, 24]. Finally, when solving for the critical temperature we find the McMillan equation

$$T_c = \frac{2e^{\gamma}}{\pi}\omega_D \exp\big(-\frac{1+\lambda}{\lambda-\mu^\star}\big). \tag{2.38}$$

Even though the original result by McMillan differed slightly from Eq. (2.38), it is similar in essence: With the electron-phonon coupling strength, the Coulomb repulsion and a measure for the phonon energy scale it is possible to explain experimentally observed values for the critical temperature in a certain regime of ω_D, λ and $\mu^\star$. Various authors have attempted to reduce the complexity of the superconducting state to a semi-empirical single expression for T_c [6, 25–27], e.g. by including additional parameters of the system. While it is possible to explain the critical temperature of BCS-like superconductors with moderate coupling strengths, it is ultimately unlikely that the measurement results for all superconductors can be fit into a closed expression with only few system parameters [8].

2.2.5 BCS theory

Historically the first microscopic theory of the superconducting state was developed by Bardeen, Cooper and Schrieffer [3]. Even though we hardly used this BCS theory for the papers of this thesis, it is worthwhile discussing it briefly here. We will not go into great detail about the rigorous derivation of the BCS gap equation, but rather explain the connection to Eliashberg theory. The more interested reader is referred to Refs. [28–30].

Let us go back to Eqs. (2.30) where we assumed isotropic electron-phonon coupling. For the mass renormalization we use the same procedure as in Section 2.2.4, i.e. we apply the square-well model to the linearized expression and find $Z_m = 1+\lambda$. For the superconducting gap in Eq. (2.30b) we assume $\lambda_{m-m'} = \lambda\Theta(\omega_c - |\omega_m|)\Theta(\omega_c - |\omega_{m'}|)$, so we use the same frequency cutoff as for the Coulomb pseudopotential, with ω_c in close vicinity to the Fermi level. With $\Delta_m = \Delta\Theta(\omega_c - |\omega_c|)$ we find

$$\Delta\frac{1+\lambda}{\lambda-\mu^\star} = \pi T \sum_{m', |\omega_{m'}|<\omega_c} \frac{\Delta}{\sqrt{\omega_{m'}^2+\Delta^2}}. \tag{2.39}$$

Taking into account that the fraction on the left side of Eq. (2.39) gives an effective electron-phonon coupling, $(\lambda-\mu^\star)/(1+\lambda) = N_0 V$, we identify the above expression as finite temperature and isotropic BCS gap equation [24]. From here it is possible to recover the McMillan equation for T_c when using the approximation $\Delta^2 \simeq 0$.

However, it is standard to use an anisotropic and frequency independent gap equation within BCS theory, reading

$$\Delta_{\mathbf{k}} = \sum_{\mathbf{k}'} V_{\mathbf{k},\mathbf{k}'} \frac{\Delta_{\mathbf{k}'}}{2E_{\mathbf{k}'}} \tanh\left(\frac{E_{\mathbf{k}'}}{2T}\right), \tag{2.40}$$

with quasiparticle energy $E_{\mathbf{k}} = \sqrt{\xi_{\mathbf{k}}^2 + \Delta_{\mathbf{k}}^2}$ [31]. As apparent from Eq. (2.40), the BCS formalism is static and therefore any time and frequency dependence is neglected (in its original form). This means retardation, i.e. the time delay between the two electrons forming a Cooper pair and the exchange boson is not taken into account, which is in contrast to Eliashberg theory. However, the simplicity of Eq. (2.40) is certainly appealing when it comes to numerical costs: While Eliashberg equations are commonly solved in an iterative loop, which can quickly become very demanding computationally, the BCS equation can be cast as an eigenvalue problem.

When considering spin fluctuations as Cooper pair mediator, Eq. (2.40) is also broadly used, with the only modification being an additional minus sign on the right hand side [32, 33]. It needs to be mentioned, however, that BCS theory was developed under the assumption of weak electron-phonon coupling. Due to the absence of an analogue to Migdal's theorem for purely electronic mechanisms [21], it is not clear how reliable results from this level of approximation are for a bosonic mechanism different from EPI.

Finally it is worth noting that $\Delta(T=0)/k_BT_c$ in BCS theory is predicted to be 1.76 [24]. This ratio is readily accessible in both theory and experiment, and therefore is an important tool to characterize the coupling strength in a superconductor. For systems with relatively weak electron-phonon coupling, also known as BCS superconductors, $\Delta(T=0)/k_BT_c$ does not deviate significantly from this universal result, leading to an accurate description of elemental superconductors and relatively simple compounds. On the other hand, if the ratio of superconducting gap edge to critical temperature is significantly larger than 1.76 (2 or higher), the here-described BCS formalism often overestimates T_c and is generally not well suited to describe the superconducting state.

Part I:
Applications of Eliashberg theory

3. Monolayer FeSe on $SrTiO_3$

> *At the end of the day, we can endure much more than we think we can.*
>
> Frida Kahlo

In the current Chapter we summarize Papers I, II and III, which fall under the umbrella of studying superconductivity in a single layer of FeSe deposited on a $SrTiO_3$ substrate (FeSe/STO).

For providing a broader overview it is useful to first introduce bulk FeSe, which is a pristine and non-magnetic superconductor with $T_c \sim 8\,\mathrm{K}$ [34]. At high temperatures the system is found to be orthorombic, and it undergoes a phase transition to a tetragonal phase at 90 K [35]. At $T \sim T_c$ FeSe shows nematicity, which is potentially linked to superconductivity [36], but we will not address this aspect here in detail. It is commonly believed that spin fluctuations (SFs) are mediating the Cooper pair condensate in FeSe [37], which is motivated from experimental observation since, for example, neutron spectroscopy measurements revealed the existence of strong magnetic fluctuations in a wide range of temperatures [38]. From a theoretical perspective a purely electronic mechanism is also reasonable, since the unconventional $s_\pm$-wave superconducting gap symmetry can be argued to originate from Fermi surface (FS) nesting properties, which in turn are intimately linked to SF theories [39].

It is further noteworthy that FeSe is close to a BCS-BEC crossover [40,41], which means that the ratio Δ/ε_F approaches unity. Here, Δ is the BCS superconducting gap and ε_F the minimum distance between electron band extremum and Fermi level. This phenomenon has been associated to the temperature evolution of the chemical potential [42,43], which was measured e.g. in Ref. [44]. As concerns the electronic structure, we use a tight-binding description introduced in Ref. [45], which includes all five Fe-*d* orbitals. With this model we obtain the prototypical FS of Fe-based superconductors [37], which consists of hole bands at the Γ, and electron bands at the M point of the folded Brillouin zone (BZ), compare Fig. 3.1(a).

In the monolayer case the critical temperature is drastically increased, $T_c \sim 50-100\,\mathrm{K}$ [46–48], which has created a tremendous research interest. In this system the hole bands at Γ move below the Fermi level, leaving only the electron pockets as a heavily reduced FS area [49], see Fig. 3.1(b). This altered FS topology implies a sensitivity to electron doping, and it has in fact been shown that T_c can be altered by a change in the number of charge carriers [50,51]. The removal of hole bands at the FS has created a challenge for theorists because the 'standard' nesting argument in favor of the SFs mechanism is no longer applicable. For this reason extended theories have been proposed, such as the incipient band scenario [52], which we discuss in more detail below. Another example is orbital selective SFs, which were primarily introduced to explain the momentum space anisotropy of the superconducting gap on each FS pocket [53].

Despite the theoretical and experimental indications for purely electronic mechanisms, electron-phonon interaction (EPI) similarly plays an important role in this system. Angle Resolved Photo Emission Spectroscopy (ARPES) in FeSe/STO revealed the existence of a replica band around the M point of the BZ [54,55], which can directly be associated with EPI, that involve small-momentum (small-$\mathbf{q}$) scattering. To be explicit, this means that electron bands, which cross the Fermi level around M, are replicated below at a certain distance in energy. It has been shown that a small-$\mathbf{q}$ electron-phonon coupling can indeed produce such replica bands, and additionally explain many characteristics of the superconducting state [56–58].

Another important aspect worth mentioning here is the momentum dependence of the superconducting gap in FeSe/STO. As of the day of writing, no consensus has been reached on the BZ symmetry of the order parameter [37,59]. Even though there is broad agreement on the absence of nodes in the BZ, some experiments suggest a sign-preserving s-wave symmetry [47,54,60], while others are more accurately interpreted by assuming a sign change of the gap function [61–63].

Before moving on to the results, it is worth commenting further on the electron dispersions used in the following subsections. As mentioned before, we use a 2D tight-binding model for bulk FeSe that was introduced in Ref. [45]. There are two possible ways to consider the electron energies: Either the

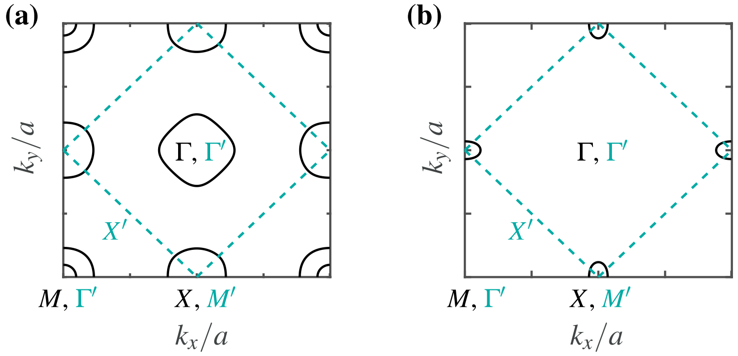

Figure 3.1. Fermi surface of tetragonal (a) bulk FeSe and (b) FeSe/STO. Black solid lines represent the unfolded 1-Fe unit cell, cyan dashed lines the folded 2-Fe unit cell. The Figure was partially taken from Paper II.

real space unit cell contains two Fe atoms, which corresponds to a so-called folded BZ, or only a single Fe atom is considered. In the latter case the unit cell volume in real space is reduced, hence we obtain a larger volume in reciprocal space, the so-called unfolded BZ. In Fig. 3.1(a) the FS is shown in the unfolded BZ (black), while the folded BZ is sketched by cyan dashed lines, and we explicitly write the high-symmetry points in both cases. A similar distinction can be made for FeSe/STO, where the electron energies are taken from Ref. [64]. Here, the tight-binding parameters of bulk FeSe have been adjusted so as to account for the lattice distortion of the FeSe monolayer arising at the interface to the substrate. In Fig. 3.1(b) we show the FS of FeSe/STO in the unfolded BZ as black solid lines, and indicate the folded BZ again in dashed cyan.

In the following we mainly discuss the superconducting state in FeSe/STO. We first consider small-$\mathbf{q}$ EPI as the responsible mechanism in Section 3.1, summarizing Paper I. In Section 3.2 we show the advances of Paper II, where a new way of embedding the SFs mechanism in a full-bandwidth Eliashberg theory is introduced. We benchmark this method with bulk FeSe and then apply it to the monolayer case. Finally, we combine SFs and EPI in Section 3.3, and study the interplay of both mechanisms, which is the content of Paper III.

3.1 Electron-phonon interactions

In Paper I we studied the effect of EPI on the superconducting state in FeSe/STO, which was motivated from the work carried out in Ref. [58]. For this purpose we chose band independent electron-phonon coupling elements $g_{\mathbf{q}}^{n,n'} = g_{\mathbf{q}}$, and modeled the interaction via the small-$\mathbf{q}$ functional form $g_{\mathbf{q}} = g_0 \exp(-a|\mathbf{q}|/0.3)$ [54]. Here, $g_0 = 728\,\mathrm{meV}$ is the electron-phonon scattering strength and a describes the lattice constant of bulk FeSe. Further, we assumed an optical phonon mode at $\Omega = 81\,\mathrm{meV}$ [54, 65], which couples to the electronic degrees of freedom via $g_{\mathbf{q}}$. Under these assumptions, the electron-phonon coupling is given by $V_{\mathbf{q},l}^{(\mathrm{eph})} = 2g_{\mathbf{q}}^2\Omega/(\Omega^2 + q_l^2)$, compare Section 2.1.1. The electron dispersion is considered in the folded BZ, corresponding to the two-Fe unit cell. For extracting properties of the interacting state we solved the self-consistent Eliashberg Eqs. (2.13) at different temperatures. We then performed an analytic continuation from Matsubara space to the real-frequency axis via Eqs. (2.23). From the results we obtained spectral properties, comparable to outcomes of ARPES and Scanning Tunneling Spectroscopy (STS), compare Eqs. (2.25).

As mentioned above, certain superconducting properties in FeSe/STO are strongly doping dependent. Changes in the number of charge carriers are reflected in the electron filling, which is calculated via Eq. (2.14) in the interacting state. For completeness, we print the expression here again:

$$n = 1 - \frac{2T}{L} \sum_{\mathbf{k},n,m} \frac{\xi_{\mathbf{k},n} - \mu + \chi_{\mathbf{k},n,m}}{\Theta_{\mathbf{k},n,m}}. \tag{3.1}$$

From Eq. (3.1) we can derive a self-consistent expression for the chemical potential, reading

$$\mu = \left[\frac{1}{2T} \sum_{\mathbf{k},n} \Big(\tanh \frac{\xi_{\mathbf{k},n} - \mu^{(I)}}{2T} - \tanh \frac{\xi_{\mathbf{k},n} - \mu}{2T} \Big) + \sum_{\mathbf{k},n,|m|\leq \mathscr{M}} \Big(\frac{\xi_{\mathbf{k},n} + \chi_{\mathbf{k},n,m}}{\Theta_{\mathbf{k},n,m}} + \frac{\xi_{\mathbf{k},n}}{\omega_m^2 + [\xi_{\mathbf{k},n} - \mu]^2} \Big) \right] \times \left[\sum_{\mathbf{k},n,|m|\leq \mathscr{M}} \Big(\frac{1}{\Theta_{\mathbf{k},n,m}} + \frac{1}{\omega_m^2 + [\xi_{\mathbf{k},n} - \mu]^2} \Big) \right]^{-1}, \tag{3.2}$$

which is coupled to, and solved on equal footing with Eqs. (2.13). Above, $\mu^{(I)}$ is an initial chemical potential shift, and $\mathscr{M}$ marks the boundaries of our Matsubara frequency grid, $m \in [-\mathscr{M}, \mathscr{M} - 1]$. The word 'initial' refers to a low temperature ($T = 10\,\mathrm{K}$), at which we choose $\mu^{(I)}$, such that both the bottom of the electron band and the replica band at the M point appear at the correct energy in the ARPES spectrum. The advantage of coupling Eq. (3.2) to the Eliashberg equations is that the electron filling is now kept constant self-consistently for increasing temperatures, hence we can ensure that no flowing charges are introduced into the system as T is changed. As a side remark, the hyperbolic functions in Eq. (3.2) appear due to a non-interacting state approximation for the frequency tails in Matsubara space, compare Section 5.3.

With the above described formalism we find a superconducting $T_c \simeq 60\,\mathrm{K}$ and a maximum gap size $\Delta = \max \Delta_{\mathbf{k}_F, m=0} \simeq 11\,\mathrm{meV}$, in excellent agreement with experiment [54]. The symmetry of the order parameter is s-wave, i.e. no sign changes of the gap function are detected on the FS. At $T = 10\,\mathrm{K}$ we resolve the main and replica band peaks in the ARPES spectrum close to the M point at realistic [54,66] energies $-50\,\mathrm{meV}$ and $-160\,\mathrm{meV}$, respectively. In Fig. 3.2(a) we show the computed temperature evolution of the ARPES spectrum in an interval $[10, 300]\,\mathrm{K}$. The position of the main peak, representing the bottom of the electron band, is emphasized by the red solid line, while the replica band position is marked in dashed orange. From our results we were also able to discern a second replication of the main band, shown as yellow dotted-dashed curve in Fig. 3.2(a). This second order peak is harder to detect experimentally, but has been confirmed very recently [67]. The advantage of resolving this signal is that the difference in energy between the first and second order replica band must equal precisely the dominant phonon energy scale, which in our case is $\Omega = 81\,\mathrm{meV}$. Our results further show that the effect of T on all three peak positions should be negligible in the studied temperature range, while thermal broadening effects are expected to produce a peak (green dotted line) slightly above zero energy.

The just observed temperature insensitivity holds equally for the renormalized FS

$$(\xi_{\mathbf{k},n} - \mu + \chi_{\mathbf{k},m=0})/Z_{\mathbf{k},m=0} = 0, \tag{3.3}$$

which we plot in Fig. 3.2(b) for $T = 10\,\mathrm{K}$ (orange) and $T = 300\,\mathrm{K}$ (purple). No significant change can be detected in this comparison, a result that has been confirmed in Ref. [68].

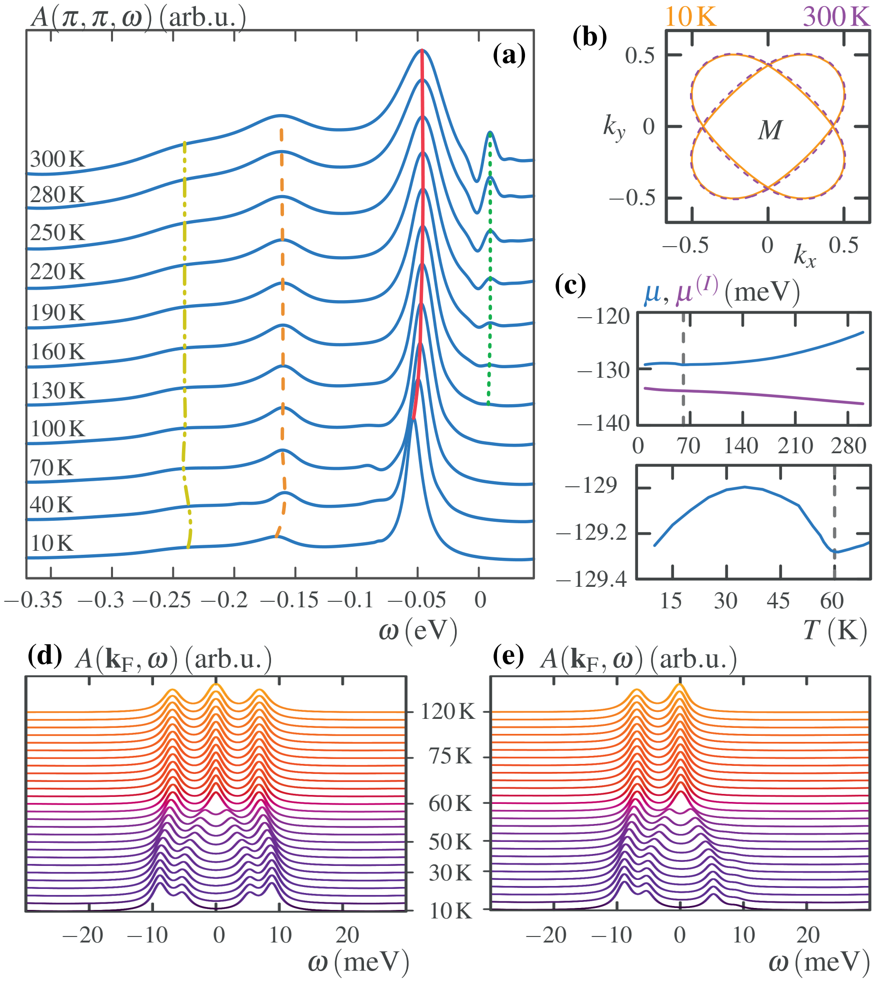

Figure 3.2. Self-consistently calculated results for FeSe/STO. (a) Frequency dependent spectral function at the M point of the Brillouin zone, shown for different temperatures. (b) Renormalized Fermi surface at 10 K (orange) and 300 K (purple). (c) Temperature evolution of chemical potentials μ (blue) and $\mu^{(I)}$ (purple). The lower panel is a zoom into the low-T region of μ. (d) Spectral function at a specific Fermi surface point, shown for different temperatures. The result has been symmetrized with respect to zero energy. (e) Similar to (d), but non-symmetrized. Figure taken from Paper I.

From the fact that we keep the electron filling constant self-consistently with changing temperature, we directly obtain the function $\mu(T)$, which is shown as blue curve in Fig. 3.2(c). In the upper panel, where a relatively large temperature interval is considered, we observe a steady increase in μ above T_c. As a comparison we solved the single self-consistent equation for $\mu^{(I)}$, i.e. the analogue of Eq. (3.2) in the non-interacting state, at each T, and show the outcome as purple line. This temperature dependence corresponds only to the effect of thermal broadening and shows a trend opposite to that of μ. This means that EPI is responsible for counteracting a thermal broadening shift of $\sim -2.3\,\text{meV}$, and producing an observable change in μ of $+5.8\,\text{meV}$. Interestingly, when zooming into the region $T \leq T_c$, see lower panel of Fig. 3.2(c), we observe a hump followed by a kink at the critical temperature. This behavior can be understood by the ratio $\Delta/\varepsilon_F \simeq 0.2-0.3$, placing the system on the BCS side of, and in close vicinity to a BCS-BEC crossover. Even though the chemical potential shows the characteristic features for this regime [42], we were not able to discern a non-BCS shape of Bogoliubov quasiparticle bands. The chemical potential evolution as predicted here has not yet been measured, but should in principle be accessible experimentally.

Next, we turn to the calculation of energy distribution curves (EDCs), as they are found by ARPES measurements. Since the regime $\omega > 0\,\text{eV}$ is difficult to access in experiment, the broadly accepted procedure is to symmetrize EDCs with respect to zero energy and plot the result at specific FS momenta [47, 54]. Since, from a theoretical perspective, we have full access to the entire frequency range, we wanted to put the validity of this procedure to test. In Fig. 3.1(e) we show the temperature evolution of an EDC at one specific $\mathbf{k}_\text{F}$. We observe two energy bands close to the Fermi level, where the left one is isolated and the right one opens up the superconducting gap below T_c, leading to two coherence peaks of unequal height. Since the left main band is below the Fermi level at this $\mathbf{k}_\text{F}$, it is not as strongly associated with coherence of the Bogoliubov quasiparticles, and therefore no signal occurs at $\omega > 0\,\text{eV}$.

Let us now consider the same data that would be accessible experimentally, i.e. only the range $\omega < 0\,\text{eV}$. To get the full spectrum we symmetrize the EDCs in Fig. 3.2(d), following the common practice. As a first observation, coherence peaks are now of equal height and have a symmetric position with respect to zero energy. Since the latter statement similarly holds for panel (e), the peak-to-peak measurement of the superconducting gap is found to be valid. However, we now duplicated the left peak so as to artificially produce the signal of an additional energy band at positive energies. This feature, which prevails in the entire temperature range, is only an artifact from the symmetrization method, therefore one always has to be cautious about features appearing in the inaccessible frequency range of the EDCs.

As a side remark, in Paper I we additionally proposed an explanation of the superconducting gap anisotropy in FeSe/STO, which we did not discuss in detail here. Our analysis showed that the BZ sampling in experiment can potentially have a significant impact on the gap magnitude's angular distribution. For more details we refer to the paper.

Above we have seen that a large number of experimentally observed properties of FeSe/STO can be explained by assuming a small-**q** EPI. Besides realistic results for T_c and the gap magnitude, the replica band is found at the correct energies. Furthermore, our predictions concerning the temperature insensitivity of the FS and the second order replica band have been confirmed after the publication of Paper I [67, 68], which strengthens the confidence in our approach. However, due to the big controversy about the pairing mechanism in this system we wanted to explore the possibility that SFs might lead to equally convincing results in the superconducting state of FeSe/STO, and we discuss our findings in the next section.

3.2 Spin fluctuations

In Paper II we introduced a novel method for including SFs and charge fluctuations (CFs) into a full bandwidth, multiband and anisotropic Eliashberg theory of FeSe/STO. The derivation of interaction kernels was inspired by Graser et al. [32], which was the starting point for developing the fully self-consistent formalism in Matsubara space. In this work we neglected any potential influence of the small-**q** EPI, and solely focused on the spin and charge degrees of freedom. By doing so we wanted to examine the importance of SFs for superconductivity in FeSe/STO. Due to the novelty of our approach we applied it to bulk FeSe, a system in which SFs are commonly believed to mediate superconductivity, as benchmark. The electron energies for both systems are from here on considered in the unfolded BZ, compare Fig. 3.1.

3.2.1 Superconductivity in bulk FeSe

In the following we derive the interaction kernels entering the Eliashberg formalism, compare Eq. (2.15), and apply the theory to bulk FeSe. By diagonalizing the non-interacting Hamiltonian from Ref. [45] we get electron energies $\xi_{\mathbf{k},n}$ as eigenvalues, and matrix elements $a^{p}_{\mathbf{k},n}$ as eigenvectors for each momentum and energy band. From here the system's bare susceptibility can be calculated as

$$\begin{aligned} \mathrm{Im}\big[X^0_{\mathbf{q}}(\omega)\big]^{p,q}_{s,t} =& -\pi \sum_{n,n',\mathbf{k}} a^{s}_{\mathbf{k},n} a^{p*}_{\mathbf{k},n} a^{q}_{\mathbf{k}+\mathbf{q},n'} a^{t*}_{\mathbf{k}+\mathbf{q},n'} \\ & \times \big[n_F(\xi_{\mathbf{k},n}) - n_F(\xi_{\mathbf{k}+\mathbf{q},n'})\big]\,\delta(\xi_{\mathbf{k}+\mathbf{q},n'} - \xi_{\mathbf{k},n} + \omega), \end{aligned} \tag{3.4a}$$

$$\mathrm{Re}\big[X^0_{\mathbf{q}}(\omega)\big]^{p,q}_{s,t} = \frac{1}{\pi}\mathscr{P}\int_{-\infty}^{\infty} \frac{\mathrm{d}\omega'}{\omega' - \omega}\,\mathrm{Im}\big[X^0_{\mathbf{q}}(\omega')\big]^{p,q}_{s,t}, \tag{3.4b}$$

where $n_F(\cdot)$ is the Fermi-Dirac function, p, q, s, t describe orbitals, and $\mathscr{P}$ denotes the principal value. Due to the fact that the susceptibilities in Eq. (3.4) are rather robust against changes in temperature, we fix $T = 5\,\mathrm{K} < T_c$ and use $\hat{X}^0_{\mathbf{q}}(\omega)$ likewise at higher temperatures. Here we use the notation $\hat{X}$ to refer to four leg tensors in orbital space, and $[X]^{p,q}_{s,t}$ to specifically address the orbital content.

The spin and charge degrees of freedom enter our theory via the intraorbital onsite interaction U and the Hund's rule coupling J. These are used to calculate the interorbital onsite interaction $V' = U - 3J/4 - J'$ and pair hopping energy $J' = J/2$ [32, 33, 69]. Within this formalism we write the Stoner tensors for spin (S) and charge (C) as

$$\begin{aligned} &\big[U^S\big]^{a,a}_{a,a} = U, \ \big[U^S\big]^{a,a}_{b,b} = \frac{J}{2}, \ \big[U^S\big]^{a,b}_{a,b} = \frac{J}{4} + V', \ \big[U^S\big]^{b,a}_{a,b} = J', \\ &\big[U^C\big]^{a,a}_{a,a} = U, \ \big[U^C\big]^{a,a}_{b,b} = 2V', \ \big[U^C\big]^{a,b}_{a,b} = \frac{3J}{4} - V', \ \big[U^C\big]^{b,a}_{a,b} = J'. \end{aligned} \tag{3.5}$$

We use linear response theory for describing the spin and charge interactions. Within the Random Phase Approximation (RPA) the corresponding susceptibilities can be cast as

$$\hat{X}^S_{\mathbf{q}}(\omega) = \hat{X}^0_{\mathbf{q}}(\omega)\left[\hat{1} - \hat{U}^S \hat{X}^0_{\mathbf{q}}(\omega)\right]^{-1}, \tag{3.6a}$$

$$\hat{X}^C_{\mathbf{q}}(\omega) = \hat{X}^0_{\mathbf{q}}(\omega)\left[\hat{1} + \hat{U}^C \hat{X}^0_{\mathbf{q}}(\omega)\right]^{-1}, \tag{3.6b}$$

and carry full momentum, frequency and orbital dependencies.

To determine the possible choices for U and J we use Eq. (3.6) to define static susceptibilities $X^{S/C,\mathrm{stat}}_{\mathbf{q}} = \frac{1}{2}\sum_{p,s} \mathrm{Re}\big[X^{S/C}_{\mathbf{q}}(0)\big]^{p,p}_{s,s}$. The Stoner criterion dictates that, for valid U and J the system satisfies the conditions $X^{S,\mathrm{stat}}_{\mathbf{q}} > 0$ and $X^{C,\mathrm{stat}}_{\mathbf{q}} > 0 \ \forall \mathbf{q}$. Upon increasing values for the two Stoner parameters, an instability can be detected by either $X^{C,\mathrm{stat}}_{\mathbf{q}} \to 0$ (charge ordering) or $X^{S,\mathrm{stat}}_{\mathbf{q}} \to 0$ (spin density wave). In Fig. 3.3(a) we show a $U-J$ phase diagram with respect to the just mentioned conditions. The blue area represents all allowed choices of U and J, while the green and cyan regions mark divergences of the RPA susceptibilities due to charge and spin, respectively. The yellow area is forbidden because both $X^{C,\mathrm{stat}}_{\mathbf{q}}$ and $X^{S,\mathrm{stat}}_{\mathbf{q}}$ violate the Stoner criterion. We emphasize three ratios of U/J as solid purple, red and gray lines in Fig. 3.3(a), which are examined in Paper II. Here our focus lies on $J = U/2$ as one example.

We want to include the interaction kernels due to SFs and CFs in an Eliashberg formalism. To do so, we distinguish between the kernel used to calculate the superconductivity order parameter, label $(-)$, and the interaction for the dispersion renormalization functions, label $(+)$. In real-frequency space we compute

$$\left[V^{(+)}_{\mathbf{q}}(\omega)\right]^{p,q}_{s,t} = \left[\frac{3}{2}U^S X^S_{\mathbf{q}}(\omega)U^S + \frac{1}{2}U^C X^C_{\mathbf{q}}(\omega)U^C\right]^{t,q}_{p,s}, \tag{3.7a}$$

$$\left[V^{(-)}_{\mathbf{q}}(\omega)\right]^{p,q}_{s,t} = \left[\frac{3}{2}U^S X^S_{\mathbf{q}}(\omega)U^S + \frac{1}{2}U^S - \frac{1}{2}U^C X^C_{\mathbf{q}}(\omega)U^C + \frac{1}{2}U^C\right]^{t,q}_{p,s}, \tag{3.7b}$$

which are the couplings in orbital representation. The next step is to transform Eqs. (3.7) into band space, and afterwards apply the Kramers-Kronig relation to obtain functions in Matsubara space:

$$V^{(\pm)}_{\mathbf{q},n,n'}(\omega) = \sum_{\mathbf{k}}\sum_{s,t,p,q} a^{t*}_{\mathbf{k},n} a^{s*}_{\mathbf{k},n}\left[V^{(\pm)}_{\mathbf{q}}(\omega)\right] a^{p}_{\mathbf{k}-\mathbf{q},n'} a^{q}_{\mathbf{k}-\mathbf{q},n'}, \tag{3.8a}$$

$$V^{(\pm)}_{\mathbf{q},l,n,n'} = \frac{1}{\pi}\mathscr{P}\int_{-\omega_{\mathrm{cut}}}^{\omega_{\mathrm{cut}}} \frac{\mathrm{d}\omega}{\omega - iq_l}\mathrm{Im}\left[V^{(\pm)}_{\mathbf{q},n,n'}(\omega)\right]. \tag{3.8b}$$

Note, that we introduce a frequency cutoff ω_{cut} for neglecting the high-frequency Stoner continuum appearing in the magnon spectrum, as this generally sup-

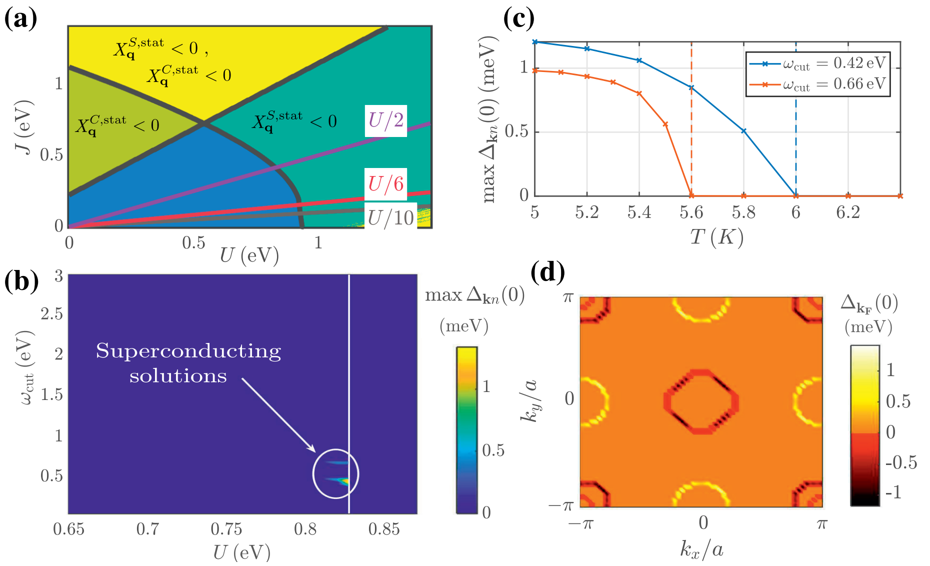

Figure 3.3. (a) Phase diagram for finding valid pairs of (U,J). The blue region represents the allowed phase space, while other regions are forbidden by the Stoner criterion. Three ratios U/J, which we considered in our work, are drawn explicitly as purple, red and gray lines. (b) Self-consistently calculated maximum superconducting gap at zero frequency as function of U and energy cutoff ω_{cut}, computed for $T = 5\,\mathrm{K}$ and $J = U/2$. (c) Temperature dependence of the superconducting gap for $J = U/2$, $U = 0.827\,\mathrm{eV}$ and ω_{cut} as written in the legend. (d) Fermi surface projection of the gap function, obtained for $(U,J) = (0.827\,\mathrm{eV}, U/2)$ and $\omega_{\mathrm{cut}} = 0.42\,\mathrm{eV}$ at $T = 5\,\mathrm{K}$. Figure taken from Paper II.

presses superconductivity. At this stage ω_{cut} is a free parameter, which we keep variable in order to find the largest critical temperatures.

Now we are in a position to solve the self-consistent set of Eliashberg equations for $Z_{\mathbf{k},n,m}$, $\chi_{\mathbf{k},n,m}$ and $\phi_{\mathbf{k},n,m}$, see Eq. (2.15), where the reader should be reminded on the additional minus sign entering the mathematical expression for $\phi_{\mathbf{k},n,m}$ compared to the electron-phonon case. With $\Delta_{\mathbf{k},n,m} = \phi_{\mathbf{k},n,m}/Z_{\mathbf{k},n,m}$ we show in Fig. 3.3(b) the maximum gap value at zero frequency as function of U and ω_{cut}, calculated at $T = 5\,\mathrm{K}$. It is directly apparent that only a small subset of possible choices for the Stoner parameter and frequency cutoff allow for superconductivity at the current temperature. As guide for the eye, we draw the limit of U due to the Stoner criterion as vertical line.

In Fig. 3.3(c) we examine closer the temperature dependence of Δ for two cutoff frequencies, at which a superconducting state is possible, according to panel (b). With interaction strength $U = 0.827\,\mathrm{eV}$ we find the largest $T_c = 6\,\mathrm{K}$ at $\omega_{\mathrm{cut}} = 0.42\,\mathrm{eV}$. This result is in good agreement with the experimental value of 8 K [34]. The self-consistently obtained BZ symmetry of the order parameter is shown in Fig. 3.3(d), where we project the zero-frequency component of the gap function onto the FS ($T = 5\,\mathrm{K}$, $\omega_{\mathrm{cut}} = 0.42\,\mathrm{eV}$). We observe a sign change between electron and hole pockets, and an additional small asymmetry, giving rise to a $s_{\pm} + s$-wave gap, compatible with experiment [70]. This momentum space structure is expected from FS nesting, which gives rises to a dominant repulsive interaction at $\mathbf{q} = (0, \pi)$ in the equation for the order parameter. Lastly, our computed maximum gap magnitude of 1.4 meV deviates only slightly from the experimentally observed 1.67 meV [70, 71].

From the benchmark results presented above we conclude that the applied method to include SFs and CFs in an Eliashberg framework is reliable and leads to realistic results in comparison to experiment. Besides the reasonable values for the superconducting T_c and maximum gap size, we also find the correct BZ symmetry of the order parameter. Next, we apply the here introduced formalism to FeSe/STO.

3.2.2 Spin fluctuations in FeSe/STO

For the monolayer case we use the same approach as described in Section 3.2.1 and employ the electron dispersion shown in Fig. 3.1(b), i.e. the FS now consists only of electron pockets while the hole bands were shifted down in energy. The nesting wave vector in the unfolded BZ is given by $\mathbf{q} = (\pi, \pi)$. Therefore, it is expected that the most coherent and dominant contributions in static and dynamic susceptibilities can be found around this exchange wave vector, which is confirmed by our data. The coupling between electron and hole bands is less prominent due to the fact that the latter lie substantially below the Fermi level. This situation describes the incipient band coupling scenario introduced in Ref. [52], and we will further comment on it later. The

RPA susceptibilities in Eqs. (3.6) are calculated at $T = 5\,\mathrm{K}$ and we find the available phase space for U and J from the Stoner criterion, as was done in connection to Fig. 3.3(a). As it turns out, the shape of the allowed parameter region is rather similar to the case of bulk FeSe, with the difference that the scales on both U and J axes are slightly larger. In the following we examine the choices $J = U/10$, $J = U/6$ and $J = U/2$ closer ($J \leq U/2$ [53, 72]).

To find the optimal parameters for a large critical temperature we explore the phase space spanned by U and ω_{cut} in Fig. 3.4(a-c), where each panel corresponds to a different U/J ratio. The plotted maximum superconducting gap is obtained by solving the full Eliashberg equations for SFs and CFs for each parameter set. We observe that an increase in Hund's rule coupling J leads to a smaller phase space that allows for superconductivity (at $T = 5\,\mathrm{K}$), while the gap magnitudes increase. The inset of panel (a) shows the evolution of Δ as U approaches the Stoner instability, for two cutoff frequencies. From this we learn that the gap magnitude does not arbitrarily increase close to the instability, even though the maximum coupling values have no upper bound. We will come back to this aspect later in more detail.

For $U = 1.5802\,\mathrm{eV}$ and $J = U/10$, we project the zero frequency superconducting gap onto the renormalized FS in Fig. 3.4(d) and find a sign change between the electron pockets, giving rise to a nodeless d-wave symmetry. The

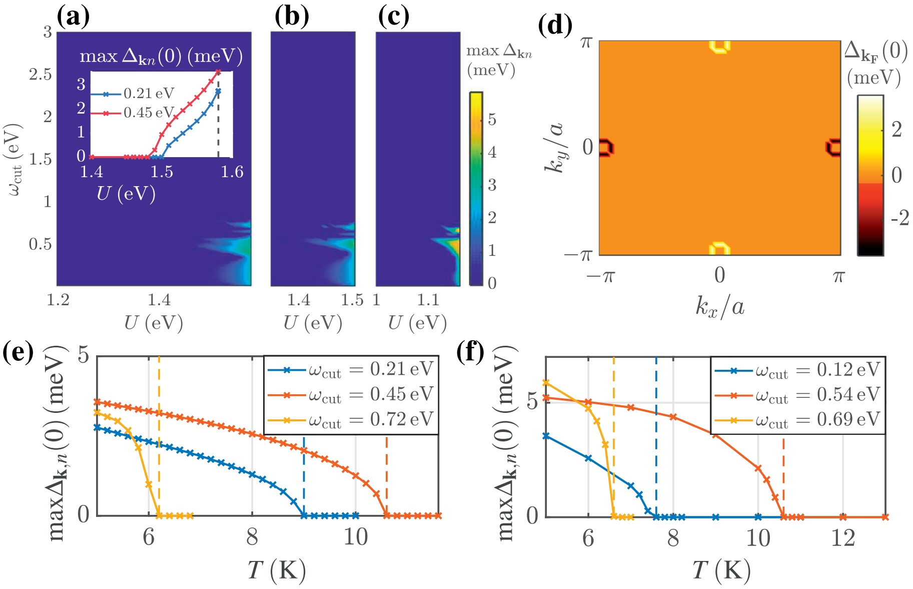

Figure 3.4. (a), (b), (c) Maximum superconducting gap at $T = 5\,\mathrm{K}$. (a) $J = U/10$, the inset shows the gap as function of U for two cutoff frequencies. (b) $J = U/6$. (c) $J = U/2$. (d) Fermi surface projection of the superconducting gap, calculated at $T = 5\,\mathrm{K}$, $J = U/10$, $U = 1.5802\,\mathrm{eV}$ and $\omega_{\text{cut}} = 0.45\,\mathrm{eV}$. (e), (f) Temperature dependence of the superconducting gap for cutoff frequencies as written in the legends. (e) $(U, J) = (1.5802\,\mathrm{eV}, U/10)$. (f) $(U, J) = (1.16\,\mathrm{eV}, U/2)$. Figure taken from Paper II.

same result is found for all the parameter space explored in Paper II, and it is compatible with some (but not all) experiments [61–63]. However, the superconducting gap magnitude is clearly too small compared to the well established picture in FeSe/STO [73, 74]. A similar conclusion emerges in connection to the superconducting critical temperature, which we determine in Fig. 3.4(e) and (f) for $J = U/10$ and $J = U/2$, respectively, for different frequency cutoffs. The choices for ω_{cut} are motivated from the phase space exploration in Fig. 3.4(a) and (c), so as to maximize the respective T_c. For parameters considered here, the critical temperatures do not exceed 10.6 K, which is too small to account for the record values of T_c in FeSe/STO [48, 54, 75].

As apparent from the above results, directly applying our Eliashberg formalism to FeSe/STO with pairing due to SFs and CFs does not lead to the correct characteristics of the superconducting state. To exclude the possibility that this is only due to details of our input electron dispersions, we studied different variations of $\xi_{\mathbf{k},n}$. One possible critique on the tight-binding model employed here, compare Fig. 3.1(b), is that the FS pockets are too small in comparison to experiment. Therefore we repeated the entire analysis for a rigidly shifted energy dispersion, denoted by $\xi_{\mathbf{k},n} - \mu$ in Paper II. A second potential inaccuracy of our tight-binding model is the distance in energy between electron and hole bands, which does not precisely match experiment [54]. For this reason we constructed energies $\xi_{\mathbf{k},n} - \delta\mu$, which is obtained from the original $\xi_{\mathbf{k},n}$ by shifting only the hole bands closer to the Fermi level via a non-rigid shift $\delta\mu$. In this case one needs to be careful to recalculate the matrix elements.

Testing these two dispersions $\xi_{\mathbf{k},n} - \mu$ and $\xi_{\mathbf{k},n} - \delta\mu$ leads to larger and smaller regions, respectively, in U-ω_{cut}-space, that allow for superconductivity at 5 K, while the gap magnitude is increased in both cases. For the rigidly shifted energies we find a maximum $T_c \sim 8.3$ K, which is a decrease compared to the above reported 10.6 K. This can be explained by the fact that the coupling between electron and hole bands is significantly reduced, as the hole bands are shifted to energies far below the Fermi level. This aspect is addressed further below. A slight increase in $T_c \sim 11.4$ K is observed for the input $\xi_{\mathbf{k},n} - \delta\mu$, which is due to an enhancement of incipient band coupling. However, for both modifications of the electron dispersions the critical temperatures are still incompatible with experiment.

We also wanted to check more explicitly the influence of incipient band pairing on the critical temperatures, as this was proposed as main mechanism for driving the high-temperature superconductivity in FeSe/STO [52]. For this purpose we took the original dispersion $\xi_{\mathbf{k},n}$, calculated the RPA susceptibilities and spin/charge fluctuation kernels, and neglected all hole bands on the level of Matsubara frequency dependent interactions, see Eq. (3.8). For two cutoffs $\omega_{\mathrm{cut}} = 0.21$ eV (blue) and $\omega_{\mathrm{cut}} = 0.45$ eV (red) we show the resulting temperature dependence of the maximum superconducting gap in Fig. 3.5 as solid lines. As a reference we show as dashed lines the results corresponding to the full dispersions (including the hole bands). For both examples of ω_{cut}

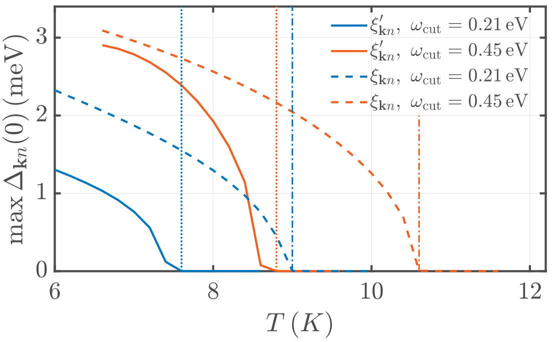

Figure 3.5. Temperature dependence of the maximum superconducting gap, calculated for $J = U/10$ and $U = 1.5802\,\mathrm{eV}$. Blue and red curves correspond to cutoffs $\omega_{\mathrm{cut}} = 0.21\,\mathrm{eV}$ and $\omega_{\mathrm{cut}} = 0.45\,\mathrm{eV}$, respectively. Dashed lines are obtained by using the full electron dispersion, while solid curves represent results for dispersion $\xi'_{\mathbf{k},n}$, where the hole bands are neglected. Figure taken from Paper II.

we find that around 85% of the magnitude of T_c is due to the electron bands only. Together with the above findings for $\xi_{\mathbf{k},n} - \delta\mu$ we conclude that the role of incipient band pairing in FeSe/STO is rather minor and cannot account for the high critical temperature.

Before ending this subsection it is worth discussing the limiting behavior of the maximum gap size when $U \to U^{\mathrm{crit}}$, i.e. when we consider the system close to the Stoner instability. From numerical fits to our data we found that the effective interaction strength at exchange wave vector $\mathbf{q} = (\pi, \pi)$ scales approximately like

$$V \sim \frac{U^2}{U^{\mathrm{crit}} - U}. \tag{3.9}$$

Considering the mass renormalization and superconducting order parameter on the FS under various simplifications, such as treating the effective interaction entering the Eliashberg equations as delta-peak, we arrive at approximate scaling laws for Z and gap function Δ:

$$Z_{\mathbf{k}_\mathrm{F}} \sim \frac{1}{2} + \sqrt{\frac{1}{4} + \frac{V}{\pi^2 T}}, \tag{3.10a}$$

$$\Delta_{\mathbf{k}_\mathrm{F}} \sim \sqrt{\frac{TV}{Z^2_{\mathbf{k}_\mathrm{F}}} - \pi^2 T^2}. \tag{3.10b}$$

We test the validity of Eqs. (3.10) in Fig. 3.6, where we show our data (solid red) and the fitting functions (dotted blue) for $Z_{\mathbf{k}_\mathrm{F}}$ and $\Delta_{\mathbf{k}_\mathrm{F}}$ in panels (a) and (b), respectively, at $T = 5\,\mathrm{K}$, $J = U/10$ and $\omega_{\mathrm{cut}} = 0.45\,\mathrm{eV}$ for U close to the instability.

The proposed scalings match our data to very good degree, increasingly so as $U \to U^{\mathrm{crit}}$. We find that the mass renormalization diverges as the system

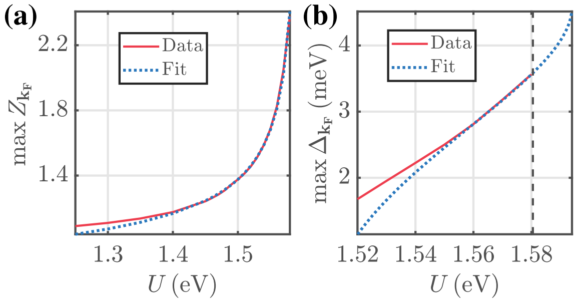

Figure 3.6. Using $T = 5\,\mathrm{K}$, $J = U/10$ and $\omega_{\mathrm{cut}} = 0.45\,\mathrm{eV}$, we show in (a) and (b) the maximum values of the mass renormalization and superconducting gap, respectively, as function of U. Figure taken from Paper II.

develops a spin density wave instability. The same holds true for the superconductivity order parameter ϕ (not shown). However, since the gap function is given as ratio between Z and ϕ, Δ stays finite regardless of how closely U approaches its maximum value. This means that there exists an upper bound for the gap magnitude, which is approximately given by $\max_U \Delta_{\mathbf{k}_F} = 3.585\,\mathrm{meV}$ for the chosen set of parameters. Such a constraint on the pairing strength can not be found in BCS theory, where arbitrarily large values of Δ can be constructed (see Paper II), and it puts also an upper limit on the possible influence of SFs on the Cooper pairing strength in this system.

3.3 Multichannel superconductivity

After the advances of Paper I and II the next logical step was to combine the two approaches into a multichannel Eliashberg theory of FeSe/STO, i.e. into a formalism that treats electron-phonon and spin/charge interactions on equal footing. To achieve this we consider the Eliashberg Eqs. (2.13) which we solve here with the interaction kernels

$$K^{(\pm)}_{\mathbf{q},l,n,n'} = V^{(\mathrm{eph})}_{\mathbf{q},l,n,n'} \pm V^{(\pm)}_{\mathbf{q},l,n,n'}. \tag{3.11}$$

In the equations for electron energy renormalizations $Z_{\mathbf{k},n,m}$ and $\chi_{\mathbf{k},n,m}$ we use $K^{(+)}_{\mathbf{q},l,n,n'}$, while the superconductivity order parameter depends on $K^{(-)}_{\mathbf{q},l,n,n'}$, which is due to the fact that the electronic interactions enter the equation for $\phi_{\mathbf{k},n,m}$ in a repulsive way. In Eq. (3.11) $V^{(\mathrm{eph})}_{\mathbf{q},l,n,n'}$ is the small-$\mathbf{q}$ EPI introduced in Section 3.1, which scales like the scattering strength g_0 and is approximated as band-independent. On the other hand, $V^{(\pm)}_{\mathbf{q},l,n,n'}$ describes the coupling due to

SFs and CFs as explained in Section 3.2, where we fix $J = U/2$[1] so that the interaction strength can be controlled solely by U.

We first solve the multichannel Eliashberg equations at $T = 5\,\mathrm{K}$ as function of g_0 and U. The self-consistent results for $\Delta = \max_{\mathbf{k},n}\Delta_{\mathbf{k},n,m=0}$ are shown in Fig. 3.7(a). The inset of this panel contains the BZ dependence of the superconducting gap, giving rise to a nodeless d-wave symmetry, which is the same as found for all the parameter space except $U = 0$ (compare Section 3.1). While the gap magnitude is rather insensitive to changes in U, we observe an increase of Δ with g_0. In the following we choose a reference value of $\Delta \simeq 12\,\mathrm{meV}$, represented by the dashed red line, which is compatible with experiment [47, 54] and provides us with different (U, g_0) pairs for closer examination.

In Fig. 3.7(b) we show the temperature dependence of Δ for various choices of U (see legend) and the corresponding scattering strengths, such that we move on the red dashed line in panel (a). For a small to moderate influence of SFs we find a critical temperature slightly above 60 K, while T_c is decreased upon growing U. The observed suppression of superconductivity stems from a competition between small-$\mathbf{q}$ EPI and intra-pocket contributions to the SF kernel peaked around $\mathbf{q} = (0, 0)$, which enter the equation for ϕ (or equivalently Δ) with opposite signs.

To check which parameters give the most accurate results in comparison to experiment, we plot the ratio $\Delta/k_B T_c$ as function of U in Fig. 3.7(c) as open blue circles, where the values of g_0 have been chosen according to the red

---

[1] This choice was made for obtaining the largest possible influence due to SFs, according to the analysis in Paper II.

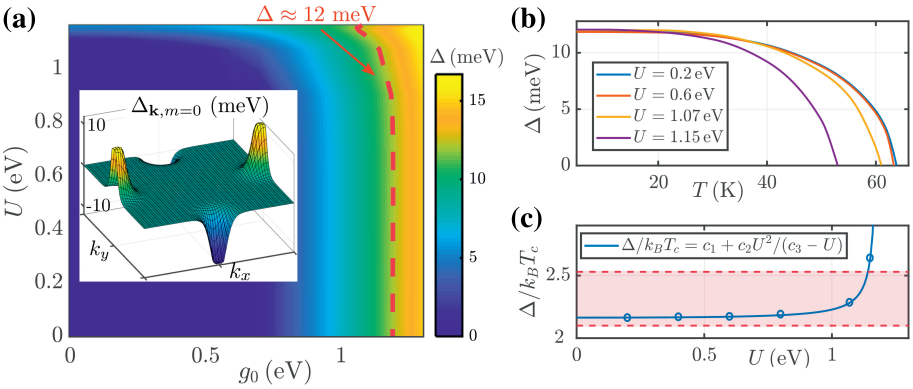

Figure 3.7. (a) Maximum superconducting gap at $T = 5\,\mathrm{K}$ as function of U and g_0. (b) Temperature dependence of Δ for different values of U as indicated in the legend. (c) Gap to T_c ratio as function of U. Open circles represent our computed results, the solid line is a numerical fit. The red area represents values for $\Delta/k_B T_c$ compatible with experiment [73, 75]. Figure taken from Paper III.

dashed line of Fig. 3.7(a). The red area marks acceptable results for $\Delta/k_B T_c$ compared to Refs. [73, 75]. We see that relatively low values of U place our results into the correct range, while $\Delta/k_B T_c$ grows too large as we approach the Stoner instability. We can therefore conclude that potential influences of SFs and CFs in FeSe/STO are limited, which means that the electron-phonon mechanism is mainly responsible for the high critical temperature and gap magnitude. According to our results and in agreement to recent measurements [61–63], the most plausible BZ symmetry of the superconducting order parameter is nodeless d-wave, which has its origin in the repulsive SFs interaction, peaked at $\mathbf{q} = (\pi, \pi)$.

It is noteworthy that, briefly after the publication of Paper III, Rademaker et al. took on similar calculations for FeSe/STO, treating the electron-phonon and SFs mechanisms on the same footing [76]. Their approach differed from ours in that the spin and charge susceptibilities were updated self-consistently, which is known as Fluctuation Exchange formalism, or FLEX. However, due to the higher computational costs compromises had to be made for the number of orbitals kept. In their approach several different gap symmetries are possible, depending on the parameter choices [76], and the true outcome will have to be determined in future theoretical and experimental investigations.

To summarize our results of the current Chapter, we described the advances of Papers I, II and III, in which we applied full-bandwidth Eliashberg theory to explain the superconducting state of FeSe/STO. When imposing small-$\mathbf{q}$ EPI in Paper I, it is possible to obtain correct values for T_c and the superconducting s-wave gap magnitude. Further, we calculated the temperature dependence of ARPES spectra, the global chemical potential and the renormalized FS, all in good agreement to experiment. The predicted second order replica band has since been experimentally confirmed [67]. As a side remark, the electron-phonon mechanism also leads to accurate tunneling spectra [58].

Considering only SFs and CFs as possible mediators of superconductivity leads to a severe underestimation of the gap magnitude and T_c, compared to experiment. From the results of Paper II we cannot deduce whether such bosons might also lead to the observed replica bands. To test this aspect, one would need to derive a self-consistent analytic continuation procedure similar to the electron-phonon case. Our calculations lead to a nodeless d-wave gap symmetry, and we further were able to exclude the incipient band scenario as a driving force for high-temperature superconductivity in this system. In Paper III we combined the two earlier approaches in a multichannel Eliashberg framework. Our results confirmed the earlier observations, in that the electron-phonon mechanism is responsible for the large T_c. From our analysis we learn that SFs suppress superconductivity in this system and generally play a subdominant role. However, the d-wave symmetry of the order parameter is a signature of such interactions. Looking ahead to Part II of this thesis, it deserves to be mentioned that vertex-corrected Eliashberg theory of electron-phonon interaction can similarly lead to unconventional gap symmetries.

4. Twisted bilayer graphene

> *If we know exactly where we're going, exactly how to get there, and exactly what we'll see along the way, we won't learn anything.*
>
> M. Scott Peck

In the current Chapter we summarize Papers IV and V, in which we studied the interacting state of Twisted Bilayer Graphene (TBG). In this system two single layers of graphene are rotated with respect to each other by an angle Θ, which produces a Moiré pattern in real space, shown in Fig. 4.1(a). To capture the symmetry of this system requires to consider large unit cells (in comparison to the system without any twist), leading to a so-called mini-BZ in reciprocal space, which we assume from here on. At a certain 'magic angle', $\Theta \sim 1.1^\circ$, there are two flat bands emerging in the electronic spectrum close to the Fermi level, giving rise to van Hove singularities and a heavily increased magnitude of the electronic Density of States (DOS) [77,78]. In 2018 the group of Jarillo-Herrero discovered that TBG becomes superconducting at the magic angle, with a transition temperature of $T_c \simeq 1.7\,\mathrm{K}$ [79]. Superconductivity in this system is strongly dependent on the electron filling, and by changing the charge carrier density TBG can be turned into a Mott insulator [80]. These findings have triggered an enormous research interest in TBG, leading to many extensive studies thereafter [81–85].

In our work we discussed the role of electron-phonon interaction (EPI) in flat band systems, and in particular in TBG, using full-bandwidth multiband Eliashberg theory. The superconducting state of this system is the main subject of Paper IV, which we summarize in Section 4.1. Afterwards we present in Section 4.2 a cascade of replica bands generically occurring when the phonon energy scale is much greater than that of the electrons, such as it is the case for TBG. These are the findings of Paper V.

From here on we use a ten band tight-binding model for the electron energies, which was introduced in Ref. [87] and qualitatively agrees with characteristics of the continuum model [77,88,89] and *ab initio* calculations [90,91]. The energy dispersions along high-symmetry lines of the Brillouin zone (BZ) are shown in Fig. 4.1(b). Panel (c) of the same figure is an enlarged view of the two flat bands close to the Fermi level. As clearly seen from Fig. 4.1(d), the respective DOS peaks at chemical potentials μ_e and μ_h, which are indicated

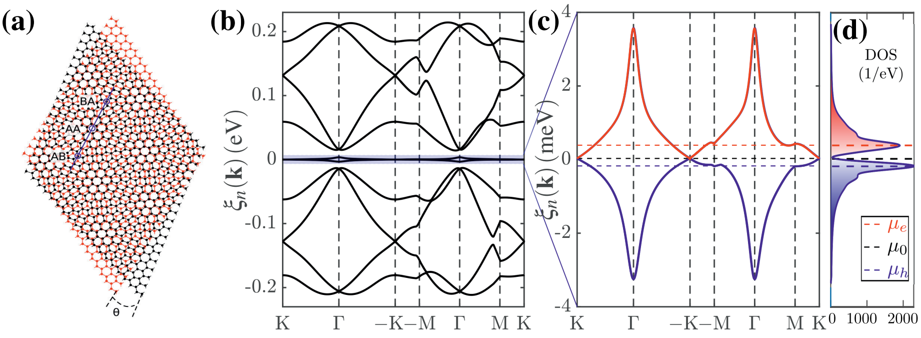

Figure 4.1. (a) Schematic of two monolayers of graphene with a relative twist Θ, taken from Ref. [86]. (b) Ten band electron dispersion reconstructed from Ref. [87] with $\Theta = 1.05°$. (c) Magnification of the two flat bands in panel (b) close to the Fermi level. (d) Density of states of the two flat bands. (b),(c),(d) taken from Paper IV.

as dashed horizontal lines. By comparison to panel (c) we learn that the DOS reaches its maximum values where the two bands are also locally flat (between $-$K and $-$M, M and K, Γ and M).

We assume here an interlayer phonon mode of $\Omega = 11\,\text{meV}$ [92, 93] that couples isotropically to the electron degrees of freedom, $g_{\mathbf{q}} = g_0$. It is noteworthy that the two flat bands extend over an energy interval of approximately 7 meV, and therefore Ω is the dominant energy scale of the system. In both Sections we solved the full bandwidth Eliashberg equations self-consistently in Matsubara space and analtyically continued the results to real frequencies, see Eqs. (2.13) and (2.23). If not further specified we used these outcomes for computing the optical spectra comparable to Angular Resolved Photoemission Spectroscopy (ARPES) and Scanning Tunneling Spectroscopy (STS).

4.1 Superconductivity from electron-phonon interaction

In the project that led to Paper IV we studied the effect of isotropic EPI in the superconducting state of TBG, using the ten band tight-binding model shown in Fig. 4.1. As mentioned above, flat band systems are unusual superconductors in that the phonon energy scale dominates over the electronic degrees of freedom, i.e. Ω is larger than the electron bandwidth. Such prerequisites requires to go beyond standard approximations of BCS theory, where only a narrow window around the Fermi level is taken into account. Even though some authors have suggested the importance of EPI in TBG before our work [86, 92, 94], a solution to full-bandwidth Eliashberg equations had not been attempted.

Superconductivity in TBG was originally discovered only for negative values of the electron density [79], but later studies found a finite T_c for both hole and electron doping [81, 95], see Fig. 4.2(a). For this reason we performed a phase space exploration as function of temperature and over a wide range of electron fillings, using an isotropic electron-phonon scattering strength $g_0 = 1.5\,\mathrm{meV}$. As for $\xi_n(\mathbf{k})$ we kept only the two bands close to the Fermi level, but carefully checked that our conclusions do not change when more states are considered. Our results for the gap edge $\Delta(0) \simeq \max_{\mathbf{k}}\Delta(\mathbf{k}, \omega_{m=0})$, which we obtained by solving the self-consistent Eqs. (2.13) for each parameter set, are shown in Fig. 4.2(b). There are two domes emerging, with maximum values of $\Delta(0)$ at $n^{(h)}$ and $n^{(e)}$, corresponding to the chemical potentials mentioned earlier in connection to Fig. 4.1(d). The electron filling $n^{(0)}$ is obtained when the chemical potential is chosen as $\mu = 0\,\mathrm{eV}$.

There are several important aspects that we learn from Fig. 4.2(b). First, the two domes are not symmetric which stems from the particle-hole asymmetry of the tight-binding model, compare panels (c) and (d) in Fig. 4.1, and coincides with experimental observations. Second, we find superconductivity almost throughout the entire range of electron densities considered here, which is in contrast to Fig. 4.2(a). However, this result is easily explained by the fact that our Eliashberg formalism does not include strongly correlated physics, such as to account for the Mott insulating states. Third, the maximum values for $T_c \sim 1\,\mathrm{K}$ have the correct order of magnitude when compared to experiment [79, 81]. More importantly even, the critical temperature is maximized at chemical potentials $\mu^{(e)}$ and $\mu^{(h)}$, which correspond to the aforementioned locally constant energies of the upper and lower flat bands, respectively, at which the DOS peaks.

The full-bandwidth Eliashberg formalism employed in Paper IV allows us to examine the distribution of the superconducting gap along the energy axis. To do so we map the self-consistent solutions for $Z(\omega)$, $\chi(\omega)$ and $\phi(\omega)$ to $Z[\tilde{\xi}_n(\mathbf{k})]$, $\chi[\tilde{\xi}_n(\mathbf{k})]$ and $\phi[\tilde{\xi}_n(\mathbf{k})]$, respectively. In Fig. 4.2(c) we show the projection of the superconducting gap (as usual, $\Delta = \phi/Z$) for electron filling $n = n^{(e)}$ onto the renormalized band structure, which is given by

$$\tilde{\xi}_n(\mathbf{k}) = \frac{\xi_n(\mathbf{k}) - \mu + \chi[\tilde{\xi}_n(\mathbf{k})]}{Z[\tilde{\xi}_n(\mathbf{k})]}. \tag{4.1}$$

Remarkably, the largest magnitude of Δ is found farthest away from the Fermi level, both below and above zero energy. Additionally, the pairing amplitude is positive throughout the entire electron bandwidth, which is different from the more common situation of dominating electron over phonon energy scales [96].

Before moving to the results of Paper V, it is worth mentioning another consequence of including the entire bandwidth in our theory. As is well known, superconductivity leads to a Meissner effect that is characterized by a finite superfluid weight D_s [97]. BCS theory for flat band systems predicts, however, a vanishing superfluid density in the superconducting state. A solution

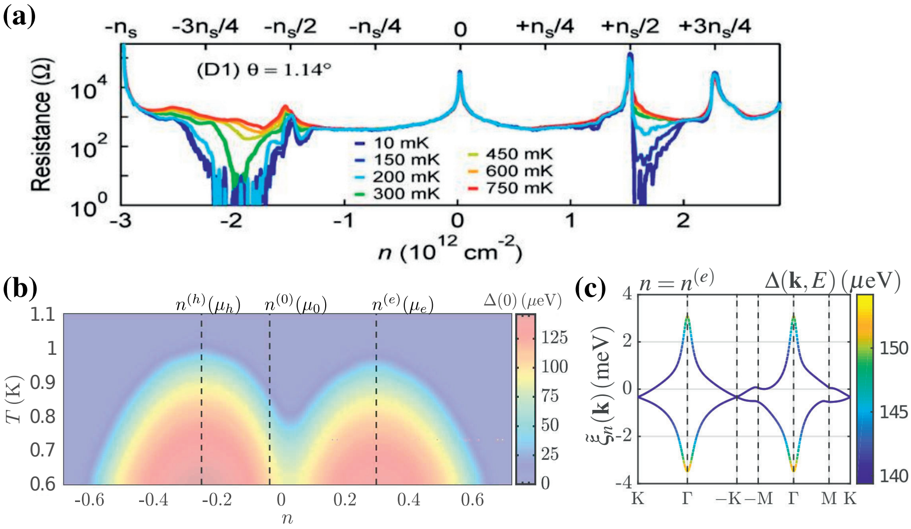

Figure 4.2. (a) Electrical resistance as function of charge carrier density in TBG, shown for various temperatures as written in the legend. Graph taken from Ref. [81]. (b) Self-consistently calculated temperature and electron filling dependent maximum superconducting gap. (c) Projection of the superconducting gap function onto the renormalized electron band structure. (b),(c) were taken from Paper IV.

to this problem has been proposed in Ref. [98], where additional geometrical contributions lead to a finite D_s. The results of our self-consistent calculations allow us to offer an alternative solution to this problem: Indeed, when confining the electron energies to a narrow window around the Fermi level, we find very small values for the superfluid density. However, as this energy window increases up to the electron bandwidth, D_s clearly becomes non-zero, therefore naturally leading to a conventional Meissner effect. In other words, due to our interpretation the vanishing superfluid density in flat band systems is only an artifact of BCS theory, and can be resolved by including a larger energy range in the formalism.

To conclude, in Paper IV we studied the superconducting state of TBG using full-bandwidth Eliashberg theory for an optical phonon mode that is isotropically coupled to the electron energies. In agreement to experiment we find two asymmetric superconducting domes as function of the electron density, leading to realistic values for T_c. We further predicted various STS features, which should be experimentally accessible. Finally, we showed that full bandwidth Eliashberg calculations lead to prominent Cooper pairing away from the Fermi level and naturally give rise to a finite superfluid density, hence ensuring a robust Meissner effect.

4.2 Replica bands

In Paper V we discussed the formation of replica bands due to EPI in flat bands systems, and in particular in TBG. To introduce this effect we use a nearest neighbor tight-binding description $\xi(\mathbf{k}) = -2t[\cos(k_x) + \cos(k_y)] - \mu$ as model system for the electron energies. With hopping energy $t = 0.425\,\text{meV}$ and chemical potential $\mu = -1\,\text{meV}$ we obtain an electron bandwidth of $W = 3.4\,\text{meV}$. In accordance to TBG discussed in the previous Section 4.1, we choose an optical phonon frequency of $\Omega = 11\,\text{meV}$, which is therefore the dominant energy scale, $\Omega > W$. With these parameters and an isotropic electron-phonon coupling strength $g_0 = 2\,\text{meV}$, we solved the Eliashberg equations in Matsubara space at $T > T_c$, analytically continued the results to the real frequency axis and calculated the spectral function via Eq. (2.25a) with a smearing of $\delta = 0.01\,\text{meV}$.

The frequency and momentum dependent outcome $A(\mathbf{k}, \omega)$ is shown in Fig. 4.3(a). The main energy band creates the signal close to zero frequency, while all the remaining features are naturally occurring from our self-consistent calculations. A closer inspection reveals that these features are replications of the original band and approximately occur at multiples of the phonon frequency. By summing the spectral function over the momentum degree of freedom we find the differential conductance shown as solid blue line in Fig. 4.3(b). Here we neglect the frequency range $|\omega| \leq W/2$ for better visibility of the quasiparticle features. From this result it is apparent that the replica bands generate clear signals not only in the ARPES, but also the STS spectrum.

To better understand the origin of the observed additional quasiparticle bands, we can rewrite the spectral function as

$$A_n(\mathbf{k}, \omega) = \frac{1}{\pi} \mathrm{Im} \left\{ \frac{1}{Z(\omega)} \frac{1}{\omega + i\delta - \tilde{\xi}_n(\mathbf{k}, \omega)} \right\}, \tag{4.2}$$

where we inserted the explicit form of the electron Green's function into Eq. (2.25a), defined $\tilde{\xi}_n(\mathbf{k}, \omega) = (\xi_n(\mathbf{k}) + \chi(\omega))/Z(\omega)$, and took into account that

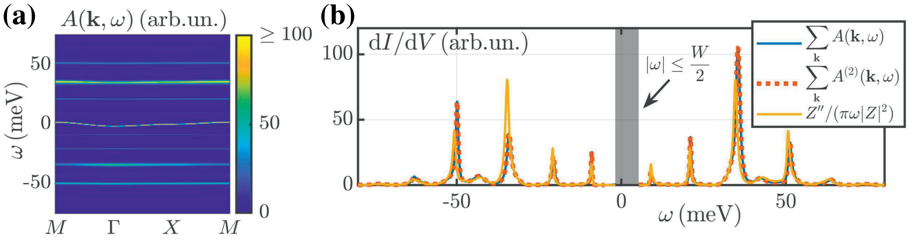

Figure 4.3. (a) Frequency dependent spectral function for our flat-band model dispersion, obtained at $T > T_c$, plotted along high-symmetry lines of the BZ. (b) Tunneling spectrum corresponding to panel (a), calculated from different levels of approximation as written in the legend. Figure taken from Paper V.

$\phi(\omega) = 0$ due to $T > T_c$. To make further progress it is useful to divide the frequency axis into ranges $|\omega| \leq W/2$ and $|\omega| > W/2$, which are treated separately in the following. It is well known that within the electron bandwidth, $|\omega| \leq W/2$, the ARPES spectrum can be reconstructed via a collection of coherent excitations, characterized by

$$A_n^{(1)}(\mathbf{k}, |\omega| \leq W/2) \simeq \frac{1}{Z'(\omega)} \delta(\omega - \tilde{\xi}_n'(\mathbf{k}, \omega)). \tag{4.3}$$

The result of Eq. (4.3) is the quasiparticle band at the Fermi level in Fig. 4.3(a), and is not shown in panel (b) of the same figure (gray area).

For frequencies outside the electron bandwidth we can express the spectral function as

$$A_n^{(2)}(\mathbf{k}, |\omega| > W/2) = \frac{1}{\pi} \frac{\omega Z''(\omega) - \chi''(\omega)}{|\omega Z(\omega) - [\xi_n(\mathbf{k}) + \chi(\omega)]|^2}, \tag{4.4}$$

where we use the notation $f' = \mathrm{Re}(f)$ and $f'' = \mathrm{Im}(f)$ for any function f. To show that Eq. (4.4) indeed reproduces our full results, we show the momentum average of $A_n^{(2)}(\mathbf{k}, \omega)$ as red dotted curve in Fig. 4.3(b), which falls precisely on top of the blue line. It turns out that the essential prerequisite for creating the replica bands is the mass renormalization function. This can be seen by writing the spectral function at $|\omega| > W/2$ as

$$A_n^{(2)}(\mathbf{k}, |\omega| > W/2) \simeq \frac{1}{\pi\omega} \frac{Z''(\omega)}{|Z(\omega)|^2}, \tag{4.5}$$

which is found from Eq. (4.4) by neglecting the electron dispersion and the chemical potential. As can be seen from the solid yellow line in Fig. 4.3(b), Eq. (4.5) leads to accurate peak positions in the differential conductance, while the height of each signal is slightly deviating from the full result. Therefore we can safely conclude that the mass renormalization function is responsible for mediating the replica bands in our toy model system, while the correct spectral weights are found upon inclusion of the chemical potential renormalization.

Next, we test the formation of replica bands in a more realistic system, namely TBG. As seen from Fig. 4.1 and the discussion of Section 4.1, TBG shares several characteristics with our model system, because the phonon frequency ($\Omega = 11\,\mathrm{meV}$) exceeds the electron bandwidth of the two flat bands ($W = 7\,\mathrm{meV}$). Further, there is a large energy gap of more than 20 meV between the two flat bands and the neighboring occupied and unoccupied states, which opens the possibility of detecting replica bands that are not superimposed on the rest of the energy dispersions. To test this hypothesis we set $g_0 = 1.6\,\mathrm{meV}$ and perform similar calculations as above, at temperature $T = 1.6\,\mathrm{K} > T_c$.

To observe whether replica bands can form in TBG we first consider the results for the differential conductance in Fig. 4.4(a), which were obtained by considering only the two flat bands. The three different colors correspond to electron fillings as described in connection to Fig. 4.1(d). The gray dashed lines indicate multiples of the optical phonon frequency Ω, and we do indeed find the expected cascade of replica bands at positive and negative frequencies. The gray shaded area corresponds to the bandwidth of the flat bands, and we show the results for this frequency range in panel (b). We see that chemical potential shifts on the energy scale of the current electron energies do not affect the position $p\Omega$ ($p \in \mathbb{Z}\backslash\{0\}$) of the replica band signals, which is due to the fact that $\Omega > W$.

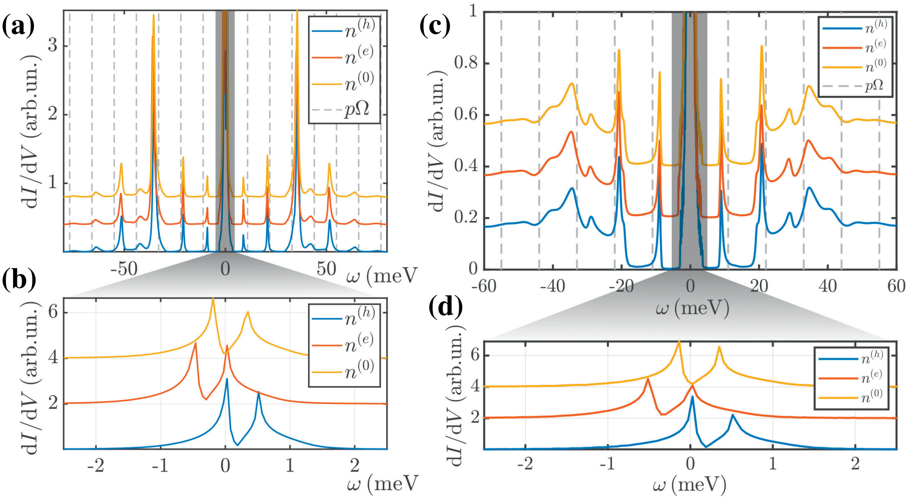

Figure 4.4. (a) Differential conductance in TBG for three different electron fillings (vertically shifted), calculated at $T = 1.6\,\mathrm{K}$. (b) Magnified view of $\mathrm{d}I/\mathrm{d}V$ on the energy scale of the two flat bands. (c),(d) same as (a),(b), but calculated from the four band electron dispersion. Figure taken from Paper V.

Having witnessed that replica bands can exist in TBG, we wanted to check if the inclusion of other energy bands would distort the signals. To do so we considered two additional bands, one occupied and one unoccupied, that are closest to the two flat bands. This dispersion has a bandwidth of $W = 127\,\mathrm{meV}$, hence $W > \Omega$. However, the phonon frequency still dominates over the energy scale of the flat bands. Our results for $\mathrm{d}I/\mathrm{d}V$ are shown in Fig. 4.2(c) where we chose again the three characteristic values for the electron filling. A zoom of the small frequency region is drawn in panel (d). The non-flat bands are located at approximately $\pm 20\,\mathrm{meV}$, and their signals are superimposed with the replica peaks. Nevertheless, at both positive and negative energies we can resolve the replica bands at $p = \pm 1, \pm 2, \pm 3$ and therefore can confidently predict their detection in tunneling experiments.

We carefully checked that the replica bands are robust with respect to the superconducting state. Further, we performed a variation in the phonon frequency for the model system, and found that the distance between neighboring peaks is adjusted accordingly, which rigorously proves that Ω dictates the replica band positions. When sufficiently decreasing the phonon frequency, the replica bands disappear as soon as the electron bandwidth becomes the dominant energy scale. Finally, we want to mention that flat band systems (and superconductors) are not compliant to the common understanding of the interacting state in various ways. For example, the mass renormalization becomes negative over extended energy intervals, which is a behavior that previously has only been reported to exist in the strong coupling limit [99]. The neglect of vertex corrections here may seem unjustified because the phonon energy scale is dominant. However, we explicitly calculated an estimate for the magnitude of second-order electron-phonon scattering contributions, and found that these are indeed negligible.

In summary, Paper V shows that in flat band systems, such as TBG, replica bands form at multiples of the phonon frequency and should be observable in tunneling and ARPES measurements. The detection of these signals is potentially challenging because they represent non-coherent excitations, leading to smaller spectral weight and therefore lower intensity in experiment. We analyzed in detail how the replica bands are created and showed that the signals are robust against temperature. When additional non-flat bands are included in the calculation we find a superposition with replica bands, therefore a sufficient energy gap is advantageous to isolate the signals. Even though we considered TBG here as an example, our results are generically applicable to all flat band systems.

5. Additional examples

> *I don't know where I'm going, but I'm on my way*
>
> Carl Sandburg

Here we present additional examples and important aspects in connection to the Eliashberg formalism. In Sections 5.1 and 5.2 we touch upon the topic of high-pressure superconductivity in hydrides, specifically atomic metallic hydrogen (Paper VI) and LaH_{10} (Paper VII). After this we summarize Paper VIII in Section 5.3, introducing an analytic tail scheme (AT-scheme) that reduces the large computational load of Eliashberg theory calculations by significantly decreasing the required number of Matsubara frequencies. We end the current Chapter by discussing phonon renormalization in Eliashberg theory in Section 5.4. Therein, summarizing Paper IX, we examine possible effects that can occur when the first Feynman diagram for the phonon self-energy is self-consistently included in the calculations.

5.1 Atomic hydrogen

Hydrogen rich compounds currently are the record holders for the highest superconducting transition temperatures. The most severe drawback in this family of superconductors is the need of applying extraordinarily high pressures to induce the Cooper pair formation, which so far hinders the broad technological usability. Prominent examples of the hydrides are LaH_{10} ($T_c = 250\,\mathrm{K}$ at $170\,\mathrm{GPa}$) [18, 100, 101], YH_6 ($T_c = 220\,\mathrm{K}$ at $166-237\,\mathrm{GPa}$) [102, 103] and a recently discovered carbanaceous sulfur hydride ($T_c = 287\,\mathrm{K}$ at $267\,\mathrm{GPa}$) [19]. Further, it is widely accepted in the scientific community that electron-phonon interactions are the main mechanism at play in hydrides for mediating these high transition temperatures. In Paper VI we focused on the most basic member of the hydrides, namely atomic hydrogen under large pressures. Wigner and Huntington proposed that sufficient pressure on atomic hydrogen leads to a metallic phase [104] and there has been some experimental support of this hypothesis, for pressures from 250 to $495\,\mathrm{GPa}$ [105–107]. The possibility of high-temperature superconductivity in atomic metallic hydrogen was first mentioned by Ashcroft [108], and has since been studied on the level of McMillan and Allen-Dynes equations [109, 110], and within isotropic Eliashberg theory [111]. Here we study the $I4_1/amd$ phase of atomic hydrogen at

400 GPa pressure using anisotropic Eliashberg theory with *ab initio* input. We examine the anisotropy of the superconducting state and the phonon mode specific contributions to the critical temperature.

In Paper VI the electron-phonon coupling elements $\lambda_{\mathbf{q},\nu}$ (ν: phonon branch), electron energies $\xi_{\mathbf{k},n}$ and phonon frequencies $\omega_{\mathbf{q},\nu}$ were obtained from Density Functional Theory calculations. We use these functions as direct input to our anisotropic Eliashberg formalism. The dynamical electron-phonon couplings, needed for solving the self-consistent Eqs. (2.29) for the mass renormalization $Z_{\mathbf{k},m}$ and gap function $\Delta_{\mathbf{k},m}$, are computed via

$$\lambda_{\mathbf{q},l} = \sum_{\nu} \lambda_{\mathbf{q},\nu} \frac{\omega^2_{\mathbf{q},\nu}}{\omega^2_{\mathbf{q},\nu} + q_l^2}. \tag{5.1}$$

Since the Coulomb pseudopotential is *a priori* not known, we solve the self-consistent equations for a wide range of $\mu^\star$ and T.

The results for the maximum superconducting gap $\Delta = \max_{\mathbf{k}} \Delta_{\mathbf{k},m=0}$ are shown in Fig. 5.1(a). The transition temperatures are indicated as red solid line, and we added the corresponding T_c values found from the Allen-Dynes equation [8] in dashed black. We observe that room-temperature superconductivity in metallic hydrogen is possible for $\mu^\star \lesssim 0.14$, which is not very restrictive with respect to the pair-breaking Coulomb pseudopotential (usually $\mu^\star \sim 0.1$). Further we learn that the modified McMillan equation underestimates T_c by a substantial amount, which we associated with the fact that this equation was originally constructed for weak-coupling superconductors, while here $\lambda = 2.32$.

Another important aspect for the above-mentioned underestimation of T_c is momentum space anisotropy, which is included in our formalism but not in the modified McMillan equation. To disentangle the effects of anisotropy and strong coupling superconductivity, we additionally solved the isotropic Eliashberg equations for the same inputs as above. The results for all three levels of approximation are given in Table 5.1. From this we learn that neglecting the momentum space anisotropy reduces T_c by approximately 5%, while an additional (and severe) decrease of 20% is found for the semi-empirical McMillan formalism.

Table 5.1. *Transition temperatures of atomic metallic hydrogen at 400 GPa, calculated by using the modified McMillan equation, isotropic and anisotropic Eliashberg theory. Table taken from Paper VI.*

	$T_c(\mu^\star = 0.1)$	$T_c(\mu^\star = 0.2)$
Modified McMillan	228 K	183 K
Isotropic Eliashberg	306 K	250 K
Anisotropic Eliashberg	321 K	260 K

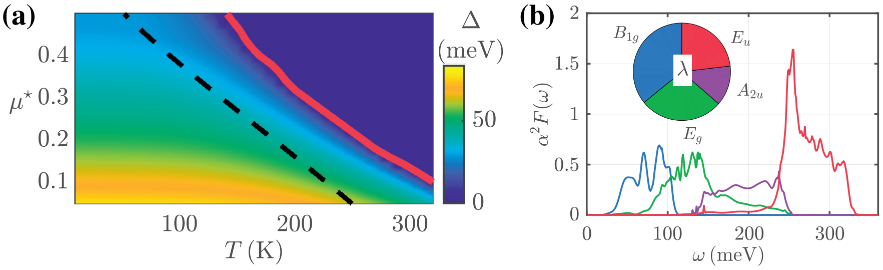

Figure 5.1. (a) Self-consistently calculated maximum superconducting gap as function of temperature and Coulomb pseudopotential. (b) Phonon mode specific contributions to the Eliashberg function. The inset shows how the global coupling strength λ depends on each irreducible representation. The Figure was reconstructed from Paper VI.

The theory employed in Paper VI allowed us to study in detail how different phonon modes influence the superconducting properties of the system. More specifically, there are four irreducible phonon mode representations in metallic atomic hydrogen, namely B_{1g} (one mode), E_g (two modes), A_{2u} (one mode) and E_u (two modes). In Fig. 5.1(b) we show the mode resolved contributions to the Eliashberg function, which is given by

$$\alpha^2F(\omega) = \frac{1}{2\pi N_0}\sum_{\mathbf{q},\nu}\delta(\omega-\omega_{\mathbf{q},\nu})\frac{\gamma_{\mathbf{q},\nu}}{\omega_{\mathbf{q},\nu}}. \tag{5.2}$$

In Eq. (5.2), $\gamma_{\mathbf{q},\nu}$ describes the quasiparticle lifetimes, which are obtained from our *ab initio* calculations. By choosing the branch indices of the lifetimes and frequencies in Eq. (5.2) according to the specific irreducible representation we are interested in, $\alpha^2F(\omega)$ can similarly be associated to the respective phonon modes. From Fig. 5.1(b) it is directly apparent that all modes occupy only confined frequency regions that partially overlap.

Using these results for the Eliashberg function allows us to estimate phonon mode dependent electron-phonon couplings by using the relation

$$\lambda = 2\int_0^\infty \frac{\alpha^2F(\omega)}{\omega}\mathrm{d}\omega. \tag{5.3}$$

The results are shown as inset in Fig. 5.1(b). The largest contribution to the global λ has its origin in the B_{1g} mode, while the smallest part stems from A_{2u} branches. However, it turns out that it is in fact the E_u representation (i.e. not B_{1g}) that has the largest impact on the superconducting transition temperature. We performed an additional set of Eliashberg calculations, where we selectively left out one particular irreducible representation at a time, and report the resulting T_c's in Table 5.2. For both values of $\mu^\star$ considered, by far the largest decrease in T_c is found when neglecting the E_u modes. In contrast, the

Table 5.2. *Reduction in the transition temperatures of atomic metallic hydrogen at 400 GPa due to specific irreducible representations.*

	$T_c(\mu^\star = 0.1)$	$T_c(\mu^\star = 0.2)$
Full calculation	321 K	260 K
without B_{1g}	283 K	213 K
without E_g	240 K	180 K
without A_{2u}	264 K	210 K
without E_u	192 K	154 K

smallest changes in critical temperature are observed for B_{1g}, which explicitly proves that a large coupling strength alone does not guarantee a severe impact on the superconducting properties.

The above insights into the importance of the different phonon modes are further backed up by additional calculations that we performed at a pressure of 600 GPa. Compared to the case of 400 GPa we obtain slightly larger critical temperatures, even though the global coupling strength is decreased to $\lambda = 2.09$. This counterintuitive observation stems from a growing contribution due to the E_u representation, and is therefore compatible with the above interpretation.

In this Section we discussed results from Paper VI, where we studied metallic atomic hydrogen at 400 and 600 GPa pressure, using anisotropic Eliashberg theory with *ab initio* input. For reasonable values of the Coulomb pseudopotential we find room temperature superconductivity with rather small anisotropy of the superconducting gap function. By examining the influence of specific phonon modes on properties of the superconducting state we found that the most significant contributions stem from the E_u irreducible representation, despite the fact that the respective coupling is subdominant.

5.2 A new trigonal phase in LaH_{10}

As mentioned in the previous Section 5.1, LaH_{10} shows one of the highest critical temperatures observed so far, reaching up to $T_c = 250$ K in the pressure regime $137 - 218$ GPa [18, 100, 112]. From crystal structure searches it was initially thought that LaH_{10} has a face-centered cubic lattice structure $Fm\bar{3}m$ above 210 GPa, and that this phase becomes dynamically unstable at low pressures [100]. However, later studies revealed that the cubic structure is stabilized in the range $137 - 218$ GPa upon inclusion of quantum corrections, and that this structural phase most likely corresponds to the measured samples exhibiting such high T_c [113]. When increasing the pressure above 400 GPa, a structural phase transition to a hexagonal $P6_3/mmc$ symmetry was predicted [114]. This high-pressure regime, however, has not yet been explored extensively.

In Paper VII, by performing more extensive cyrstal structure searches, we identify a new trigonal structural phase $R\bar{3}m$, which we find as ground state for pressures between approximately 250 GPa and 425 GPa. In our work we considered mainly the interval 300 – 500 GPa, as the low-pressure region has already been studied in great detail. By using one to four formula units of LaH_{10} in the unit cell, we identified several of the already known structures, most importantly the cubic $Fm\bar{3}m$, hexagonal $P6_3/mmc$ and the new trigonal $R\bar{3}m$ phase. This new structure differs from the already known trigonal configuration in that it consists of three, instead of one formula unit of LaH_{10} in the unit cell [100, 113].

The newly discovered structural phase is characterized by each lanthanum atom being surrounded by cages consisting of 32 hydrogen atoms. These are linked to six neighboring cages via 8 hydrogen atom cuboids, while each 8-H hexagonal face is shared by neighboring 32-H atom cages. It further deserves mentioning that we find an unusually small cell angle of $\alpha \sim 24.56°$, compared to the earlier predicted trigonal structure with $\alpha \sim 60°$. In comparison to the low pressure cubic phase, the hydrogen cages consist of quadrilaterals and hexagons, instead of squares and regular hexagons. We find this new trigonal phase to be stable up to pressures of 425 GPa, where a phase transition to the earlier predicted hexagonal phase occurs. This observation can be made from Fig. 5.2(a), where we show the enthalpy difference of the new trigonal (red), hexagonal (blue) and cubic phase (black), all with respect to the cubic structure. As directly apparent, at the low end of the considered pressure spectrum the cubic and trigonal structures are nearly indistinguishable.

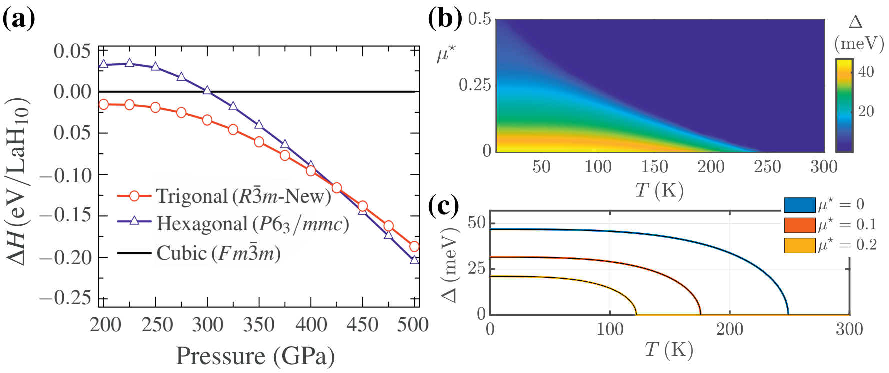

Figure 5.2. (a) Enthalpy difference of each structural phase of LaH_{10} as compared to the cubic $Fm\bar{3}m$ structure. (b) Self-consistently calculated maximum superconducting gap as function of temperature and Coulomb pseudopotential for the new trigonal phase at 350 GPa. (c) Temperature dependence of the superconducting gap for three values of $\mu^\star$, see legend. The thickness of each curve represents the degree of anisotropy in the order parameter. Figure reconstructed from Paper VII.

The aforementioned transition from trigonal to hexagonal is found at 425 GPa, where the latter starts showing a bigger enthalpy difference.

We describe the superconducting phase of trigonal LaH_{10} at 350 GPa by solving Eqs. (2.29) for various temperatures and values of the Coulomb pseudopotential. Here, the electron energies, electron-phonon couplings and phonon frequencies are taken from *ab initio* calculations. The self-consistent results for the maximum superconducting gap as function of T and $\mu^\star$ are shown in Fig. 5.2(b). We observe the usual behavior of decreasing Δ with increasing $\mu^\star$ and T. For three realistic values of the pseudopotential, we show $\Delta(T)$ in Fig. 5.2(c), where the gap anisotropy is represented by the thickness of each line. As each curve is very thin, we conclude that trigonal LaH_{10} exhibits a very isotropic superconducting state, in accordance to most hydrogen-rich high-temperature superconductors.

Table 5.3. *Critical temperature, maximum gap amplitude and ratio Δ/k_BT_c in trigonal LaH_{10} for three representative values of $\mu^\star$.*

$\mu^\star$	T_c (K)	$\Delta(T=0)$ (meV)	Δ/k_BT_c
0	248.7	46.9	2.19
0.1	175.5	31.6	2.09
0.2	122.0	21.1	2.01

In Table 5.3 we show the numeric values for critical temperature T_c, zero-temperature gap magnitude and the ratio Δ/k_BT_c, each for $\mu^\star \in \{0, 0.1, 0.2\}$. As expected, for each value of the Coulomb pseudopotential Δ/k_BT_c is significantly larger that the BCS results of 1.76, indicating strong-coupling superconductivity. Further we report a significant reduction of T_c when compared to the face-centered cubic phase, where a global coupling strength of $\lambda = 2.2$ leads to $T_c \simeq 250$ K [100]. In our newly discovered trigonal phase the coupling strength is reduced to $\lambda = 1.6$, which results in a smaller critical temperature of approximately 175 K at $\mu^\star = 0.1$.

To summarize, in this Section and in Paper VII we presented a new trigonal phase of LaH_{10} that represents the most likely prevailing structure at pressures $250-425$ GPa. At lower pressures we find the well-established face-centered cubic phase with $T_c = 250$ K, while the new trigonal compound shows a reduced critical temperature of about 175 K. At 425 GPa we find a phase transition to a hexagonal structure, that was predicted earlier. Therefore our findings provide a better understanding of the high-pressure regime in LaH_{10} and can be experimentally probed by studying details of the superconducting state.

5.3 Reducing the computational costs

There is no doubt that the numerical solution of coupled Eliashberg equations is generally a difficult task. This stems from the fact that potentially large momentum and frequency grids are involved, and additionally one needs to use a self-consistency loop with a possibly high number of iterations. To complicate the challenge further, Matsubara frequencies are proportional to temperature, which means that the required number of frequencies in a fixed energy interval increases as T decreases. In practical applications it is often not enough to solve the coupled equations only for a single set of parameters, as one might be interested in the evolution of certain quantities with e.g. doping or temperature. For these reasons it is always of great interest to come up with simplified or more efficient solutions for these numerical challenges.

In Paper VIII we introduced an AT-scheme to significantly reduce the computational costs of solving Eliashberg equations. The motivation for this work came from Paper I, where we had to apply a non-interacting state approximation for high-frequency tails of functions in Matsubara space, so as to make the chemical potential shift in Eq. (3.2) numerically stable. Here we apply a similar idea to the entire Eliashberg formalism to reduce the number of Matsubara frequencies needed for well converged results. The method discussed below is applicable to calculations involving summations over infinitely many Matsubara frequencies, where the functional form of the interaction is either known or can be accurately determined by numerical fitting. For introducing the concept, we focus here on the anisotropic full bandwidth formalism, see Eqs. (2.13).

To introduce our approach, consider a function $F_m = \sum_{m'} g_{m-m'} f_{m'}$ with f_m depending on fermion Matsubara frequencies ω_m. The generally accepted procedure for evaluating this sum over all integers m' is to set a hard numerical cutoff $\pm\mathscr{M}$, and neglect all contributions to F_m from frequencies $|m'| > \mathscr{M}$ [8,24]. However, here we assume that the functional form of $g_{m-m'}$ is known, and that $f_m = f_m^{(0)}$ is a good approximation for $|m| > \mathscr{M}$, with $f_m^{(0)}$ also known. Below this will be referred to as the non-interacting state approximation. In this case we can write $F_m = \sum_{|m'|\leq\mathscr{M}} g_{m-m'} f_m + \sum_{|m'|>\mathscr{M}} g_{m-m'} f_m^{(0)}$. The second sum can be recast by the simple observation that $\sum_{|m'|>\mathscr{M}}(\cdot) = \sum_m(\cdot) - \sum_{|m'|\leq\mathscr{M}}(\cdot)$. It follows that $F_m \simeq F_m^{(\mathscr{A})} = F_m^{(I)} + F_m^{(N)} - F_m^{(N_\mathscr{M})}$, where we use labels (I) for the interacting state, (N) for non-interacting state, and $(N_\mathscr{M})$ for non-interacting state inside the numerically accessible boundaries. Here, $F_m^{(\mathscr{A})}$ is our approximation to F_m that accounts for the infinite tails in Matusbara space. We note that, in the case of Eliashberg equations, $F_m^{(N)}$ and $F_m^{(N_\mathscr{M})}$ can be precomputed, i.e. they do not have to be updated in the self-consistent cycle. The summation in $F_m^{(N)}$ runs over all integers, and can be evaluated analytically.

More specifically for Eliashberg theory, compare Eqs. (2.13), the non-interacting state approximation for functions $Z_{\mathbf{k},m}$, $\chi_{\mathbf{k},m}$ and $\phi_{\mathbf{k},m}$ reads

$$\exists\mathscr{M} >> 1 \in \mathbb{N}:\ Z_{\mathbf{k},|m|>\mathscr{M}} = 1,\ \chi_{\mathbf{k},|m|>\mathscr{M}} = \phi_{\mathbf{k},|m|>\mathscr{M}} = 0\ \forall\mathbf{k}. \tag{5.4}$$

On the basis of Eq. (5.4) the mass renormalization and chemical potential shift within our AT-scheme are calculated from the above-mentioned three terms, while $\phi^{(\mathscr{A})}_{\mathbf{k},m} = \phi^{(I)}_{\mathbf{k},m}$ remains unchanged. Likewise we apply the non-interacting state approximation to the Matsubara dependent part of our analytic continuation procedure, which leads to real-frequency dependent functions $f^{(\mathscr{A})}_{\mathbf{k},\omega}$ in contrast to the usual $f_{\mathbf{k},\omega}$ ($f = Z,\ \chi,\ \phi$). To evaluate the efficiency of our method we start from a very large number of Matsubara frequencies (12000), at which we calculate reference results f_{ref} and $f^{(\mathscr{A})}_{\text{ref}}$, i.e. for the conventional approach and our AT-scheme. We then gradually decrease the number of Matsubara frequencies and compare the results at each step to the reference functions, using the error measures

$$\varepsilon_A = \log_{10}\Big(\int |A - A_{\text{ref}}| \mathrm{d}\omega\Big), \tag{5.5a}$$

$$\varepsilon_f = \log_{10}(\langle |f_{\text{ref}} - f_{\mathbf{k},\omega}|\rangle_{\mathbf{k},\omega}), \quad f = Z, \chi, \phi, \tag{5.5b}$$

where A is the spectral function, and likewise for each $f^{(\mathscr{A})}$.

Here we discuss results obtained at $T = 10\,\text{K}$ for FeSe/STO (see Chapter 3), with the parameters used in Ref. [58] and Paper I. Using a hard cutoff for the tails in Matsubara space in this system requires approximately 1500 frequencies for reliable results, so using 12000 frequencies for our reference functions leads to extremely well converged outcomes. In Fig. 5.3(a) we show the ARPES spectrum of FeSe/STO at the M point of the BZ in cyan, where both curves (vertically shifted) have been calculated with the standard procedure of neglecting the tails in Matsubara space. The dashed red (dotted purple) results are obtained by calculating the spectral function with (without) the AT-scheme for 100 frequencies. The deviation from the reference graph is small in both cases, but larger without AT corrections. A more rigorous error estimate is shown in the inset, where we plot the logarithmic errors ε_A and $\varepsilon^{(\mathscr{A})}_A$, compare Eq. (5.5a). As directly apparent, we spare about a factor of five in the number of Matsubara frequencies required to reach a given precision when the AT-scheme is used. Equivalently, for a given cutoff $\mathscr{M}$ we find $\varepsilon^{(\mathscr{A})}_A$ about two orders of magnitude smaller than ε_A.

In Fig. 5.3(b) we show logarithmic errors of each individual function Z, χ and ϕ after the analytic continuation procedure. As a reminder, we use the AT-scheme in the self-consistent Matsubara space calculation and for those terms of the analytic continuation that depend on Matsubara frequencies. From this graph we learn that the errors $\varepsilon^{(\mathscr{A})}_f$ are significantly smaller than their respective counterparts ε_f. Here the AT-scheme allows us to spare approximately a factor of eight in the number of frequencies.

To conclude, in Paper VIII we introduced a method to reduce the required number of Matsubara frequencies in anisotropic Eliashberg equations by approximately 80%. We additionally tested the same idea on isotropic Eliashberg theory, where such savings are even up to 90%. Further it is important to

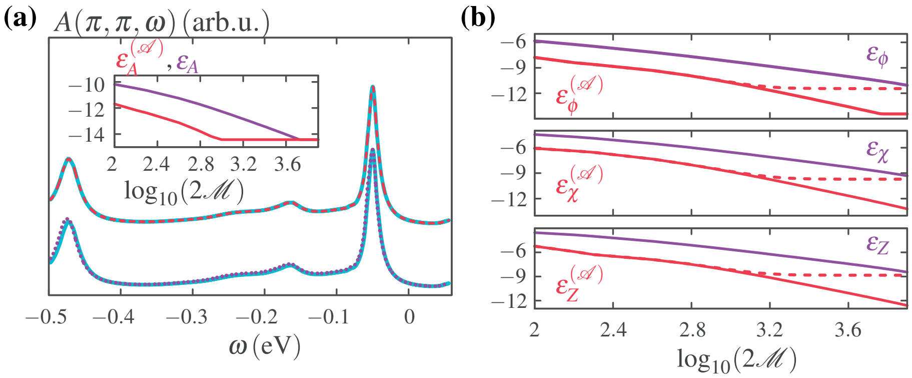

Figure 5.3. (a) Spectral function of FeSe/STO at the M point (cyan). Red dashed and purple dotted curves are found with and without AT-scheme. The inset shows the logarithmic errors in both cases as function of cutoff $\mathscr{M}$. (b) Logarithmic errors for ϕ, χ and Z as function of cutoff $\mathscr{M}$. Purple and red curves show our results without and with AT corrections, respectively. The red dashed lines are deviations of AT-scheme results from non-AT-scheme reference functions. Figure taken from Paper VIII.

note that the here introduced AT-scheme is compatible with using Fast Fourier transforms to evaluate momentum and frequency sums (which were used in all calculations of Paper VIII). There are cases where the functional form of the interaction is not known, for example in Fluctuation Exchange calculations where the kernel is iteratively updated. Even though our method would in principle be applicable by fitting the interaction to a known functional form, such as a Lorentzian, other approaches to include the tails in Matsubara space might be more suitable [115–117].

5.4 Phonon renormalization

In this last Section of the current Chapter we discuss the effects of phonon renormalization on the superconducting state in Holstein-like model systems. We have seen in Chapter 2 how the Eliashberg equations are theoretically derived, but in this derivation we neglected for simplicity the backreaction of electrons onto the phonon spectrum, as it is common practice. Equivalently, this means that we omitted all Feynman diagrams for the phonon self-energy $\Pi_{\mathbf{q},l}$, and hence set $\Pi_{\mathbf{q},l} = 0$. In Paper IX we provided an overview of possible effects that can occur when we go beyond such an assumption, i.e. when both first order Feynman diagrams of Fig. 5.4 are taken into account self-consistently.

Before our work such investigation has not been done in a systematic way, but rather with the primary goal of testing the validity of Eliashberg theory [17, 118, 119]. In these works results from the Eliashberg formalism are benchmarked against other approaches, such as Quantum Monte Carlo

(QMC) [120, 121] or Dynamical Mean-Field theories [122]. From these studies the generally accepted picture has emerged that there exists a maximally allowed electron-phonon coupling strength for any given system, which marks the border of applicability of Eliashberg theory. However, it is noteworthy that the benchmark methods often have their disadvantages and inaccuracies as well, such as e.g. small lattice sizes in QMC. Additionally, the Eliashberg calculations were often not performed in the superconducting state but rather extrapolated from the normal state [120, 122]. It needs to be stressed that here we are only interested in the results from the Migdal-Eliashberg formalism and leave the comparison to other theories for future works.

By far the most commonly studied system in this context is the 2D Holstein model [123–125]. To make comparison to other works easier we followed a similar path in Paper IX, describing the electron energies within a next-nearest neighbor tight-binding model as

$$\xi_{\mathbf{k}} = -2t^{(1)}[\cos(k_x)+\cos(k_y)] - 4t^{(2)}\cos(k_x)\cos(k_y) - \mu, \tag{5.6}$$

where $t^{(1)}$ is the nearest, and $t^{(2)}$ the next-nearest neighbor hopping energy. In most of what follows, we will focus primarily on this two dimensional system. The Eliashberg formalism employed here differs from Eqs. (2.13) only in one key aspect, i.e. that we now consider a finite phonon self-energy. This means that the electron-phonon coupling $V_{\mathbf{q},l} = -|g_{\mathbf{q}}|^2 D_{\mathbf{q},l}$ is iteratively updated on the same footing as $Z_{\mathbf{k},m}$, $\chi_{\mathbf{k},m}$ and $\phi_{\mathbf{k},m}$. To do so we calculate the phonon propagator via a Dyson equation,

$$D^{-1}_{\mathbf{q},l} = \big[D^{(0)}_{\mathbf{q},l}\big]^{-1} - \Pi_{\mathbf{q},l}, \tag{5.7}$$

with bare Green's function $D^{(0)}_{\mathbf{q},l} = -2\Omega_0/(\Omega_0^2 + q_l^2)$, and evaluate the phonon self-energy via Fig. 5.4(b) as

$$\Pi_{\mathbf{q},l} = T|g_{\mathbf{q}}|^2 \sum_{\mathbf{k},m} \mathrm{Tr}\big[\hat{\rho}_3 \hat{G}_{\mathbf{k},m} \hat{\rho}_3 \hat{G}_{\mathbf{k}+\mathbf{q},m+l}\big]. \tag{5.8}$$

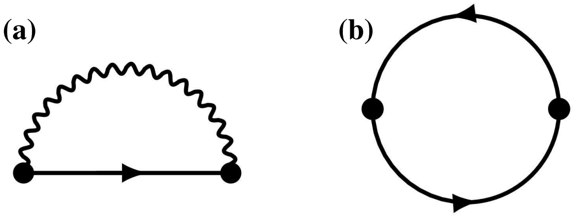

Figure 5.4. Feynman diagrams for the electron (a) and phonon (b) self-energy. Figure taken from Paper IX.

The zero-frequency renormalized coupling strength and phonon frequencies can be calculated by

$$\lambda_{\mathbf{q}} = -N_0 |g_{\mathbf{q}}|^2 D_{\mathbf{q},l=0}, \tag{5.9a}$$

$$\Omega_{\mathbf{q}} = \sqrt{\Omega_0^2 + 2\Omega_0 \Pi_{\mathbf{q},l=0}}, \tag{5.9b}$$

from which we can define a measure for the global electron-phonon coupling strength as $\lambda = \langle\langle \lambda_{\mathbf{k}-\mathbf{k}'} \rangle_{\mathbf{k}\in\mathrm{FS}} \rangle_{\mathbf{k}'\in\mathrm{FS}}$.

In Fig. 5.5 we show our results for the 2D system, where we used the hopping energies $t^{(1)} = W/8$ and $t^{(2)} = t^{(1)}/4$ for the electron dispersion, with electron bandwidth $W = 1.5\,\mathrm{eV}$, and three different chemical potentials $\mu = 62.5\,\mathrm{meV}$ [orange, (1)], $-437.5\,\mathrm{meV}$ [green, (2)] and $-887.5\,\mathrm{meV}$ [purple, (3)]. The energies and FSs are shown in panels (a) and (b). For solving the Eliashberg equations we choose isotropic scattering matrix elements $g_{\mathbf{q}} = g_0$, and vary the initial coupling strength λ_0 for different bare phonon frequencies Ω_0. Due to the fact that we systematically change λ_0 (and not g_0), the three $\xi_{\mathbf{k}}$ differ to good approximation only in nesting properties and the size of their FS, since changes in the density of states N_0 are compensated for by the relation $\lambda_0 = 2N_0 g_0^2/\Omega_0$.

To get a general idea of the possible effects that can occur due to including phonon renormalization into our Eliashberg framework, we show results for the coupling strength λ (i-iii), minimum phonon frequency (iv-vi) and superconducting gap $\Delta = \max_{\mathbf{k}} \Delta_{\mathbf{k},m=0}$ (vii-ix), each as function of input coupling λ_0, in Fig. 5.5(c) with color codes as in panel (a).

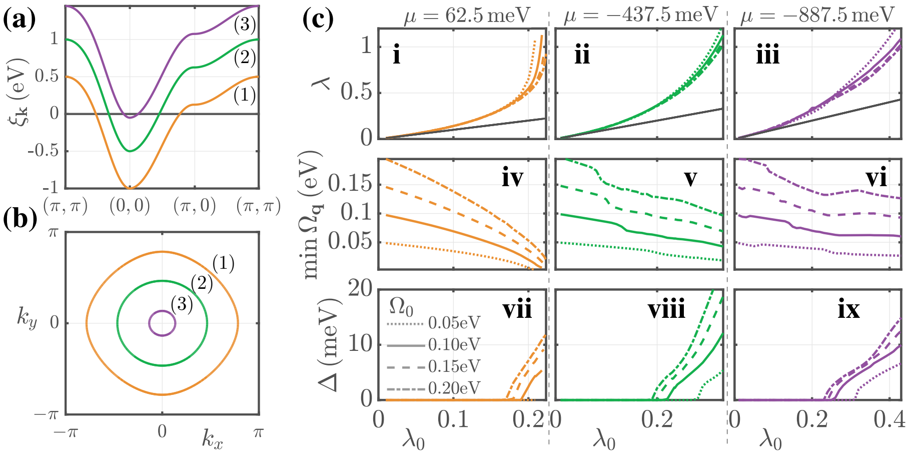

Figure 5.5. (a) Electron dispersion along high-symmetry lines for three different chemical potential shifts. (b) Fermi surface corresponding to panel (a). (c) Equivalent color codes as in panels (a) and (b). The first, second and third rows show the renormalized coupling strength, minimum phonon frequency and superconducting gap magnitude, respectively. Figure taken from Paper IX.

The first important thing to notice is the divergence of λ at a certain coupling strength $\lambda_0^\star$, which coincides with a decrease in the minimal phonon frequency (phonon softening). This effect corresponds to a lattice instability where our formalism is no longer applicable, and is in agreement to previous works [119, 120, 122]. When the renormalized coupling strength is sufficiently large but not yet divergent, we find the onset of superconductivity in panels (vii-ix) and a growing Δ as λ increases further. Each panel in Fig. 5.5(c) contains results for different frequencies Ω_0. By comparison we learn that λ and $\lambda_0^\star$ are rather insensitive to changes in Ω_0, while the onset of superconductivity occurs at smaller input couplings for larger input frequencies.

When comparing the results for our three electron dispersions we see that a decrease in FS size leads to less pronounced phonon softening at similar values of λ_0. Equivalently, $\lambda_0^\star$ increases as we go from energies (1) to (3). The reason for this behavior are the nesting conditions in each of the $\xi_{\mathbf{k}}$. From Fig. 5.5(b) it is apparent that FS segments of dispersion (1) can be connected more coherently than is the case for (2), and even more so in comparison to the most shallow energy band (3). A rigorous confirmation of this explanation is found from the momentum dependent phonon frequencies, where we find the softest frequencies at the approximate nesting wave vector. Overall this is not surprising since the phonon self-energy can be expressed as $\Pi_{\mathbf{q},l} = -g_{\mathbf{q}}^2 X_{\mathbf{q},l}^{(0)}$, with $X_{\mathbf{q},l}^{(0)}$ the charge susceptibility. Due to the fact that $X_{\mathbf{q},l}^{(0)}$ peaks at the FS nesting wave vector, which is a well documented behavior from purely electronic theories of superconductivity, the same properties apply to the phonon self-energy. From Eq. (5.9b) it then becomes clear that better nesting leads to smaller phonon frequencies.

Next we want to address the scaling of the renormalized coupling strength as function of λ_0. From Eq. (5.9a) and the aforementioned relation $\Pi_{\mathbf{q},l} =$

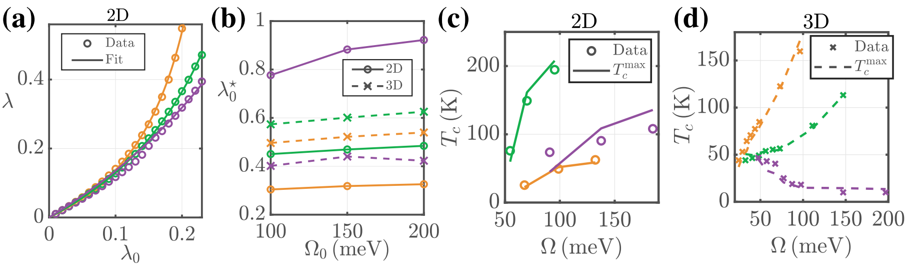

Figure 5.6. (a) Renormalized coupling strength for $T = 20\,\mathrm{K}$ and $\Omega_0 = 100\,\mathrm{meV}$ as function of input coupling λ_0 for the 2D systems, with color code corresponding to Fig. 5.5(a). (b) Estimate for the maximally allowed input couplings at $T = 20\,\mathrm{K}$ for 2D (solid) and 3D (dashed) systems as function of bare phonon frequency. (c) and (d) show the largest critical temperatures found in 2D and 3D, respectively, as function of renormalized phonon frequency. Figure taken from Paper IX.

$-g^2_{\mathbf{q}}X^{(0)}_{\mathbf{q},l}$ we can write $\lambda = \langle\langle \lambda_0/(1-\lambda_0 X_{\mathbf{q},l=0}/N_0)\rangle_{\mathbf{k}\in\mathrm{FS}}\rangle_{\mathbf{k}'\in\mathrm{FS}}$. Due to this dependence we choose the approximate functional form as

$$\lambda \sim a_\lambda \frac{\lambda_0}{1-b_\lambda\lambda_0}, \tag{5.10}$$

with a_λ and b_λ free parameters, with which we fit our data points in Fig. 5.6(a). As is directly apparent, Eq. (5.10) captures our self-consistent results very accurately for all three electron dispersions. We know that λ diverges as $\lambda_0 \to \lambda_0^\star$, i.e. when the system develops a charge density wave instability. Therefore we can determine the approximate value of $\lambda_0^\star$ by setting the denominator of Eq. (5.10) to zero, which gives $\lambda_0^\star \simeq b_\lambda^{-1}$.

In Paper IX we also examined 3D systems, which we will not go into detail here but only mention some of the results. The corresponding electron energies are similar to the 2D case, i.e. using a next-nearest neighbor tight-binding description with the same bandwidth $W = 1.5\,\mathrm{eV}$ we define three different $\xi_{\mathbf{k}}$ by altering the chemical potential: a very shallow band (purple), one with large electron filling resembling a Fermi gas (orange), and one intermediate case (green). The results for the critical coupling strength $\lambda_0^\star$ for 2D (solid) and 3D (dashed) systems are shown in Fig. 5.6(b).

We find a relatively mild dependence of $\lambda_0^\star$ on the bare phonon frequency, for all systems considered. As mentioned before, in 2D the rather coherent nesting conditions in dispersion (1) lead to comparatively small values for the critical coupling strength. As the nesting becomes less coherent, energies (2) and (3), $\lambda_0^\star$ grows. This observation confirms our interpretation of the renormalized coupling strength in terms of the charge susceptibility, see above. Our findings for 3D (dashed curves) suggest that $\lambda_0^\star$ is rather robust with respect to changes in the electron dispersion, and we therefore conclude that nesting becomes less important in 3D. Results plotted in orange and green follow similar trends as in 2D, i.e. more coherent nesting leads to smaller $\lambda_0^\star$. An exception is the very shallow band (purple), which is due to the special role of the $\mathbf{q} = (0,0,0)$ exchange wave vector. As the absolute value of $\mathbf{q}$ becomes small the angular dependence loses its significance and nesting becomes coherent again, an effect that is well pronounced in 3D but less so in 2D. For this reason we find the smallest values of $\lambda_0^\star$ in 3D for the shallow energy band.

For both, 2D and 3D systems we calculated the maximally possible values of T_c with respect to $\lambda_0 \to \lambda_0^\star$ for various input frequencies Ω_0. In Fig. 5.6(c) and (d) we show the respective outcomes against the renormalized frequency $\Omega = \langle \Omega_{\mathbf{q}} \rangle_{\mathbf{q}\in\mathrm{BZ}}$ as open circles and crosses, respectively, for the three different $\xi_{\mathbf{k}}$ using the same color code as before. To model the observed functional dependence of the critical temperature on Ω, we started by $T_c^{\max} \propto \sqrt{\Omega_0^2 - \Omega^2}$, which was proposed in Ref. [126]. We found that our data in 2D, Fig. 5.6(c), can be fitted accurately in this way but less so our results for 3D systems. Instead, the most precise match to our outcomes, which are the solid and dashed lines in Fig. 5.6(c) and (d), respectively, is obtained via

$$k_B T_c \propto \lambda(\Omega)\sqrt{\Omega_0^2 - \Omega^2} \sim \lambda_0 \frac{\Omega_0^2}{\Omega^2}\sqrt{\Omega_0^2 - \Omega^2}. \tag{5.11}$$

This scaling law for the maximum value of T_c within Eliashberg theory can be interpreted in a straight forward way. First, it is not surprising that the critical temperature scales like the coupling strength, which in turn depends heavily on the details of phonon softening, as we discussed above. Secondly, we find that phonon softening is advantageous for T_c in its own right as seen from the square root in Eq. (5.11). However, this is only a very approximate explanation of our results, as one has to bear in mind that also details of the electron dispersion and the initial coupling strength influence Ω.

Summarizing, in Paper IX we have investigated the effects of phonon renormalization in 2D and 3D Holstein-like systems, using full bandwidth Eliashberg theory, as function of bare electron-phonon coupling strength, initial phonon frequency, nesting conditions and size of the FS. Our results on phonon softening, renormalized coupling strength and superconductivity give a broad overview on the topic. Finally, we have proposed a new scaling law for T_c that is valid for Eliashberg theory of two and three dimensional systems.

Part II:
Vertex-corrected Eliashberg theory

6. Formalism and exploration

Without deviation from the norm,
progress is not possible.

Frank Zappa

Up to this point we focused on what can be called 'standard' Eliashberg theory, i.e. the theoretical description of superconductors motivated from Migdal's approximation. For electron-phonon mediated Cooper pairing we are allowed to neglect vertex corrections to the scattering process, provided that the ratio α of phonon to electron energy scales is significantly smaller than unity [4]. As a side remark, no such theoretical justification of neglecting vertex corrections exists for the case of spin fluctuations [21], but the validity of using only the first electron-boson scattering Feynman diagram in this case is rarely questioned.

As it turns out, many high-temperature superconductors, including the families of Cu- and Fe-based materials, do not qualify for a neglect of vertex corrections, as in these systems $\alpha \sim \mathscr{O}(0.1) - \mathscr{O}(1)$. This is mainly due the common ingredient of very shallow energy bands close to the Fermi surface, combined with comparatively large boson frequencies [15, 127–129]. For this reason we wanted to systematically explore possible effects due to the mentioned vertex corrections to the electron-phonon scattering process. In Section 6.1 we derive an extended set of Eliashberg equations, which served as basis for Paper X, summarized in Section 6.2. The theoretical and numerical results presented here are built upon further in discussions in Chapter 7.

6.1 Extended Eliashberg theory

6.1.1 First and second order Feynman diagrams

We use here a similar recipe as in Section 2.1, where we derive the 'standard' Eliashberg equations. Consider a single optical phonon mode Ω, which is coupled to the electrons via $g_{\mathbf{q}}$. The systems Hamiltonian is then given by

$$H = \sum_{\mathbf{k}} \xi_{\mathbf{k}} \Psi^{\dagger}_{\mathbf{k}} \hat{\rho}_3 \Psi_{\mathbf{k}} + \Omega \sum_{\mathbf{q}} \left(b^{\dagger}_{\mathbf{q}} b_{\mathbf{q}} + \frac{1}{2} \right) + \sum_{\mathbf{k},\mathbf{q}} g_{\mathbf{q}} u_{\mathbf{q}} \Psi^{\dagger}_{\mathbf{k}-\mathbf{q}} \hat{\rho}_3 \Psi_{\mathbf{k}}. \tag{6.1}$$

For simplicity we drop the band index in the electron dispersion $\xi_{\mathbf{k}}$ and return to this aspect in the end of the current section. As before, $b^{\dagger}_{\mathbf{q}}$ ($c^{\dagger}_{\mathbf{k},\sigma}$) and $b_{\mathbf{q}}$

($c_{\mathbf{k},\sigma}$) are the phonon (electron) creation and annihilation operators, respectively. The Nambu spinor is defined as $\Psi^{\dagger}_{\mathbf{k}} = (c^{\dagger}_{\mathbf{k},\uparrow}, c_{-\mathbf{k},\downarrow})$, and $u_{\mathbf{q}} = b^{\dagger}_{\mathbf{q}} + b_{-\mathbf{q}}$ is the ion displacement.

The electron Green's function $\hat{G}_k$ obeys the Dyson equation

$$\hat{G}_k = \hat{G}^{(0)}_k + \hat{G}^{(0)}_k \hat{\Sigma}_k \hat{G}_k, \tag{6.2}$$

where we introduce the four-momentum notation $k = (\mathbf{k}, m)$. The ansatz for the electron self-energy $\hat{\Sigma}_k$ reads

$$\hat{\Sigma}_k = i\omega_k(1 - Z_k)\hat{\rho}_0 + \chi_k\hat{\rho}_3 + \phi_k\hat{\rho}_1. \tag{6.3}$$

Similar to earlier Chapters, Z_k is the electron mass renormalization, χ_k a chemical potential shift and ϕ_k the superconductivity order parameter. By using Eqs. (6.2) and (6.3), together with the non-interacting electron Green's function $[\hat{G}^{(0)}_k]^{-1} = i\omega_k\hat{\rho}_0 - \xi_k\hat{\rho}_3$, we obtain

$$\hat{G}_k = \frac{i\omega_k Z_k}{\Theta_k}\hat{\rho}_0 + \frac{\xi_k + \chi_k}{\Theta_k}\hat{\rho}_3 + \frac{\phi_k}{\Theta_k}\hat{\rho}_1, \tag{6.4}$$

with $\Theta_k = [i\omega_k Z_k]^2 - [\xi_k + \chi_k]^2 - \phi_k^2$.

The mathematical expressions in the remainder of this section are rather lengthy, which is why the shorthand notation

$$\gamma^{(Z)}_k = \frac{\omega_k Z_k}{\Theta_k},\ \gamma^{(\chi)}_k = \frac{\xi_k + \chi_k}{\Theta_k},\ \gamma^{(\phi)}_k = \frac{\phi_k}{\Theta_k} \tag{6.5}$$

comes in handy. With these definitions we can write Eq. (6.4) as

$$\hat{G}_k = i\gamma^{(Z)}_k\hat{\rho}_0 + \gamma^{(\chi)}_k\hat{\rho}_3 + \gamma^{(\phi)}_k\hat{\rho}_1. \tag{6.6}$$

Up to this point the derivation shown here is essentially equivalent to the calculations in Section 2.1. However, it is instructive to have the necessary equations available in the current section, as they are required for the following steps below.

For deriving self-consistent equations we first need to evaluate the electron self-energy by considering the Feynman diagram series for electron-phonon scattering. As first shown by Migdal, $\hat{\Sigma}$ can be written as infinite series of diagrams, where the expansion parameter scales like $\alpha = \Omega/\varepsilon_F$ [4]. In a large number of superconductors one finds $\alpha \gtrsim \mathscr{O}(0.1)$, i.e. corrections to the first order diagram cannot be expected to be negligible. For this reason we include here the first and second order contributions, which are depicted in Fig. 6.1. The straight lines represent the electron Green's functions $\hat{G}_k$, the wavy lines show phonon propagators D_q, and each vertex (black spheres) is associated with a factor $g_q\hat{\rho}_3$ or $g^*_q\hat{\rho}_3$, depending on whether a given vertex opens or closes a loop. Let us write the two contributions to the electron self-energy as

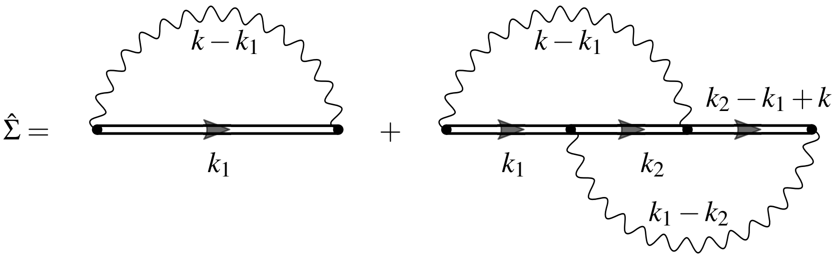

Figure 6.1. First (left) and second (right) order Feynman diagrams for electron-phonon scattering, constituting the building blocks for the electron self-energy.

$\hat{\Sigma}_k = \hat{\Sigma}_k^{(1)} + \hat{\Sigma}_k^{(2)}$. From Section 2.1 we already know the functional form of the first order contributions, namely

$$\hat{\Sigma}_k^{(1)} = T \sum_{k_1} |g_{k-k_1}|^2 D_{k-k_1} \hat{\rho}_3 \hat{G}_{k_1} \hat{\rho}_3. \tag{6.7}$$

It is worthwhile evaluating $\hat{\Sigma}_k^{(2)}$ step by step, see the diagram on the right in Fig. 6.1. Going from left to right, the first vertex opens a loop by producing a factor $g_{k-k_1}\hat{\rho}_3$. The associated electron and phonon propagators are $\hat{G}_{k_1}$ and D_{k-k_1}. Note, that k_1 is an internal index, while $k - k_1$ is dictated by momentum and energy conservation. The following vertex, $g_{k_1-k_2}\hat{\rho}_3$, opens a loop of $\hat{G}_{k_2}$ and $D_{k_1-k_2}$, analogously to the previous case. Hereafter, the first loop closes, producing $g^*_{k-k_1}\hat{\rho}_3$. The index k_3 of the third electron Green's function can be determined by realizing that, together with the second phonon propagator index, $k_3 + (k_1 - k_2)$ must equal k, therefore $k_3 = k_2 - k_1 + k$. This is again a consequence of momentum and energy conservation. Finally, the last vertex contributes a factor $g^*_{k_1-k_2}\hat{\rho}_3$, so that all together we have

$$\hat{\Sigma}_k^{(2)} = T^2 \sum_{k_1} \sum_{k_2} D_{k-k_1} D_{k_1-k_2} |g_{k-k_1}|^2 |g_{k_1-k_2}|^2 \hat{\rho}_3 \hat{G}_{k_1} \hat{\rho}_3 \hat{G}_{k_2} \hat{\rho}_3 \hat{G}_{k_2-k_1+k} \hat{\rho}_3, \tag{6.8}$$

where we have to sum over the two independent internal indices k_1 and k_2. By expressing the product of electron-phonon scattering elements with the phonon propagator as coupling $V_q = |g_q|^2 D_q$, we get

$$\hat{\Sigma}_k = T \sum_{k_1} V_{k-k_1} \hat{\rho}_3 \hat{G}_{k_1} \hat{\rho}_3 + T^2 \sum_{k_1,k_2} V_{k-k_1} V_{k_1-k_2} \hat{\rho}_3 \hat{G}_{k_1} \hat{\rho}_3 \hat{G}_{k_2} \hat{\rho}_3 \hat{G}_{k_2-k_1+k} \hat{\rho}_3. \tag{6.9}$$

The above self-energy can be used in the single-band picture or for multiple electron bands, provided that the electron-phonon coupling can be considered band-independent. In this case we simply need to sum over the energy band index in the definition[1] of each $\gamma_k^{(\cdot)}$, compare Eq. (6.5). On the other hand, using explicitly electron band dependent interactions is beyond the scope of the current work. From here on we employ the bare phonon propagator, i.e. $D_{\mathbf{q},l} = D^{(0)}_{\mathbf{q},l}$. Further, we assume that the electron-phonon scattering $g_\mathbf{q} = g_0$ is momentum-independent. With the Eliashberg function $\alpha^2F(\omega) = N_0 g_0^2 \delta(\omega - \Omega)$ we can express the electron-phonon coupling as

$$V_{\mathbf{q},l} = D_{\mathbf{q},l}|g_\mathbf{q}|^2 = D^{(0)}_l g_0^2 = \int_0^\infty \frac{\mathrm{d}\omega}{N_0}\alpha^2F(\omega)\frac{2\omega}{q_l^2+\omega^2} \equiv V_l. \qquad (6.10)$$

It is important to note that the interaction in Eq. (6.10) can never lead to an anisotropic superconducting gap when used in BCS or 'standard' Eliashberg theory. As we see in later Sections, this statement no longer holds for vertex-corrected Eliashberg theory. In the following we derive the self-consistent Eliashberg equations from Eq. (6.9) and show various possible simplifications.

6.1.2 Levels of approximation

Here we explore different levels of sophistication at which the vertex-corrected Eliashberg equations can be tackled. For each approximation shown below, the recipe for deriving the final self-consistent equations is equivalent: With the electron self-energy given by Eq. (6.3), and whatever approximation we derive from Eq. (6.9) we have the tools to extract each function individually. To do so we need to multiply $\hat{\Sigma}$ by a Pauli matrix of our choosing ($\hat{\rho}_0$ for Z, $\hat{\rho}_3$ for χ, $\hat{\rho}_1$ for ϕ) and trace the result. For an overview of the different approximations introduced below, we show characteristic scattering processes due to the second order Feynman diagram in Fig. 6.2, where the Fermi surface is sketched as blue circle, and black solid lines correspond to virtual processes between scattering events.

General case

The most straight-forward approach to the self-energy in Eq. (6.9) is to not introduce any approximations whatsoever. In this case the electron degrees of freedom are not confined in any way, and contributions throughout the whole electron bandwidth are taken into account. An example for a possible scattering process due to the second order Feynman diagram is shown on the left side of Fig. 6.2. Here, the positions of all electronic states are unrestricted, hence no further assumptions on the smallness of $\alpha < 1$ are required.

---

[1] For a multiband electron dispersion $\xi_{k,n}$, with n the energy band index, we get $\Theta_{k,n} = [i\omega_k Z_k]^2 - [\xi_{k,n} + \chi_k]^2 - \phi_k^2$, leading to the definitions $\gamma_k^{(Z)} = \sum_n \omega_k Z_k/\Theta_{k,n}$, $\gamma_k^{(\chi)} = \sum_n(\xi_{k,n} + \chi_k)/\Theta_{k,n}$ and $\gamma_k^{(\phi)} = \sum_n \phi_k/\Theta_{k,n}$.

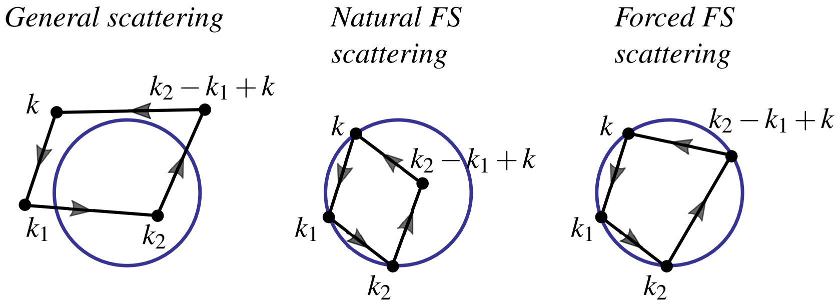

Figure 6.2. Different levels of approximation for the second order electron-phonon scattering processes.

Directly using Eq. (6.9) for the electron self-energy yields the vertex-corrected Eliashberg equations

$$Z_k = 1 - \frac{T}{\omega_k} \sum_{k_1} V_{k-k_1} \Big(\gamma^{(Z)}_{k_1} + T \sum_{k_2} V_{k_1-k_2} \vec{\gamma}^T_{k_2} P^{(Z)}_{k_1} \vec{\gamma}_{k_2-k_1+k} \Big), \tag{6.11a}$$

$$\chi_k = T \sum_{k_1} V_{k-k_1} \Big(\gamma^{(\chi)}_{k_1} + T \sum_{k_2} V_{k_1-k_2} \vec{\gamma}^T_{k_2} P^{(\chi)}_{k_1} \vec{\gamma}_{k_2-k_1+k} \Big), \tag{6.11b}$$

$$\phi_k = -T \sum_{k_1} V_{k-k_1} \Big(\gamma^{(\phi)}_{k_1} + T \sum_{k_2} V_{k_1-k_2} \vec{\gamma}^T_{k_2} P^{(\phi)}_{k_1} \vec{\gamma}_{k_2-k_1+k} \Big), \tag{6.11c}$$

where we define the three-component pseudovectors $\vec{\gamma}^T_k = (\gamma^{(Z)}_k, \gamma^{(\chi)}_k, \gamma^{(\phi)}_k)$. Further, the matrices in Eqs. (6.11) are given by

$$P^{(Z)}_k = \begin{pmatrix} -\gamma^{(Z)}_k & \gamma^{(\chi)}_k & \gamma^{(\phi)}_k \\ \gamma^{(\chi)}_k & \gamma^{(Z)}_k & 0 \\ -\gamma^{(\phi)}_k & 0 & \gamma^{(Z)}_k \end{pmatrix}, \; P^{(\chi)}_k = \begin{pmatrix} -\gamma^{(\chi)}_k & -\gamma^{(Z)}_k & 0 \\ -\gamma^{(Z)}_k & \gamma^{(\chi)}_k & -\gamma^{(\phi)}_k \\ 0 & -\gamma^{(\phi)}_k & -\gamma^{(\chi)}_k \end{pmatrix},$$

$$P^{(\phi)}_k = \begin{pmatrix} -\gamma^{(\phi)}_k & 0 & -\gamma^{(Z)}_k \\ 0 & \gamma^{(\phi)}_k & \gamma^{(\chi)}_k \\ \gamma^{(Z)}_k & \gamma^{(\chi)}_k & -\gamma^{(\phi)}_k \end{pmatrix}. \tag{6.12}$$

Natural Fermi surface scattering

Let us now assume that α is significantly smaller than unity. In such a case we can assume that contributions away from the Fermi level contribute to small degree to the overall electron self-energy. It is therefore justified to confine k_1 and k_2 to the Fermi surface, compare center of Fig. 6.2. Note, that there is no direct justification for confining also $k_2 - k_1 + k$ to the Fermi surface, which is why this state can occur anywhere throughout the electronic bandwidth. In Section 2.1 we already encountered how to derive Fermi-surface based equations, but it is worthwhile to repeat the basic steps here.

The momentum sum over any function $f(\xi_{\mathbf{k}}, \mathbf{k})$ can be written as

$$\sum_{\mathbf{k}} f(\xi_{\mathbf{k}}, \mathbf{k}) = \int_{-\infty}^{\infty} \mathrm{d}\varepsilon N(\varepsilon) f(\varepsilon, \mathbf{k}), \tag{6.13}$$

where we assume infinite bandwidth of the electron dispersion. Since the electron density of states is given by $N(\varepsilon) = \sum_{\mathbf{k}} \delta(\xi_{\mathbf{k}} - \varepsilon)$, we can write

$$\sum_{\mathbf{k}} f(\xi_{\mathbf{k}}, \mathbf{k}) = \sum_{\mathbf{k}} \delta(\xi_{\mathbf{k}}) \int_{-\infty}^{\infty} \mathrm{d}\varepsilon f(\varepsilon, \mathbf{k}). \tag{6.14}$$

In the last step we have used the assumption that only processes at the Fermi surface significantly contribute to the evaluation of the momentum sum, therefore we set $\varepsilon = 0$ inside the delta function.

Using the definition $\lambda_q = N_0 V_q$, with N_0 the density of states at the Fermi level, we are now in the position to rewrite the electron self-energy from Eq. (6.9) as

$$\begin{aligned} \hat{\Sigma}_k =& T \sum_{k_1} \frac{\delta(\xi_{k_1})}{N_0} \lambda_{k-k_1} \hat{\rho}_3 \hat{g}_{k_1} \hat{\rho}_3 \\ &+ T^2 \sum_{k_1, k_2} \frac{\delta(\xi_{k_1})}{N_0} \frac{\delta(\xi_{k_2})}{N_0} \lambda_{k-k_1} \lambda_{k_1-k_2} \hat{\rho}_3 \hat{g}_{k_1} \hat{\rho}_3 \hat{g}_{k_2} \hat{\rho}_3 \hat{G}_{k_2-k_1+k} \hat{\rho}_3. \end{aligned} \tag{6.15}$$

The modified Green's functions in Eq. (6.15) are given by

$$\hat{g}_k = \int_{-\infty}^{\infty} \mathrm{d}\varepsilon \hat{G}_k(\varepsilon) = -\pi \frac{i\omega_k Z_k \hat{\rho}_0 + \phi_k \hat{\rho}_1}{\sqrt{\omega_k^2 Z_k^2 + \phi_k^2}}. \tag{6.16}$$

Note, that the prefactor of $\hat{\rho}_3$ identically cancels because it is an odd function with respect to the integration variable. For the current case of 'natural Fermi surface scattering' we omit to derive the corresponding Eliashberg equations. The reason is that no advantage is apparent when such equations are solved numerically: Even though the assumption of Fermi surface scattering has been made, i.e. the approach is more restrictive than the general case, the computational costs are identical since electrons with index $k_2 - k_1 + k$ are still to be kept within the full electron bandwidth.

Forced Fermi surface scattering

To improve on the computational costs needed for evaluating the second order electron-phonon scattering contributions, we now demand that the third electronic state $k_2 - k_1 + k$ be also on the Fermi surface. This situation is indicated on the right side of Fig. 6.2. Mathematically, we can accomplish such a situation by artificially introducing a delta function:

$$f(\xi_{\mathbf{k}}, \mathbf{k}) = \int_{-\infty}^{\infty} \mathrm{d}\varepsilon \delta(\xi_{\mathbf{k}} - \varepsilon) f(\varepsilon, \mathbf{k}) \simeq \delta(\xi_{\mathbf{k}}) \int_{-\infty}^{\infty} \mathrm{d}\varepsilon f(\varepsilon, \mathbf{k}). \tag{6.17}$$

In the second step of Eq. (6.17) we use that $\xi_{\mathbf{k}}$ should be close to the Fermi level, which allows us to set $\varepsilon = 0$ inside the delta function. Using the above property in Eq. (6.15) yields

$$\begin{aligned}\hat{\Sigma}_k = {} & T\sum_{k_1}\frac{\delta(\xi_{k_1})}{N_0}\lambda_{k-k_1}\hat{\rho}_3\hat{g}_{k_1}\hat{\rho}_3 \\ & + T^2\sum_{k_1,k_2}\frac{\delta(\xi_{k_1})}{N_0}\frac{\delta(\xi_{k_2})}{N_0}\delta(\xi_{k_2-k_1+k})\lambda_{k-k_1}\lambda_{k_1-k_2}\hat{\rho}_3\hat{g}_{k_1}\hat{\rho}_3\hat{g}_{k_2}\hat{\rho}_3\hat{g}_{k_2-k_1+k}\hat{\rho}_3 .\end{aligned} \tag{6.18}$$

Next, we use $\Delta_k = \phi_k/Z_k$ to rewrite the Green's function of Eq. (6.16) as

$$\hat{g}_k = -\pi\big(i\gamma_k^{(\omega)}\hat{\rho}_0 + \gamma_k^{(\Delta)}\hat{\rho}_1\big), \tag{6.19}$$

with the definitions $\gamma_k^{(\omega)} = \omega_k/\sqrt{\omega_k^2+\Delta_k^2}$ and $\gamma_k^{(\Delta)} = \Delta_k/\sqrt{\omega_k^2+\Delta_k^2}$. Note, that the chemical potential χ has vanished in the current level of approximation. Therefore we are left with two self-consistent and anisotropic Eliashberg equations for the mass renormalization and gap function, reading

$$\begin{aligned}Z_k = {} & 1 + \frac{\pi T}{\omega_k}\sum_{k_1}\frac{\delta(\xi_{k_1})}{N_0}\lambda_{k-k_1}\gamma_{k_1}^{(\omega)} - \frac{\pi^3T^2}{\omega_k}\sum_{k_1,k_2}\frac{\delta(\xi_{k_1})}{N_0}\frac{\delta(\xi_{k_2})}{N_0}\delta(\xi_{k_2-k_1+k})\lambda_{k-k_1} \\ & \times\lambda_{k_1-k_2}\big[\big(\gamma_{k_1}^{(\Delta)}\gamma_{k_2}^{(\Delta)} + \gamma_{k_1}^{(\omega)}\gamma_{k_2}^{(\omega)}\big)\gamma_{k_2-k_1+k}^{(\omega)} + \big(\gamma_{k_1}^{(\omega)}\gamma_{k_2}^{(\Delta)} - \gamma_{k_1}^{(\Delta)}\gamma_{k_2}^{(\omega)}\big)\gamma_{k_2-k_1+k}^{(\Delta)}\big],\end{aligned} \tag{6.20a}$$

$$\begin{aligned}\Delta_k = {} & \frac{\pi T}{Z_k}\sum_{k_1}\frac{\delta(\xi_{k_1})}{N_0}\lambda_{k-k_1}\gamma_{k_1}^{(\Delta)} - \frac{\pi^3T^2}{Z_k}\sum_{k_1,k_2}\frac{\delta(\xi_{k_1})}{N_0}\frac{\delta(\xi_{k_2})}{N_0}\delta(\xi_{k_2-k_1+k})\lambda_{k-k_1} \\ & \times\lambda_{k_1-k_2}\big[\big(\gamma_{k_1}^{(\Delta)}\gamma_{k_2}^{(\omega)} - \gamma_{k_1}^{(\omega)}\gamma_{k_2}^{(\Delta)}\big)\gamma_{k_2-k_1+k}^{(\omega)} + \big(\gamma_{k_1}^{(\omega)}\gamma_{k_2}^{(\omega)} + \gamma_{k_1}^{(\Delta)}\gamma_{k_2}^{(\Delta)}\big)\gamma_{k_2-k_1+k}^{(\Delta)}\big].\end{aligned} \tag{6.20b}$$

In the above set of equations potentially important contributions are neglected, because the Green's function $\hat{G}_{k_2-k_1+k}$ has been restricted to the Fermi surface without much of justification. However, the formalism is nevertheless appealing as the computational effort is significantly reduced in comparison to Eqs. (6.11). Additionally, it is possible to directly solve Eqs. (6.20) with input from *ab initio* theory, which is useful to estimate the effect of vertex corrections in more realistic systems.

Isotropic case

As mentioned above, we assume here that the electron-phonon interaction is isotropic, $\lambda_{k-k_1} \equiv \lambda_{m-m_1}$. The discussions in the following Sections clearly show that this assumption alone does in general not lead to an isotropic mass renormalization or gap function. Therefore we additionally set $\hat{g}_k \equiv \hat{g}_m$, which could be appropriate if we know *a priori* that the momentum anisotropy in the Green's function is small. The electron self-energy then takes the form

$$\begin{aligned}\hat{\Sigma}_m = T\sum_{m_1}\lambda_{m-m_1}\hat{\rho}_3\hat{g}_{m_1}\hat{\rho}_3 \\ +PT^2\sum_{m_1,m_2}\lambda_{m-m_1}\lambda_{m_1-m_2}\hat{\rho}_3\hat{g}_{m_1}\hat{\rho}_3\hat{g}_{m_2}\hat{\rho}_3\hat{g}_{m_2-m_1+m}\hat{\rho}_3,\end{aligned} \tag{6.21}$$

where the constant factor P is defined as

$$P = \sum_{\mathbf{k}_1,\mathbf{k}_2}\frac{\delta(\xi_{\mathbf{k}_1})}{N_0}\frac{\delta(\xi_{\mathbf{k}_2})}{N_0}\delta(\xi_{\mathbf{k}_2-\mathbf{k}_1+\mathbf{k}}). \tag{6.22}$$

The resulting Eliashberg equations have a similar form as Eqs. (6.20), but now all quantities except P are treated only on the Matsubara frequency axis:

$$\begin{aligned}Z_m^{(\mathrm{iso})} =& 1+\frac{\pi T}{\omega_m}\sum_{m_1}\lambda_{m-m_1}\gamma^{(\omega)}_{m_1} - P\frac{\pi^3T^2}{\omega_m}\sum_{m_1,m_2}\lambda_{m-m_1}\lambda_{m_1-m_2}\Big[\big(\gamma^{(\Delta)}_{m_1}\gamma^{(\Delta)}_{m_2} \\ &+\gamma^{(\omega)}_{m_1}\gamma^{(\omega)}_{m_2}\big)\gamma^{(\omega)}_{m_2-m_1+m}+\big(\gamma^{(\omega)}_{m_1}\gamma^{(\Delta)}_{m_2}-\gamma^{(\Delta)}_{m_1}\gamma^{(\omega)}_{m_2}\big)\gamma^{(\Delta)}_{m_2-m_1+m}\Big],\end{aligned} \tag{6.23a}$$

$$\begin{aligned}\Delta_m^{(\mathrm{iso})} =& \frac{\pi T}{Z_m}\sum_{m_1}\lambda_{m-m_1}\gamma^{(\Delta)}_{m_1} - P\frac{\pi^3T^2}{Z_m}\sum_{m_1,m_2}\lambda_{m-m_1}\lambda_{m_1-m_2}\Big[\big(\gamma^{(\Delta)}_{m_1}\gamma^{(\omega)}_{m_2} \\ &-\gamma^{(\omega)}_{m_1}\gamma^{(\Delta)}_{m_2}\big)\gamma^{(\omega)}_{m_2-m_1+m}+\big(\gamma^{(\omega)}_{m_1}\gamma^{(\omega)}_{m_2}+\gamma^{(\Delta)}_{m_1}\gamma^{(\Delta)}_{m_2}\big)\gamma^{(\Delta)}_{m_2-m_1+m}\Big].\end{aligned} \tag{6.23b}$$

We have added the label (iso) in Eqs. (6.23) for later reference.

6.1.3 Numerical solution

Before moving to the summary of Paper X the interested reader is provided in the current subsection with supplementary information on how to numerically implement vertex-corrected Eliashberg equations, as this is a rather difficult task. If the computational aspects are of no direct interest, the reader might continue with Section 6.2.

In the current section we choose to write the four-momentum dependencies explicitly, as they are of primary importance, $f_k = f_{\mathbf{k},m}$ for fermionic and $g_q = g_{\mathbf{q},l}$ for bosonic functions. For all quantities under consideration we assume momentum inversion symmetry, i.e.

$$f_{\mathbf{k},m} = f_{-\mathbf{k},m} \;\;,\;\; g_{\mathbf{q},l} = g_{-\mathbf{q},l}. \tag{6.24}$$

Further, we denote the symmetry along the Matsubara frequency axis as

$$f_{\mathbf{k},m} = (-1)^f f_{\mathbf{k},-m-1} \;\;,\;\; g_{\mathbf{q},l} = (-1)^g g_{\mathbf{q},-l}, \tag{6.25}$$

with the notation

$$(-1)^f = \begin{cases} +1 \text{ , if } f \text{ even in frequency} \\ -1 \text{ , if } f \text{ odd in frequency}\end{cases}. \tag{6.26}$$

In Eq. (6.25) it is important to recognize the difference of inverting fermionic and bosonic frequency grids.

Each of the vertex-corrected Eliashberg equations takes the generic form

$$f_{\mathbf{k},m} = f^{(1)}_{\mathbf{k},m} + f^{(2)}_{\mathbf{k},m}, \tag{6.27}$$

where $f^{(1)}_{\mathbf{k},m}$ and $f^{(2)}_{\mathbf{k},m}$ describe the first and second order electron-phonon scattering contributions, respectively. In a general way we can write

$$f^{(1)}_{\mathbf{k},m} = c \sum_{\mathbf{k}_1,m_1} \alpha_{\mathbf{k}-\mathbf{k}_1,m-m_1} \beta_{\mathbf{k}_1,m_1}, \tag{6.28}$$

which can be implemented as

$$f^{(1)}_{\mathbf{k},m} = c\mathscr{F}^{-1}\big\{\mathscr{F}\big(\alpha_{\mathbf{k}-\mathbf{k}_1,m-m_1}\big) \star \mathscr{F}\big(\beta_{\mathbf{k}_1,m_1}\big)\big\}, \tag{6.29}$$

numerically speaking, compare also Section 2.1. Here, $\mathscr{F}$ ($\mathscr{F}^{-1}$) denotes the forward (backward) Fourier transform in momentum and frequency space.

The second term, which is much more difficult to calculate numerically, can be expressed as

$$\begin{aligned} f^{(2)}_{\mathbf{k},m} = c \sum_{\mathbf{k}_1,m_1} \sum_{\mathbf{k}_2,m_2} & \alpha_{\mathbf{k}-\mathbf{k}_1,m-m_1} \alpha_{\mathbf{k}_1-\mathbf{k}_2,m_1-m_2} \beta_{\mathbf{k}_1,m_1} \\ & \times \delta_{\mathbf{k}_2,m_2} \varepsilon_{\mathbf{k}_2-\mathbf{k}_1+\mathbf{k},m_2-m_1+m}, \end{aligned} \tag{6.30}$$

where function α enters twice, resembling the bosonic electron-phonon interaction. A direct implementation of Eq. (6.30) would be very inefficient and of little use for practical applications. For this reason we aim at using Fourier transforms to speed up the computation, which requires some work to ensure that each function subject to Fourier transformation is centered around the origin of the Matsubara frequency axis.

To start with, we make the reasonable assumption that f and $f^{(2)}$ share the same frequency symmetry, so that we can write

$$f^{(2)}_{\mathbf{k},m} = \frac{1}{2}\big(f^{(2)}_{\mathbf{k},m} + (-1)^f f^{(2)}_{\mathbf{k},-m-1}\big). \tag{6.31}$$

Inserting Eq. (6.30) into Eq. (6.31) gives

$$\begin{aligned} f^{(2)}_{\mathbf{k},m} = (-1)^\alpha \frac{c}{2} \sum_{\mathbf{k}_1,m_1} \sum_{\mathbf{k}_2,m_2} & \alpha_{\mathbf{k}_1-\mathbf{k}_2,m_1-m_2} \beta_{\mathbf{k}_1,m_1} \delta_{\mathbf{k}_2,m_2} \big\{ \alpha_{\mathbf{k}_1-\mathbf{k},m_1-m} \\ & \times \varepsilon_{\mathbf{k}_2-\mathbf{k}_1+\mathbf{k},m_2-m_1+m} + (-1)^f \alpha_{\mathbf{k}_1-\mathbf{k},m+m_1+1} \varepsilon_{\mathbf{k}_2-\mathbf{k}_1+\mathbf{k},m_2-m_1-m-1} \big\}, \end{aligned} \tag{6.32}$$

where we used momentum inversion and frequency symmetry of α. Next, we define the zero-centered frequency symmetric (in m) function

$$\Lambda_{\mathbf{k}_1-\mathbf{k},|m|,m_1} = \frac{1}{2}\big(\alpha_{\mathbf{k}_1-\mathbf{k},m_1-m} + \alpha_{\mathbf{k}_1-\mathbf{k},m+m_1+1}\big), \tag{6.33}$$

which allows us to express

$$\alpha_{\mathbf{k}_1-\mathbf{k},m+m_1+1} = 2\Lambda_{\mathbf{k}_1-\mathbf{k},|m|,m_1} - \alpha_{\mathbf{k}_1-\mathbf{k},m_1-m}. \tag{6.34}$$

By inserting Eq. (6.34) into Eq. (6.32) we find

$$\begin{aligned} f^{(2)}_{\mathbf{k},m} =& (-1)^{\alpha}\frac{c}{2}\sum_{\mathbf{k}_1,m_1}\sum_{\mathbf{k}_2,m_2} \alpha_{\mathbf{k}_1-\mathbf{k}_2,m_1-m_2}\beta_{\mathbf{k}_1,m_1}\delta_{\mathbf{k}_2,m_2} \\ &\times\big\{\alpha_{\mathbf{k}_1-\mathbf{k},m_1-m}\big[\varepsilon_{\mathbf{k}_2-\mathbf{k}_1+\mathbf{k},m_2-m_1+m} - (-1)^f\varepsilon_{\mathbf{k}_2-\mathbf{k}_1+\mathbf{k},m_2-m_1-m-1}\big] \\ &+2(-1)^f\Lambda_{\mathbf{k}_1-\mathbf{k},|m|,m_1}\varepsilon_{\mathbf{k}_2-\mathbf{k}_1+\mathbf{k},m_2-m_1-m-1}\big\}. \end{aligned} \tag{6.35}$$

Considering the numerical implementation, let as perform a loop over momenta $\mathbf{k}$ and frequencies m. Then, for each pair $(\mathbf{k},m)$ we can carry out explicit index shifts, so as to define

$$\tilde{\alpha}_{\mathbf{k}_1,m_1} = \alpha_{\mathbf{k}_1-\mathbf{k},m_1-m}, \tag{6.36a}$$

$$\tilde{\Lambda}_{\mathbf{k}_1,m_1} = \Lambda_{\mathbf{k}_1-\mathbf{k},|m|,m_1}, \tag{6.36b}$$

$$\tilde{\varepsilon}^{(-)}_{\mathbf{k}_2-\mathbf{k}_1,m_2-m_1} = \varepsilon_{\mathbf{k}_2-\mathbf{k}_1+\mathbf{k},m_2-m_1+m} - (-1)^f\varepsilon_{\mathbf{k}_2-\mathbf{k}_1+\mathbf{k},m_2-m_1-m-1}. \tag{6.36c}$$

Further, we split Eq. (6.35) according to the two summands in the curly brackets, i.e. $f^{(2)}_{\mathbf{k},m} = f^{(2,a)}_{\mathbf{k},m} + f^{(2,b)}_{\mathbf{k},m}$. For the first term we use Eqs. (6.35) and (6.36), so that for each ($\mathbf{k}$,m) we get

$$f^{(2,a)}_{\mathbf{k},m} = \frac{c}{2}\sum_{\mathbf{k}_1,m_1}\sum_{\mathbf{k}_2,m_2}\tilde{\beta}_{\mathbf{k}_1,m_1}\delta_{\mathbf{k}_2,m_2}\tau^{(-)}_{\mathbf{k}_2-\mathbf{k}_1,m_2-m_1}. \tag{6.37}$$

Equation (6.37) is derived by using symmetries of α and the straight-forward definitions

$$\tilde{\beta}_{\mathbf{k}_1,m_1} = \beta_{\mathbf{k}_1,m_1}\tilde{\alpha}_{\mathbf{k}_1,m_1}, \tag{6.38a}$$

$$\tau^{(-)}_{\mathbf{k}_2-\mathbf{k}_1,m_2-m_1} = \alpha_{\mathbf{k}_2-\mathbf{k}_1,m_2-m_1}\tilde{\varepsilon}^{(-)}_{\mathbf{k}_2-\mathbf{k}_1,m_2-m_1}. \tag{6.38b}$$

The functional form of $f^{(2,a)}$ can now be cast efficiently as

$$f^{(2,a)}_{\mathbf{k},m} = \frac{c}{2}\sum_{\mathbf{k}_2,m_2}\delta_{\mathbf{k}_2,m_2}\mathscr{F}^{-1}\big\{\mathscr{F}\big(\tilde{\beta}_{\mathbf{k}_1,m_1}\big)\star\mathscr{F}\big(\tau^{(-)}_{\mathbf{k}_2-\mathbf{k}_1,m_2-m_1}\big)\big\}_{\mathbf{k}_2,m_2}. \tag{6.39}$$

Considering the remaining expression $f^{(2,b)}$, we use again the symmetry argument along the Matsubara axis, i.e. $f^{(2,b)}_{\mathbf{k},m} = \frac{1}{2}\big(f^{(2,b)}_{\mathbf{k},m} + (-1)^f f^{(2,b)}_{\mathbf{k},-m-1}\big)$, so as to obtain zero-centered inputs for the Fourier transforms. We get

$$f^{(2,b)}_{\mathbf{k},m} = (-1)^{\alpha}(-1)^f\frac{c}{2}\sum_{\mathbf{k}_1,m_1}\sum_{\mathbf{k}_2,m_2}\alpha_{\mathbf{k}_1-\mathbf{k}_2,m_1-m_2}\beta_{\mathbf{k}_1,m_1}\delta_{\mathbf{k}_2,m_2}\tilde{\varepsilon}^{(+)}_{\mathbf{k}_2-\mathbf{k}_1,m_2-m_1}\tilde{\Lambda}_{\mathbf{k}_1,m_1}, \tag{6.40}$$

with the definition

$$\tilde{\varepsilon}^{(+)}_{\mathbf{k}_2-\mathbf{k}_1,m_2-m_1} = \varepsilon_{\mathbf{k}_2-\mathbf{k}_1+\mathbf{k},m_2-m_1-m-1} + (-1)^f \varepsilon_{\mathbf{k}_2-\mathbf{k}_1+\mathbf{k},m_2-m_1+m}. \tag{6.41}$$

Finally, we group the indices according to

$$\tau^{(+)}_{\mathbf{k}_2-\mathbf{k}_1,m_2-m_1} = \alpha_{\mathbf{k}_2-\mathbf{k}_1,m_2-m_1} \tilde{\varepsilon}^{(+)}_{\mathbf{k}_2-\mathbf{k}_1,m_2-m_1}, \tag{6.42a}$$

$$\eta_{\mathbf{k}_1,m_1} = \beta_{\mathbf{k}_1,m_1} \tilde{\Lambda}_{\mathbf{k}_1,m_1}, \tag{6.42b}$$

leaving us with the simpler-looking term

$$f^{(2,b)}_{\mathbf{k},m} = (-1)^f \frac{c}{2} \sum_{\mathbf{k}_1,m_1} \sum_{\mathbf{k}_2,m_2} \eta_{\mathbf{k}_1,m_1} \delta_{\mathbf{k}_2,m_2} \tau^{(+)}_{\mathbf{k}_2-\mathbf{k}_1,m_2-m_1}, \tag{6.43}$$

which can be written as Fourier convolution in indices $(\mathbf{k}_1,m_1)$:

$$f^{(2,b)}_{\mathbf{k},m} = (-1)^f \frac{c}{2} \sum_{\mathbf{k}_2,m_2} \delta_{\mathbf{k}_2,m_2} \mathscr{F}^{-1}\left\{\mathscr{F}\left(\eta_{\mathbf{k}_1,m_1}\right) \star \mathscr{F}\left(\tau^{(+)}_{\mathbf{k}_2-\mathbf{k}_1,m_2-m_1}\right)\right\}_{\mathbf{k}_2,m_2}. \tag{6.44}$$

The recipe provided above is rather lengthy and cumbersome to implement numerically. However, doing so decreases the computational costs for $\mathscr{N}$ sampling points in four-momentum space from $\mathscr{O}(\mathscr{N}^3)$ to $\mathscr{O}(\mathscr{N}^2 \log \mathscr{N})$. At first glance, this might not look like a tremendous improvement, but none of the Papers X, XI, XIII would have been possible without the Fourier convolution techniques introduced here.

6.2 Phase space exploration

In Paper X we explored the possible effects of vertex corrections in Eliashberg theory as function of the nonadiabaticity parameter α, coupling strength λ and dimensionality of the system. To do so, we chose several different levels of approximations to the Eliashberg equations and solved each of them self-consistently for a given set of parameters. Comparing the results gave us a better understanding under which circumstances each respective approximation is applicable, in comparison to the outcomes from the vertex-corrected Eliashberg theory. Additionally, this procedure provided us with key insights on the sign and magnitude of the said vertex corrections to the superconducting gap and other quantities.

Not many studies have been carried out on the current subject matter, except for the original work by Migdal [4], a series of papers by Pietronero et al. [128, 130–134] and few other works [129, 135–137]. In contrast to our study, these authors discussed the possible influence of vertex corrections to the electron-phonon problem under various, partially rather drastic approximations, such as simplified or neglected momentum dependencies, extrapolation of normal state properties to the superconducting state, or Fermi surface averaged quantities. In our work we solved Eqs. (6.11) without any approximations, keeping the full momentum and frequency dependencies. Therefore, we were able to compare our results to prior literature only in few limiting cases, see discussion below.

The different theories used in Paper X can be described as follows:

- Complete, nonadiabatic theory, solving Eqs. (6.11) for $Z_{\mathbf{k},m}$, $\chi_{\mathbf{k},m}$ and $\phi_{\mathbf{k},m}$ ($\Delta_{\mathbf{k},m} = \phi_{\mathbf{k},m}/Z_{\mathbf{k},m}$).
- Isotropic, Fermi surface restricted approximation to the nonadiabatic equations, solving Eqs. (6.23) for $Z_m^{(\mathrm{iso})}$ and $\Delta_m^{(\mathrm{iso})}$.
- Adiabatic theory, solving Eqs. (6.11) *without* the vertex correction part for the quantities

$$Z_k^{(\mathrm{ad})} = 1 - \frac{T}{\omega_k} \sum_{k_1} V_{k-k_1} \gamma_{k_1}^{(Z)}, \tag{6.45a}$$

$$\chi_k^{(\mathrm{ad})} = T \sum_{k_1} V_{k-k_1} \gamma_{k_1}^{(\chi)}, \tag{6.45b}$$

$$\phi_k^{(\mathrm{ad})} = -T \sum_{k_1} V_{k-k_1} \gamma_{k_1}^{(\phi)}, \tag{6.45c}$$

  ($\Delta_k^{(\mathrm{ad})} = \phi_k^{(\mathrm{ad})}/Z_k^{(\mathrm{ad})}$).
- Fermi surface restricted, adiabatic theory, solving Eqs. (6.20) *without* the vertex correction part for

$$Z_k^{(\mathrm{Fs})} = 1 + \frac{\pi T}{\omega_k} \sum_{k_1} \frac{\delta(\xi_{k_1})}{N_0} \lambda_{k-k_1} \gamma_{k_1}^{(\omega)}, \tag{6.46a}$$

$$\Delta_k^{(\mathrm{Fs})} = \frac{\pi T}{Z_k} \sum_{k_1} \frac{\delta(\xi_{k_1})}{N_0} \lambda_{k-k_1} \gamma_{k_1}^{(\Delta)}. \tag{6.46b}$$

The electron energies are chosen here as single band, next-nearest neighbor tight-binding model

$$\xi_{\mathbf{k}} = -t^{(1)} \sum_{i=x,y,z} c_i \cos(k_i) - t^{(2)} \sum_{i=x,y,z} \prod_{j=x,y,z;\, j\neq i} c_j \cos(k_j) - \mu, \tag{6.47}$$

which can be used for 1D, 2D and 3D systems. Above, $c_x = 1$ and $c_{i\neq x} \in \{0,1\}$ control the dimensionality. We focus on the 2D and 3D cases here, choosing the hopping energies as $t^{(2)} = t^{(1)}/2$ and $t^{(1)} = W/2\sum_{i=x,y,z} c_i$, with electronic bandwidth $W = |\max_{\mathbf{k}}(\xi_{\mathbf{k}}) - \min_{\mathbf{k}}(\xi_{\mathbf{k}})| = 1.5\,\mathrm{eV}$. The phonon frequency is fixed at $\Omega = 50\,\mathrm{meV}$ and for now we consider a temperature of $T = 20\,\mathrm{K}$. By varying the electron-phonon coupling strength λ, which is used in the Fermi surface averaged theories listed above, we make a connection to the full electron bandwidth equations by identifying the scattering strength as

$$g_0^2 = \frac{\lambda \Omega}{2N_0}. \tag{6.48}$$

The electron density of states at the Fermi level can directly be calculated from the electron energies, $N_0 = \sum_{\mathbf{k}} \delta(\xi_{\mathbf{k}})$. In the following we choose three different values for the degree of nonadiabaticity, namely $\alpha \in \{0.05, 0.1, 1\}$, for both 2D and 3D systems. The smaller the value of α is chosen, the larger the electron filling. For example, in 3D, $\alpha = 0.05$ resembles the situation of an ideal Fermi gas to good degree, while $\alpha = 1$ corresponds to a very shallow energy band. The results for the maximum superconducting gap as function of coupling strength are shown in Fig. 6.3, where different colors/symbols correspond to the above listed levels of approximation, as indicated in the legends. As a side note, all superconducting gap symmetries obtained in Paper X are exclusively s-wave.

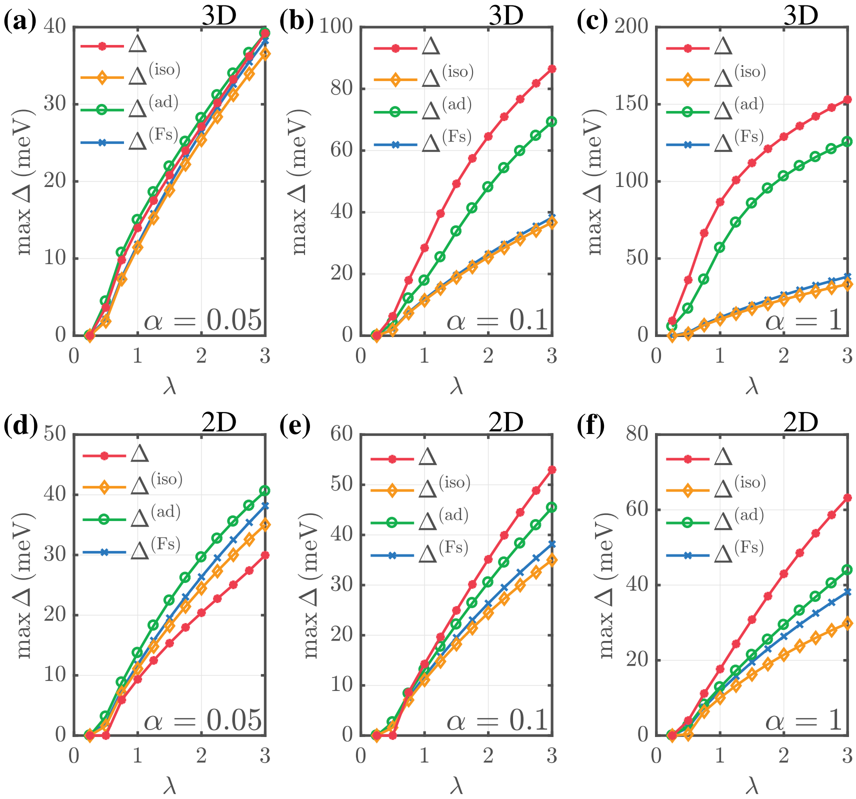

Figure 6.3. Maximum zero-frequency superconducting gap as function of electron-phonon coupling strength λ, calculated for $\Omega = 50\,\text{meV}$ and $T = 20\,\text{K}$. The degree of nonadiabaticity α is written in each panel. Different colors correspond to levels of approximation as indicated in the legends. Graphs (a-c) and (d-f) show results for 3D and 2D systems, respectively. Figures taken from Paper X.

The first important thing to notice is the confirmation of Migdal's theorem in Fig. 6.3(a). All curves fall essentially on top of each other, meaning that the adiabatic Fermi surface restricted theory provides an accurate description of the superconducting state in a 3D system with $\alpha \ll 1$, which is Migdal's theorem [4]. This result was expected and can therefore be seen as a benchmark for our numerical implementation. As we increase α to 0.1 and 1 in panels (b) and (c), the deviation between results from Fermi surface restricted theories, $\Delta^{(\mathrm{Fs})}$ and $\Delta^{(\mathrm{iso})}$, to our reference curve Δ grows significantly larger, both with increasing α and λ. Further, we learn that $\Delta^{(\mathrm{ad})}$ seems to always be a good approximation to Δ regardless of coupling strength. In the 3D case the vertex corrections, if significant, increase the size of the superconducting gap, which might likely reflect in an increase of transition temperature.

Turning to the 2D systems, we find in Fig. 6.3(d) that a small value of α leads to an overestimation of all approximative theories $\Delta^{(\mathrm{iso})}$, $\Delta^{(\mathrm{ad})}$ and $\Delta^{(\mathrm{Fs})}$, in comparison to the red curve for Δ. This means that the vertex correction adds negatively to the superconductivity order parameter, a behavior that has not been encountered for 3D systems. The situation changes upon increase of α to 0.1 and 1, see Fig. 6.3(e) and (f): Here the second order electron-phonon scattering processes add positively to the gap magnitude, leading to a larger Δ compared to the other three approaches. The adiabatic full bandwidth results $\Delta^{(\mathrm{ad})}$ stay closest to the reference curves, but increasingly deviate with growing λ. It is further notable that $\Delta^{(\mathrm{Fs})}$ is a better approximation to Δ than $\Delta^{(\mathrm{iso})}$, while both also become worse estimates for larger coupling strengths. In fact, all of Fig. 6.3 points towards highly inaccurate results $\Delta^{(\mathrm{iso})}$ from isotropic, Fermi surface averaged Eliashberg theory, which leads us to the conclusion that this level of approximation is not well suited for most situations, except in the strongly adiabatic limit in 3D when vertex corrections are insignificant.

A closer examination of the intermediate regime in Fig. 6.3(e) reveals that the vertex corrections are partially positive or negative, depending on the interaction strength. This points towards a smooth transition between the two situations encountered in panels (d) and (f). Further, it is noteworthy that the (quasi) 2D case is the most interesting in terms of current advances in high-temperature superconductivity. It is for this reason that we examine this particular parameter range, relevant for Cu- and Fe-based superconductors [127, 138], in more detail below.

Next, consider the 2D system with electron-phonon coupling strength $\lambda = 1.5$. We calculate the maximum superconducting gap as function of temperature and show the outcomes in Fig. 6.4. The colors orange, green and purple correspond to levels of nonadiabaticity $\alpha = 0.05$, $\alpha = 0.1$ and $\alpha = 1$, respectively. The superconducting gaps Δ and $\Delta^{(\mathrm{ad})}$ are drawn as dashed and solid lines, while results from adiabatic, Fermi surface averaged Eliashberg theory are shown as dash-dotted blue curve. Note that, due to the isotropic nature of the electron-phonon interaction, $\Delta^{(\mathrm{Fs})}$ does not depend on α. Our results for $\Delta^{(\mathrm{ad})}$ show that the gap magnitude decreases slightly with growing α, while

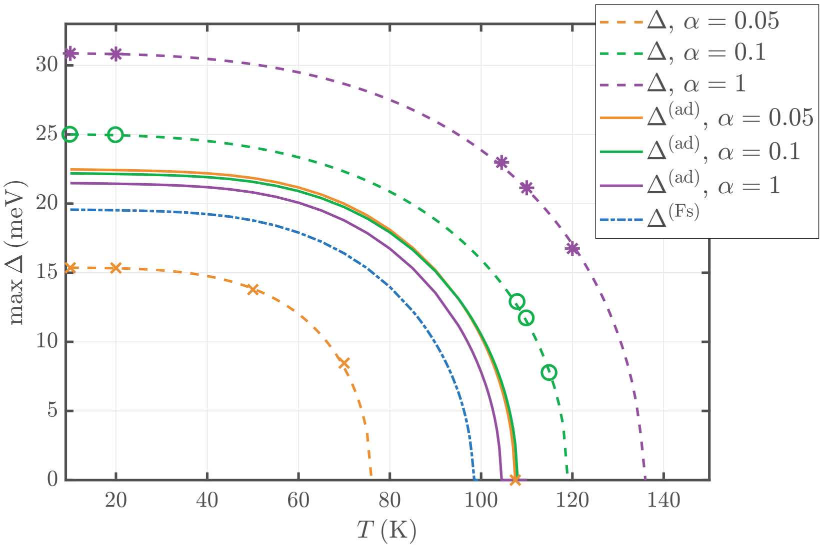

Figure 6.4. Maximum superconducting gap as function of temperature for $\lambda = 1.5$, calculated for 2D systems within different levels of approximation, see legend. Figure taken from Paper X.

the changes remain very small ($T_c \sim 100\,\mathrm{K}$). Approximately the same result (slightly smaller gap magnitude) is obtained from $\Delta^{(\mathrm{Fs})}$. The difference stems from Cooper pairing away from the Fermi level, which is included in the full bandwidth, but not in the Fermi surface averaged formalism.

When we compare these curves with results from vertex-corrected Eliashberg theory the conclusions are heavily α-dependent. For the most adiabatic situation, $\alpha = 0.05$, the vertex corrections reduce the maximally possible gap size and the superconducting T_c ($\sim 75\,\mathrm{K}$). This precisely matches the observations in connection to Fig. 6.3(d). At intermediate electron filling we find a slight, but noticeable increase in T_c and Δ, because the magnitude of vertex corrections is rather small and positive, compare Fig. 6.3(e) at $\lambda = 1.5$. Finally, as expected from Fig. 6.3(f), we find a significantly larger critical temperature ($T_c \sim 135\,\mathrm{K}$) and gap magnitude for $\alpha = 1$, i.e. for the most shallow electron band.

To quantify the aspect of positive and negative contributions due to vertex corrections, we employ the effective electron-phonon coupling constant of the system, which is commonly calculated as

$$\lambda_Z^{(\mathrm{ad/Fs})} = \langle Z^{(\mathrm{ad/Fs})}_{\mathbf{k},m=0} \rangle_{\mathbf{k}_F} \big|_{T > T_c^{(\mathrm{ad/Fs})}} - 1. \tag{6.49}$$

A first estimate for this coupling in vertex-corrected Eliashberg theory can simply be given by

$$\lambda_Z = \langle Z_{\mathbf{k},m=0} \rangle_{\mathbf{k}_F} |_{T>T_c, T>T_c^{(\mathrm{ad})}, T>T_c^{(\mathrm{Fs})}} - 1 = \lambda_Z^{(1)} + \lambda_Z^{(2)}, \tag{6.50}$$

where $\lambda_Z^{(1)}$ and $\lambda_Z^{(2)}$ are associated with the first and second order Feynman diagrams. Note, that Eq. (6.50) is only an approximation to observe the underlying trends. A more rigorous expression for the effective electron-phonon coupling strength is given in Section 7.1. In Table 6.1 we list our results for the couplings calculated for the same parameters used in Fig. 6.4. We skip the results for the adiabatic Fermi surface averaged theory, since $\lambda_Z^{(\mathrm{Fs})} \equiv \lambda$ due to the fact that we consider an isotropic interaction.

Table 6.1. *Effective electron-phonon coupling strength for different degrees of nonadiabaticity. The first row is obtained from Eq. (6.49), the remaining rows are determined from Eq. (6.50). Table taken from Paper X.*

	$\alpha = 0.05$	$\alpha = 0.1$	$\alpha = 1$
$\lambda_Z^{(\mathrm{ad})}$	1.4016	1.5971	1.4723
$\lambda_Z^{(1)}$	1.4015	1.5972	1.4671
$\lambda_Z^{(2)}$	−0.5496	−0.0462	0.4060
λ_Z	0.8519	1.5510	1.8731

First, we observe that $\lambda_Z^{(\mathrm{ad})} \simeq \lambda_Z^{(1)}$ for all values of α considered here. This is due to the fact that both quantities represent the first order electron-phonon scattering processes, and hence the contributions are expected to be similar. For $\alpha = 1$ the overall coupling is significantly enhanced by the vertex corrections, which results in the strong increase of T_c in Fig. 6.4. For the intermediate case of $\alpha = 0.1$ we find $\lambda_Z^{(2)}$ to be a small and negative number. This coincides with observations in Fig. 6.4 insofar as the second order Feynman diagram does not lead to a very large change in Δ or T_c. The most adiabatic system $\alpha = 0.05$ shows significant reduction in the effective coupling strength, which causes the above mentioned drop in T_c, when compared to the purely adiabatic results.

To summarize, in Paper X we confirmed Migdal's theorem and explored a substantial part of phase space spanned by our parameters. Our findings indicate that adiabatic Eliashberg theory for 3D systems is often a good approximation, leading to the correct trends and orders of magnitude regarding the superconducting gap. In 2D the situation is more involved, as vertex corrections can have positive or negative sign, and therefore enhance or reduce T_c. This picture is in accordance with prior estimates [131,139]. Many (quasi) 2D superconductors, such as Cu- or Fe-based materials, lie in a parameter regime where vertex corrections are expected to play an important role. In the following Chapter 7 we will explore those systems in more detail.

7. Exotic superconducting states

> *Simpler explanations are, other things being equal, generally better than more complex ones.*
>
> William of Ockham

Here we use the extended Eliashberg theory introduced in Chapter 6 to explore different exotic phenomena in superconductors, which can only be observed due to the inclusion of vertex corrections to the electron-phonon interaction. The word ‘exotic’ is used here in comparison to the general conception of superconducting states that can originate from isotropic electron-phonon coupling. As we show in the summary of Paper XI in Section 7.1, such an interaction can in fact produce unconventional, i.e. sign-changing symmetries of the superconducting gap in the families of Cu-based, Fe-based and heavy fermion superconductors. We continue by presenting Paper XII, where the Fe-based system ThFeAsN is shown to be a likely candidate exhibiting an unconventional Brillouin zone symmetry of the superconductivity order parameter due to vertex corrections. In Section 7.3 we discuss the topic of odd-frequency superconductivity. As we show in Paper XIII, vertex corrections to the electron-phonon problem generically allow for the coexistence of two superconducting order parameters, where one is always even, and the other one is odd in frequency space. Even though the experimental verification of this finding might prove challenging, we benchmark our approach successfully in a generic cuprate superconductor.

7.1 Unconventional superconducting gap

Among all results discussed in Section 6.2, the most important one for the discussion about unconventional superconducting states are the effective coupling strengths due to the second order Feynman diagram. We have seen that the effective electron-phonon coupling can be written as $\lambda_Z = \lambda_Z^{(1)} + \lambda_Z^{(2)}$, where $\lambda_Z^{(1)}$ is generally positive. Under suitable circumstances, such as for 2D systems, $\lambda_Z^{(2)}$ can contribute destructively, i.e. have the effect of reducing the overall coupling strength. These (partial) interaction strengths were averaged quantities over the Fermi surface, but consider now each of these λ’s as momentum dependent. It is generally not hard to imagine that the resulting total coupling might have sign changes in momentum space, which might lead to non-trivial effects such as symmetry changes in the superconductivity order parameter.

One additional reason to expect unconventional gap symmetries to emerge under the correct conditions is the work carried out by Hague in Refs. [140, 141]. By using the Dynamical Cluster Approximation for solving vertex-corrected equations for the electron Green's function and self-energy, he was able to show that within this model approach an isotropic electron-phonon interaction in Cu-based superconductors can lead to the experimentally observed d-wave symmetry of the superconducting gap. We therefore wanted to examine this aspect closer, asking two central questions: (i) Can vertex-corrected Eliashberg theory under suitable conditions produce sign-changing symmetries of the superconductivity order parameter? (ii) If so, how generic is this phenomenon and what are the systems it applies to? In the current Section we walk through the answers to both questions step by step.

7.1.1 System properties and self-consistent solutions

In Paper XI we consider three different systems, each representative for a prominent family of superconductors, namely a Cu-based, Fe-based and heavy fermion superconductor. All of these fall into the category of unconventional superconductors, meaning that their respective superconductivity order parameter changes sign in momentum space [39]. In each case we choose characteristic values for the Einstein phonon frequency Ω, the systems temperature $T < T_c$ and the electron-phonon scattering strength. Further, we use materials specific tight-binding models for the electron energies, see below.

Starting with the Cu-based material, we use a one-band next-nearest neighbor tight-binding model for the electron dispersion, reading

$$\xi_{\mathbf{k}} = tc_{x+y} + t'c_{xy} - \mu. \tag{7.1}$$

Above we introduced functions $c_{ax+ay} = \cos(a \cdot k_x) + \cos(a \cdot k_y)$ and $c_{axy} = \cos(a \cdot k_x)\cos(a \cdot k_y)$, $a \in \mathbb{N}$, for brevity. The hopping energies are chosen as $t = -0.25\,\mathrm{eV}$ and $t' = 0.1\,\mathrm{eV}$, so that, together with a chemical potential shift $\mu = -0.07\,\mathrm{eV}$, we get the prototypical Fermi surface as shown in Fig. 7.1(a). Even though the modeling of electron energies as in Eq. (7.1) is rather simple, the result is representative for many cuprate superconductors, such as $\mathrm{Bi_2Sr_2CaCu_2O_8}$ [142] or $\mathrm{La_{2-x}Sr_xCuO_4}$ [143].

For the Fe-based systems we use two energy bands to correctly capture the electron pockets around the M point of the Brillouin zone, and the hole pockets at Γ. The bands

$$\begin{aligned} \xi^{(1)}_{\mathbf{k}} &= tc_{x+y} - \left[K - t'c_{xy}\right] - \mu, \\ \xi^{(2)}_{\mathbf{k}} &= tc_{x+y} + \left[K - t'c_{xy}\right] - \mu, \end{aligned} \tag{7.2}$$

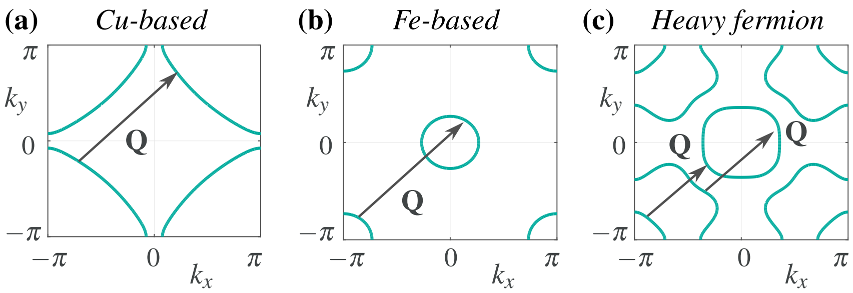

Figure 7.1. Panels (a), (b) and (c) show the Fermi surface of our tight-binding model for exemplary cuprate, Fe-based and heavy fermion superconductor, respectively. The nesting wave vector for (a) and (b) is $\mathbf{Q} \simeq (\pi, \pi)$, while for (c) $\mathbf{Q} \simeq (\pi/2, \pi/2)$.

with parameters $K = 1/3\,\mathrm{eV}$, $t = 1/6\,\mathrm{eV}$, $t' = 1/12\,\mathrm{eV}$ and $\mu = 0\,\mathrm{eV}$, render the Fermi surface in Fig. 7.1(b), which is typical for a broad variety of superconductors, e.g. FeSe [37], $\mathrm{BaFe_2As_2}$ [144], LaFeAsO [145] or LiFeAs [146].

The third system under consideration is a heavy fermion superconductor, where we choose to focus on the well-known example of $\mathrm{CeCoIn_5}$. In the following, when referring to the 'heavy fermion' system we mean this specific material. The corresponding Fermi surface shown in Fig. 7.1(c) is created from a two band tight-binding model

$$\begin{aligned}\xi_{\mathbf{k}}^{(1,2)} =& \frac{\varepsilon_{\mathbf{k}}^{c} + \varepsilon_{\mathbf{k}}^{f}}{2} \pm \sqrt{\left(\frac{\varepsilon_{\mathbf{k}}^{c} + \varepsilon_{\mathbf{k}}^{f}}{2}\right)^2 + s_{\mathbf{k}}^2}, \qquad (7.3)\\ \varepsilon_{\mathbf{k}}^{c} =& -2t_{c_1} c_{x+y} - 4t_{c_2} c_{xy} - 2t_{c_3} c_{2x+2y} - \mu_c,\\ \varepsilon_{\mathbf{k}}^{f} =& -2t_{f_1} c_{x+y} - 4t_{f_2} c_{xy} - 2t_{f_3} c_{2x+2y} - 4t_{f_5} c_{2xy} - 2t_{f_7} c_{3x+3y} + \varepsilon_f,\\ s_{\mathbf{k}} =& s_0 + s_1 \sin^2(k_x)\sin^2(k_y),\end{aligned}$$

which we took from Ref. [147]. The list of hopping energies and other parameters is given by $t_{c_1} = -50\,\mathrm{meV}$, $t_{c_2} = -13.36\,\mathrm{meV}$, $t_{c_3} = -16.73\,\mathrm{meV}$, $\mu_c = -151.51\,\mathrm{meV}$, $t_{f_1} = -0.85\,\mathrm{meV}$, $t_{f_2} = -0.35\,\mathrm{meV}$, $t_{f_3} = -0.8\,\mathrm{meV}$, $t_{f_5} = 0.1\,\mathrm{meV}$, $t_{f_7} = 0.09\,\mathrm{meV}$, $\varepsilon_f = 0.5\,\mathrm{meV}$, $s_0 = 3\,\mathrm{meV}$ and $s_1 = 7\,\mathrm{meV}$.

The arrows in each panel of Fig. 7.1 indicate the respective nesting properties with the exchange vectors $\mathbf{Q} \simeq (\pi, \pi)$ for (a), (b) and $\mathbf{Q} \simeq (\pi/2, \pi/2)$ for (c). Nesting is commonly associated with enhanced tendencies towards antiferromagnetic spin fluctuations [148, 149], which are broadly believed to mediate the superconductivity in these systems. This picture first has been studied for the heavy fermion systems [11, 13, 150], and later also for the Cu-based high-temperature superconductors [151–153]. With the discovery of Fe-based compounds the concept of spin fluctuations has gained further momentum [32, 33, 154, 155], such that this mechanism is now commonly believed to be responsible for unconventional superconductivity [39]. As we show below, this picture is far from being complete because the Fermi surface nesting turns out to play a crucial role also for electron-phonon mediated Cooper pairing.

In our formalism we choose the phonon frequency Ω for each system in accordance to available literature [156–160]. Further, we fix the temperature at a value $T < T_c$, since we are primarily interested in the superconducting state. The only remaining free parameter of our theory is the electron-phonon scattering strength g_0. As done in Section 6.2, we employ again an *isotropic* electron-phonon interaction between a single optical phonon mode and the electronic system. The input coupling strength to our theory can be determined from $\lambda = 2g_0^2 N_0/\Omega$, and the nonadiabaticity ratio is calculated as $\alpha = \Omega/\varepsilon_F$, with ε_F the 'minimal shallowness' of $\xi_{\mathbf{k}}$ (also in the case of two bands). We summarize the parameters for each model system in Table 7.1.

Table 7.1. *Parameters entering the vertex-corrected Eliashberg calculations for each system considered. The first four rows are chosen freely but in accordance to literature, while λ and α are calculated from those choices.*

	Cu-based	*Fe-based*	*Heavy fermion*
Ω (meV)	50 [156]	17 [157]	5 [160]
T (K) $< T_c$	30	15	2
$\xi_{\mathbf{k}}$	Eq. (7.1)	Eq. (7.2)	Eq. (7.3)
g_0 (meV)	148	130	4
λ	2.00	2.85	1.06
α	0.16	0.22	0.14

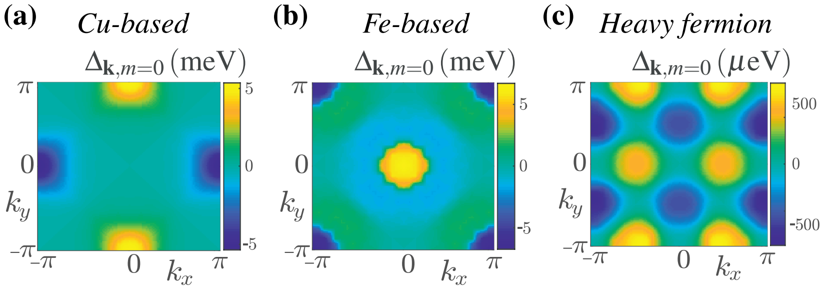

Figure 7.2. Self-consistently calculated zero-frequency superconducting gap. Panels (a), (b) and (c) are results obtained for the Cu-based, Fe-based and heavy fermion superconductor. Figure taken from Paper XI.

We can clearly see from the last line of Table 7.1 that the condition $\alpha \ll 1$ is not met in any of these systems. For this reason we expect vertex corrections to play an important role. Using the above listed parameters we numerically solved the vertex-corrected Eliashberg Eqs. (6.11); the resulting zero-frequency superconducting gaps are shown in Fig. 7.2. As directly apparent, the realistic inputs for the Cu-based system lead to the experimentally observed [161] $d_{x^2-y^2}$-wave symmetry of $\Delta_{\mathbf{k},0}$, where the sign change is dictated by the nesting wave vector $\mathbf{Q} = (\pi,\pi)$. In our model for the Fe-based compound we find the prototypical $s_{\pm}$-wave symmetry [162], where $\Delta_{\mathbf{k},0}$ shows opposite signs between electron and hole bands. Finally, our representative example for the heavy fermion family shows also a (higher-harmonic) $d_{x^2-y^2}$-wave superconducting gap, compatible with the established picture [163].

It is striking that, not only do the symmetries obtained from an isotropic electron-phonon coupling match the experimental situation, also the magnitude of the superconducting gap has the correct range in all three cases. As an example, we find a maximum gap of 800 μeV at $T = 2$ K when projecting $\Delta_{\mathbf{k},m=0}$ onto the Fermi surface in the case of CeCoIn$_5$. Fasano et al. measured a similar value of 620 μeV in CeCoIn$_5$ at the same temperature [163]. The outcomes for our models of Cu-based and Fe-based superconductors are in equally realistic regimes. To further stress the agreement of our calculations with experiment we show the temperature evolution of the maximum superconducting gap $\Delta_0 = \max \Delta_{\mathbf{k}_\mathrm{F},m=0}$ for the cuprate compound in Fig. 7.3. The transition temperature $T_c \simeq 52$ K has the correct order of magnitude for the materials under consideration. Further it should be noted that Δ_0 and T_c can be fine tuned by slightly varying Ω and g_0. Our main goal here, however, is not to fully explain all details of the superconducting state in these materials, but rather raise the awareness that electron-phonon interactions might likely play a more important role than is generally believed.

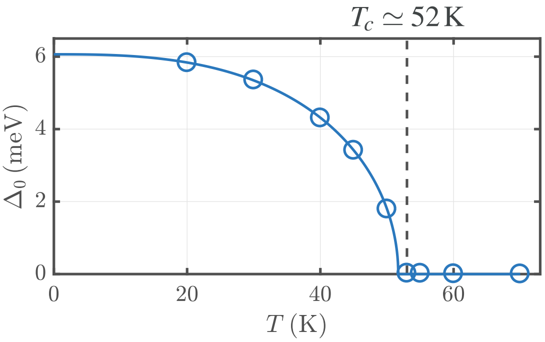

Figure 7.3. Temperature dependence of the superconducting gap function for our model cuprate system, obtained from self-consistent solutions of the vertex-corrected Eliashberg equations. Figure taken from Paper XI.

Since, for the Cu-based compound we have calculated the full temperature dependence, we can get an estimate of the effective electron-phonon coupling strength in the system. Recall the relatively large input coupling $\lambda = 2$ from Table 7.1, which, however, is merely an input parameter not reflecting the actual coupling strength. The self-consistent solutions of the interacting state above T_c allow us to calculate an estimate of this quantity by evaluating $\langle Z_{\mathbf{k},m=0}\rangle_{\mathbf{k_F}}|_{T>T_c}$. Without vertex corrections this expression is equal to $1+\lambda_Z$, see earlier Chapters. Now, the second order Feynman diagram introduces an additional contribution, which we can calculate by setting $\phi = 0$ in Eq. (6.11a), since $T > T_c$, approximating $\chi \simeq 0$, evaluating all momentum sums as energy integrals and performing the Matsubara frequency sums analytically. The result reads

$$\langle Z_{\mathbf{k},m=0}\rangle_{\mathbf{k_F}}|_{T>T_c} = 1+\lambda_Z - \lambda_Z^2 \frac{\pi^2 \Omega N_0}{4} \frac{3\sinh(\Omega/T) - \Omega/T}{\cosh(\Omega/T) - 1}, \tag{7.4}$$

which is a second order polynomial in λ_Z. For the Cu-based system at $T = 70\,\mathrm{K}$ we find $\lambda_Z = 0.34$ and $\lambda_Z = 0.85$ as solutions, which in both cases is a significant reduction in comparison to the input coupling $\lambda = 2$. Experimentally it has been shown that an upper bound for the coupling strength is given by approximately unity [156], which compares well to our estimates.

Now that the three model systems have been introduced, together with some particular aspects of each respective superconducting state, we want to analyze the solutions to Eliashberg theory in greater detail in Section 7.1.2, so as to answer the question about the origin of unconventional Cooper pairing in these materials.

7.1.2 Deeper analysis of the superconducting state

So far we laid out the answer to question (i), namely that it is indeed possible to obtain unconventional superconducting states from isotropic electron-phonon interaction in several classes of superconductors. We now want to examine closer why this happens, and in particular what the cause of a sign-changing gap function is.

We start the analysis by writing the electron self-energy of Eq. (6.9) in a slightly modified way,

$$\begin{aligned}\hat{\Sigma}_k =& T\sum_{k_1} V_{k-k_1}\hat{\rho}_3\hat{G}_{k_1}\hat{\rho}_3\Big(1+T\sum_{k_2} V_{k_1-k_2}\hat{G}_{k_2}\hat{\rho}_3\hat{G}_{k_2-k_1+k}\hat{\rho}_3\Big)\\ =& T\sum_{k_1} V_{k-k_1}\hat{\rho}_3\hat{G}_{k_1}\hat{\rho}_3\Big(1+g_0^2\hat{\Gamma}_{k,k_1}\Big),\end{aligned} \tag{7.5}$$

where we implicitly defined the electron-phonon vertex

$$\hat{\Gamma}_{k,k_1} = \frac{T}{g_0^2}\sum_{k_2} V_{k_1-k_2}\hat{G}_{k_2}\hat{\rho}_3\hat{G}_{k_2-k_1+k}\hat{\rho}_3\ . \tag{7.6}$$

Written as in Eq. (7.5) it becomes apparent that we can easily recover the self-energy of ‘standard’ Eliashberg theory by setting $\hat{\Gamma}_{k,k_1}$ to zero. Moving forward, we can explicitly perform the matrix multiplications in Nambu space in the definition of the vertex, leading to

$$\begin{aligned}\hat{\Gamma}_{k,k_1} = \frac{T}{g_0^2}\sum_{k_2} V_{k_1-k_2}\big(- \underline{\gamma^{(Z)}_{k_2}\gamma^{(Z)}_{k_2-k_1+k}\hat{\rho}_0} + i\gamma^{(\chi)}_{k_2}\gamma^{(Z)}_{k_2-k_1+k}\hat{\rho}_3 + i\gamma^{(\phi)}_{k_2}\gamma^{(Z)}_{k_2-k_1+k}\hat{\rho}_1 \\ + i\gamma^{(Z)}_{k_2}\gamma^{(\chi)}_{k_2-k_1+k}\hat{\rho}_3 + \underline{\gamma^{(\chi)}_{k_2}\gamma^{(\chi)}_{k_2-k_1+k}\hat{\rho}_0} - i\gamma^{(\phi)}_{k_2}\gamma^{(\chi)}_{k_2-k_1+k}\hat{\rho}_2 \\ - \gamma^{(Z)}_{k_2}\gamma^{(\phi)}_{k_2-k_1+k}\hat{\rho}_1 - i\gamma^{(\chi)}_{k_2}\gamma^{(\phi)}_{k_2-k_1+k}\hat{\rho}_2 - \underline{\gamma^{(\phi)}_{k_2}\gamma^{(\phi)}_{k_2-k_1+k}\hat{\rho}_0}\big),\end{aligned} \tag{7.7}$$

where we inserted the electron Green’s function of Eq. (6.6) twice into Eq. (7.6). From the properties of the Pauli basis it follows that all prefactors of $\hat{\rho}_0$, which are underlined in Eq. (7.7) for clarity, enter each function Z, χ and ϕ[1]. It is therefore useful to estimate the influence of the second order Feynman diagram by the (scalar) function

$$\Gamma_{k,k_1} = -\frac{T}{g_0^2}\sum_{k_2} V_{k_1-k_2}\big(\gamma^{(Z)}_{k_2}\gamma^{(Z)}_{k_2-k_1+k} - \gamma^{(\chi)}_{k_2}\gamma^{(\chi)}_{k_2-k_1+k} + \gamma^{(\phi)}_{k_2}\gamma^{(\phi)}_{k_2-k_1+k}\big). \tag{7.8}$$

We assume isotropic electron-phonon interaction, therefore the coupling has only Matsubara frequency dependence, $V_{k_1-k_2} \equiv V_{m_1-m_2}$. In this case, by defining $\mathbf{q} = \mathbf{k} - \mathbf{k}_1$, we only have to deal with a single momentum index in the vertex estimate. For simplicity, we further set $m = m_1$ and write the momentum and frequency dependencies explicitly:

$$\Gamma_{\mathbf{q},m} = -\frac{T}{g_0^2}\sum_{\mathbf{k}_2,m_2} V_{m-m_2}\big(\gamma^{(Z)}_{\mathbf{k}_2,m_2}\gamma^{(Z)}_{\mathbf{k}_2+\mathbf{q},m_2} - \gamma^{(\chi)}_{\mathbf{k}_2,m_2}\gamma^{(\chi)}_{\mathbf{k}_2+\mathbf{q},m_2} + \gamma^{(\phi)}_{\mathbf{k}_2,m_2}\gamma^{(\phi)}_{\mathbf{k}_2+\mathbf{q},m_2}\big). \tag{7.9}$$

There are cases in which it is advantageous to get an estimate of $\Gamma_{\mathbf{q},m}$ without having to self-consistently solve the vertex-corrected Eliashberg equations. An often reasonable estimate can be found by considering the non-interacting state, in which $Z = 1$, $\chi = 0$ and $\phi = 0$. With the shorthand notation[2] $\gamma^{(\omega)}_{\mathbf{k},m} = \omega_m/[(i\omega_m)^2 - \xi^2_{\mathbf{k}}]$ and $\gamma^{(\xi)}_{\mathbf{k},m} = \xi_{\mathbf{k}}/[(i\omega_m)^2 - \xi^2_{\mathbf{k}}]$ we find

$$\Gamma^{(0)}_{\mathbf{q},m} = -\frac{T}{g_0^2}\sum_{\mathbf{k}_2,m_2} V_{m-m_2}\big(\gamma^{(\omega)}_{\mathbf{k}_2,m_2}\gamma^{(\omega)}_{\mathbf{k}_2+\mathbf{q},m_2} - \gamma^{(\xi)}_{\mathbf{k}_2,m_2}\gamma^{(\xi)}_{\mathbf{k}_2+\mathbf{q},m_2}\big) \tag{7.10}$$

---

[1] Recall, that we project out a function in channel i by calculating $\mathrm{Tr}(\hat{\Sigma}\hat{\rho}_i) \sim \mathrm{Tr}(\hat{\rho}_3\hat{G}\hat{\rho}_3(1+\hat{\Gamma})\hat{\rho}_i)$. Those terms of $\hat{\Gamma}$ proportional to $\hat{\rho}_0$ leave the projection matrix $\hat{\rho}_i$ invariant, and therefore enter the result regardless of the choice i.

[2] In the case of multiple electron energy bands, $\xi_{\mathbf{k},n}$, we define $\gamma^{(\omega)}_{\mathbf{k},m} = \sum_n \omega_m/[(i\omega_m)^2 - \xi^2_{\mathbf{k},n}]$, $\gamma^{(\xi)}_{\mathbf{k},m} = \sum_n \xi_{\mathbf{k},n}/[(i\omega_m)^2 - \xi^2_{\mathbf{k},n}]$.

as approximation to the vertex estimate. The Matsubara frequency sum in Eq. (7.10) can be performed analytically but we omit to write the result here explicitly as it is rather lengthy and does not contribute much to the narrative.

The functional form of the vertex bears a striking similarity to the electron susceptibility that we encountered in earlier Chapters. In the fully interacting state, the susceptibility can be calculated as

$$\begin{aligned} \mathrm{X}_{\mathbf{q},l} &= T \sum_{\mathbf{k},m} \mathrm{Tr}\big[\hat{\rho}_3 \hat{G}_{\mathbf{k},m} \hat{\rho}_3 \hat{G}_{\mathbf{k}+\mathbf{q},m+l}\big] \\ &= -2T \sum_{\mathbf{k},m} \big(\gamma^{(Z)}_{\mathbf{k},m}\gamma^{(Z)}_{\mathbf{k}+\mathbf{q},m+l} - \gamma^{(\chi)}_{\mathbf{k},m}\gamma^{(\chi)}_{\mathbf{k}+\mathbf{q},m+l} + \gamma^{(\phi)}_{\mathbf{k},m}\gamma^{(\phi)}_{\mathbf{k}+\mathbf{q},m+l}\big), \end{aligned} \tag{7.11}$$

which resembles Eq. (7.9) up to a prefactor and the electron-phonon coupling. In the non-interacting state we find

$$\mathrm{X}^{(0)}_{\mathbf{q},l} = -2T \sum_{\mathbf{k},m} \big(\gamma^{(\omega)}_{\mathbf{k},m}\gamma^{(\omega)}_{\mathbf{k}+\mathbf{q},m+l} - \gamma^{(\xi)}_{\mathbf{k},m}\gamma^{(\xi)}_{\mathbf{k}+\mathbf{q},m+l}\big), \tag{7.12}$$

which is the close cousin of Eq. (7.10). What we learn here is that the vertex correction to the electron-phonon problem should behave approximately as the susceptibility of the system, which means that Fermi surface nesting is the most likely candidate for mediating a sign change in the renormalized interaction, and therefore in the superconducting order parameter.

Let us now consider again the three systems discussed in Section 7.1.1. For each case we show the outcome of Eqs. (7.9) and (7.10) for $m = 0$ by plotting the vertex functions in the first two rows of Fig. 7.4. Since we consider isotropic electron-phonon couplings, these functions $(1 + g_0^2\Gamma_{\mathbf{q},0})$ and $(1 + g_0^2\Gamma^{(0)}_{\mathbf{q},0})$ contain the full momentum dependence of the renormalized interaction. We observe in panels (a-c) that this interaction is attractive in most parts of the Brillouin zone, while having a negative sign close to the respective nesting wave vector **Q**. It is therefore straight-forward to conclude that the sign change of the order parameter, see Fig. 7.2, is caused by the momentum dependence of the renormalized vertex function. Further, for the Cu-based and Fe-based systems the similarity between results from the interacting and non-interacting state are striking, compare panels (a-b) with (d-e) in Fig. 7.4. For our example of heavy fermion superconductors, however, there are significant differences in that no sign change of the vertex function is found in the non-interacting state, see Fig 7.4(c) and (f). This means that in some (but not all) cases it might not be necessary to self-consistently solve the vertex-corrected Eliashberg equations for getting an accurate estimate of the renormalized vertex function.

When comparing the first and second with the third and fourth row in Fig. 7.4, we immediately realize how similar the Brillouin zone structures of susceptibilities and vertex functions are. Even though the former does not change sign as function of **q**, the shape matches that of the vertex function. Results in the interacting state, panels (a-c) and (g-i), compare equally accurate for each system as those obtained for the non-interacting systems, panels (d-f) and (j-l). This clearly points towards the utter importance of coherent nesting conditions for determining the Brillouin zone structure of the vertex function, as this is the well-known dominant factor entering the susceptibilities [13]. We therefore have substantial reason to conclude that nesting conditions are

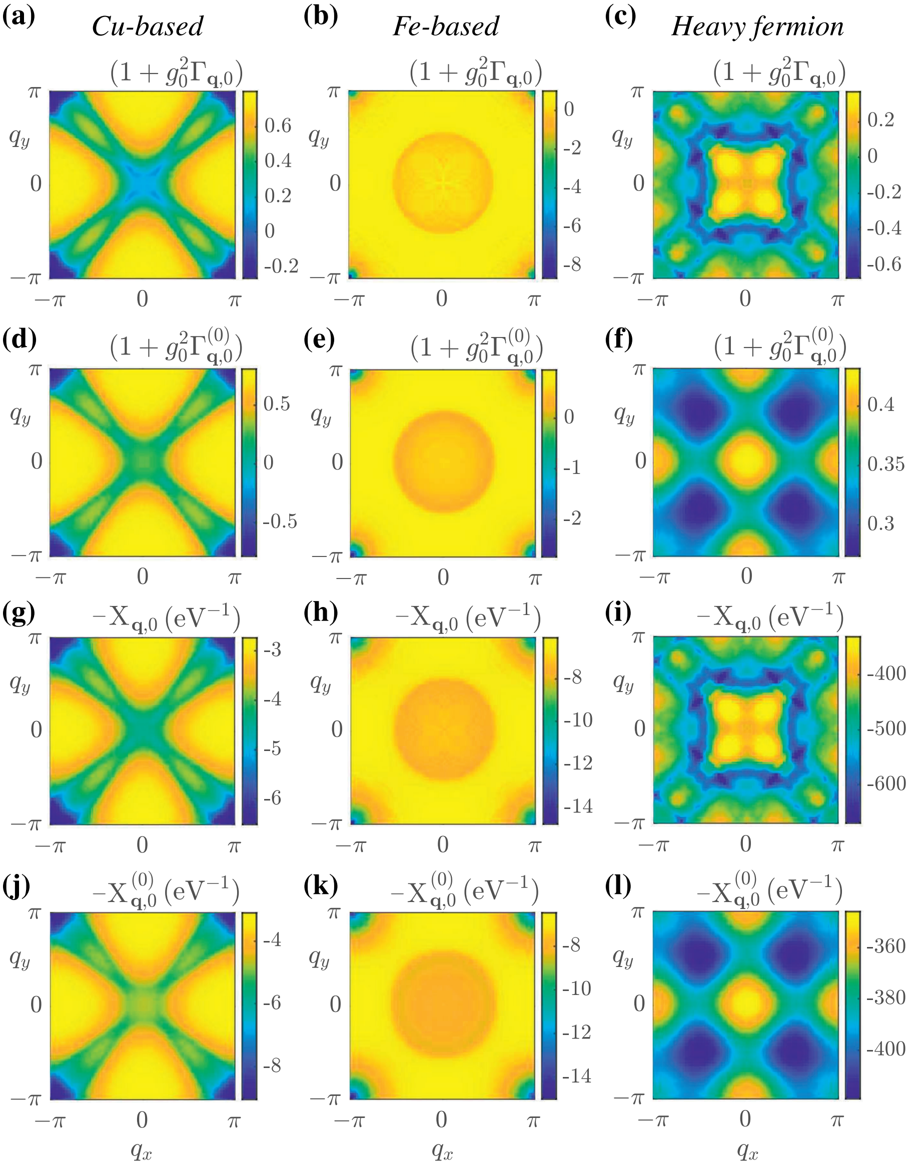

Figure 7.4. Zero-frequency (bare) vertex functions and (bare) susceptibilities, see label in each panel. The first, second and third columns correspond to results for the Cu-based, Fe-based and heavy fermion superconductor, respectively. Parts of the figure are taken from Paper XI.

the driving force for both spin fluctuations and electron-phonon mediated pairing in the families of unconventional superconductors considered here.

It is important to stress what these results precisely mean. Using only *isotropic* electron-phonon interaction in a vertex-corrected Eliashberg framework leads automatically to the experimentally observed, *unconventional* symmetries of the superconducting gap function. This confirms earlier results obtained by Hague for the Cu-based compounds [140], and even generalizes the picture to a much broader set of superconductors, which is the answer to question (i) posed in the beginning of the current Section. Concerning question (ii), we found that the unconventional superconducting gap symmetry appears as consequence of coherent Fermi surface nesting, and therefore is expected to be at least as generic as the concept of spin fluctuations. We do not claim to fully have solved the theoretical challenges concerning unconventional superconductivity, nor does the concept of spin fluctuations become irrelevant. However, the findings introduce a paradigm shift, in that electron-phonon and spin fluctuations interactions do not necessarily support different symmetries of the superconductivity order parameter, as is generally believed, but rather are possibly cooperating to boost T_c in high temperature superconductors. As an explicit example, we explore in Section 7.2 a real system in which the here presented effects are likely of importance to explain the superconducting state.

7.2 The case of ThFeAsN

Here we want to look into a real physical system, considered in Paper XII, where vertex corrections to the electron-phonon problem might play a crucial role for explaining superconductivity. ThFeAsN is a recently discovered, undoped superconductor with critical temperature $T_c^{\text{exp}} = 30\,\text{K}$ [164]. We wanted to see if superconductivity in this material can be understood by adiabatic, Fermi surface averaged Eliashberg theory for electron-phonon and spin/charge interactions, which takes results from *ab initio* calculations for the electron energies $\xi_{\mathbf{k},n}$ and electron-phonon couplings $\lambda_{\mathbf{q},\nu}$ as input. Here, n is an energy band index and ν denotes the phonon branch. For calculating the electronic dispersion one needs to use the experimental lattice parameters to get the distance between Fe and As planes correctly [165, 166], a common challenge in Fe-based superconductors that potentially can lead to wrong Fermi surface topologies [167, 168]. The Fermi surface of ThFeAsN is prototypical for the family of Fe-based superconductors, consisting of electron-like pockets at the Brillouin zone edges, and hole-like bands at the center, while being effectively two dimensional. As will become clear in the discussion below, the adiabatic theory cannot explain the high critical temperature in ThFeAsN, and we have good reason to believe that T_c will be enhanced upon the inclusion of vertex corrections to the electron-phonon interaction.

We calculate the dynamic electron-phonon couplings by using the *ab initio* inputs $\lambda_{\mathbf{q},\nu}$ and phonon frequencies $\omega_{\mathbf{q},\nu}$ as

$$\lambda^{(\mathrm{ep})}_{\mathbf{q},l} = \sum_{\nu} \lambda_{\mathbf{q},\nu} \frac{\omega^2_{\mathbf{q},\nu}}{\omega^2_{\mathbf{q},\nu} + q_l^2}. \tag{7.13}$$

The band-resolved electronic bare susceptibility is obtained via

$$X^{n,n'}_{\mathbf{q},l} = \sum_{\mathbf{k}} \delta(\xi_{\mathbf{k},n}) \delta(\xi_{\mathbf{k}+\mathbf{q},n'}) \frac{n_F(\xi_{\mathbf{k},n}) - n_F(\xi_{\mathbf{k}+\mathbf{q},n'})}{\xi_{\mathbf{k}+\mathbf{q},n'} - \xi_{\mathbf{k},n} + iq_l}, \tag{7.14}$$

with $n_F(\cdot)$ the Fermi-Dirac function. There are three hole bands and two electron bands crossing the Fermi level, which we group as sets h and e, respectively. We can then define susceptibilities that couple those two subsets of bands in different combinations:

$$X^{(e-e)}_{\mathbf{q},l} = \sum_{n\in e, n'\in e} X^{n,n'}_{\mathbf{q},l}, \tag{7.15a}$$

$$X^{(h-h)}_{\mathbf{q},l} = \sum_{n\in h, n'\in h} X^{n,n'}_{\mathbf{q},l}, \tag{7.15b}$$

$$X^{(e-h)}_{\mathbf{q},l} = \sum_{n\in e, n'\in h} X^{n,n'}_{\mathbf{q},l} + \sum_{n\in h, n'\in e} X^{n,n'}_{\mathbf{q},l}, \tag{7.15c}$$

$$X^{(0)}_{\mathbf{q},l} = X^{(e-e)}_{\mathbf{q},l} + X^{(h-h)}_{\mathbf{q},l} + X^{(e-h)}_{\mathbf{q},l} = \sum_{n,n'} X^{n,n'}_{\mathbf{q},l}. \tag{7.15d}$$

To be explicit, $X^{(e-h)}_{\mathbf{q},l}$ includes only the couplings between electron bands with hole bands, but neither electron, nor hole bands among each other. When using the index $r \in \{e-e, h-h, e-h, 0\}$, we can define the spin and charge fluctuations kernels within the Random Phase Approximation (RPA) as function of the Stoner interaction U,

$$\lambda^{(\mathrm{sf},r)}_{\mathbf{q},l} = \frac{3}{2} N(0) U^2 \frac{X^{(r)}_{\mathbf{q},l}}{1 - UX^{(r)}_{\mathbf{q},l}}, \tag{7.16a}$$

$$\lambda^{(\mathrm{cf},r)}_{\mathbf{q},l} = \frac{1}{2} N(0) U^2 \frac{X^{(r)}_{\mathbf{q},l}}{1 + UX^{(r)}_{\mathbf{q},l}}, \tag{7.16b}$$

valid for spin-singlet electrons. In Eqs. (7.16), $N(0)$ denotes the Fermi surface density of states. The Stoner criterion dictates that the system develops a magnetic instability when $1 - UX^{(r)}_{\mathbf{q},l} \to 0$, therefore U's upper bound is given by $U^{(r)}_{\max} = [\max_{\mathbf{q},l} X^{(r)}_{\mathbf{q},l}]^{-1}$. It is convenient to define the Stoner parameter in relation to this upper bound, i.e. $U = \frac{p}{100} U^{(r)}_{\max}$, where $p \in (0, 100)$.

The momentum structure of each of the above couplings is crucially important when in comes to the superconducting state. For this reason we examine the outcomes of Eqs. (7.13) and (7.16) in Fig. 7.5 closer. The results have been calculated by considering the system as two dimensional. Panels (a) and (b), representing the coupling of electron with electron bands, and hole with hole bands, respectively, show clearly dominant contributions around the Brillouin zone center, which are expected to suppress superconductivity [169]. The situation is different in Fig. 7.5(c), where we plot the spin fluctuations interaction due to a coupling only between electron and hole bands. In this scenario the result is strongly peaked at large wave vectors, which is the ingredient needed to induce a sign change of the superconducting gap on the Fermi surface. Combining all the contributions to the spin fluctuations interaction leads to Fig. 7.5(d), where the dominant feature stems from $\lambda_{\mathbf{q},l}^{(\mathrm{sf},e-h)}$, but a noticeable hump around the Brillouin zone center remains.

The electron-phonon interaction, as it is shown in Fig. 7.5(e), is peaked at small and large momenta, a feature that is generally not expected to support the unconventional $s_{\pm}$-wave symmetry. For this particular state one would need a strongly peaked interaction at small-$\mathbf{q}$ [170]. To put these speculations to the test, we solved the Fermi surface restricted Eliashberg equations [171]

$$Z_{\mathbf{k},m}^{(r)} = 1 + \frac{\pi T}{\omega_m} \sum_{\mathbf{k}',m'} \frac{\delta(\xi_{\mathbf{k}'})}{N(0)} \lambda_{\mathbf{k}-\mathbf{k}',m-m'}^{(+,r)} \frac{\omega_{m'}}{\sqrt{\omega_{m'}^2 + (\Delta_{\mathbf{k}',m'}^{(r)})^2}}, \tag{7.17a}$$

$$\Delta_{\mathbf{k},m}^{(r)} = \frac{\pi T}{Z_{\mathbf{k},m}^{(r)}} \sum_{\mathbf{k}',m'} \frac{\delta(\xi_{\mathbf{k}'})}{N(0)} \lambda_{\mathbf{k}-\mathbf{k}',m-m'}^{(-,r)} \frac{\Delta_{\mathbf{k}',m'}^{(r)}}{\sqrt{\omega_{m'}^2 + (\Delta_{\mathbf{k}',m'}^{(r)})^2}}, \tag{7.17b}$$

with the couplings $\lambda_{\mathbf{q},l}^{(\pm,r)} = \pm\lambda_{\mathbf{q},l}^{(\mathrm{sf},r)}(+\lambda_{\mathbf{q},l}^{(\mathrm{cf},r)})(+\lambda_{\mathbf{q},l}^{(\mathrm{ep})})$, where we tested all possibilities of combining spin, charge and electron-phonon couplings.

As an example, we show the self-consistent solution of the superconducting gap for $r = e-h$, $T = 2\,\mathrm{K}$, $p = 99$ and $m = 0$ in Fig. 7.5(f). We observe that Δ changes sign between the electron and hole bands, as is typically the case in Fe-based superconductors [37, 162], and compatible with experiment in ThFeAsN [172]. However, the critical temperature for this particular parameter setting is only about 5 K, which is considerably smaller than $T_c^{\exp}$. Naively, one would expect that we can achieve drastically higher values for T_c by increasing U, since this has the effect of larger coupling strengths. However, as was also shown in Paper II and Section 3.2, the critical temperature cannot arbitrarily be enhanced by choosing U close to $U_{\max}$.

As mentioned before, we tested all possible interaction kernels $\lambda_{\mathbf{q},l}^{(\pm,r)}$, i.e. each combination of electron-phonon and spin/charge interactions. Here also all options concerning the coupling of hole and electron bands have been explored. The maximally allowed critical temperature as obtained in our Eliashberg formalism was $T_c \sim 7.5\,\mathrm{K}$, which is significantly deviating from the ex-

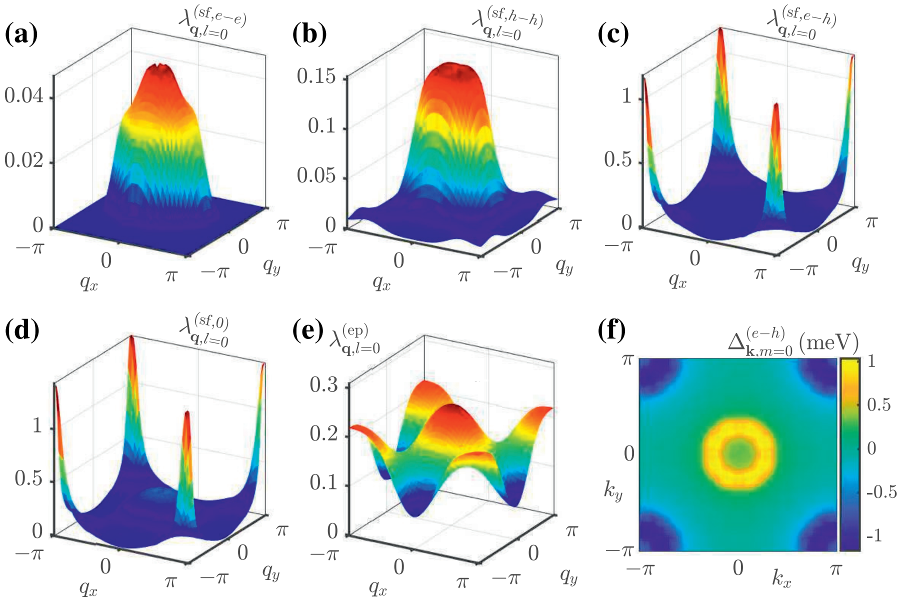

Figure 7.5. (a-d) Zero-frequency spin fluctuations interactions according to Eqs. (7.16), obtained for $U = 110\,\text{meV}$ and $T = 5\,\text{K}$. (e) Zero-frequency component of the electron-phonon interaction. (f) Self-consistently calculated superconducting gap function at $m = 0$, $p = 99$ and $T = 2\,\text{K}$. Figure taken from Paper XII.

perimental result. Our analysis showed that this is due to phase frustration effects, which means that the electron-phonon interaction and $\lambda^{(\text{sf/cf},r)}_{\mathbf{q},l}$ for $r \in \{e-e, h-h\}$ support a non-sign changing symmetry of the superconducting gap, while the dominant $\lambda^{(\text{sf},e-h)}_{\mathbf{q},l}$ promotes the correct $s_{\pm}$-wave symmetry. This self-restraint behavior is not unusual for Fe-based superconductors [169], and further work is required to overcome this issue. This is the point where we realized that vertex corrections to the electron-phonon interaction could be of utter importance in ThFeAsN.

The first thing to notice is that the adiabatic ratio, with characteristic phonon energy scale $\omega_{\log} \simeq 17\,\text{meV}$ and minimal band shallowness $\varepsilon_F \simeq 52\,\text{meV}$, is not substantially smaller than unity, $\alpha = \omega_{\log}/\varepsilon_F \sim 0.33$. This is a direct indicator that vertex corrections are likely important. To get an estimate of the renormaliazed vertex function we consider the non-interacting system and assume that the phonon spectrum can be approximated by a single optical phonon with frequency $\omega_{\log}$. The vertex $\Gamma^{(0)}_{\mathbf{q},m}$ can then be evaluated via Eq. (7.10). By following the approach of Ref. [173] for estimating the electron-phonon coupling strength via

$$\lambda = \frac{1.04 + \mu^{\star}\log(\Theta_D/1.45T_c)}{(1-0.62\mu^{\star})\log(\Theta_D/1.45T_c) - 1.04}, \tag{7.18}$$

we obtain a value of $\lambda = 1.6$, directly resembling the coupling strength in the actual physical system. In Eq. (7.18), we use $T_c = T_c^{\text{exp}} = 30\,\text{K}$ [164], a standard value for the Coulomb pseudopotential $\mu^\star = 0.136$, and the Debye temperature $\Theta_D = 332\,\text{K}$ [174]. With these parameters we calculate the scattering strength as $g_0 = \sqrt{\lambda\,\omega_{\log}/2N(0)}$.

In Fig. 7.6 we show the result for the renormalized vertex function, calculated at $T = 10\,\text{K}$. Now, in contrast to the non-renormalized interaction, the large wave vector couplings have a negative sign, while $(1+g_0^2\Gamma^{(0)})$ is positive in most parts of the Brillouin zone. This particular shape resembles our model calculations for Fe-based superconductors in Section 7.1, and therefore it is a clear indication that the electron-phonon interaction supports an $s_\pm$-wave symmetry of the superconducting gap when vertex corrections are taken into account. As a natural consequence, we expect that the frustration effects discussed earlier are minimized, while the critical temperature is boosted due to a cooperative effect from electron-phonon and spin fluctuations interactions.

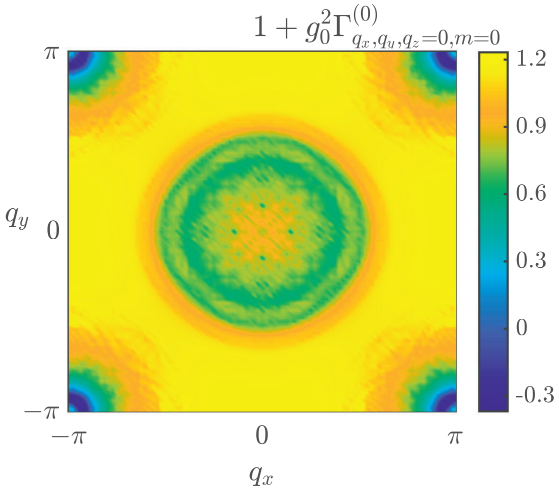

Figure 7.6. Estimate for the renormalized electron-phonon vertex function in ThFeAsN, calculated at $T = 10\,\text{K}$ and shown for $q_z = 0$, $m = 0$. The Figure is reprinted from Paper XII.

In summary, we have shown in Paper XII that the superconducting state in ThFeAsN cannot be explained by a Fermi surface restricted Eliashberg theory. At the current stage it is unclear whether our conclusions in this regard would change if we included the orbital dependence of the electron energy bands. However, we identified the system as a likely candidate for electron-phonon mediated, unconventional superconductivity, cooperating with the spin/charge fluctuations mechanism so as to produce the prototypical $s_\pm$-wave symmetry of the superconducting gap function and a high T_c.

7.3 Odd-frequency superconductivity

We now want to address another ‘exotic’ phenomenon that occurs due to vertex corrections to electron-phonon interaction, which is that of odd-frequency superconductivity. Until here we discussed even-parity Cooper pairs made of spin-singlet electrons, which are even functions under exchange of relative time. This means that the superconducting gap describing the condensate of such Cooper pairs is even in Matsubara and real frequency space. However, superconductivity is also possible for spin-triplet, odd-frequency electrons, still assuming even parity in real/momentum space [175]. The first proposal of such a state was introduced by Berezinskii [176] for superfluid ^{3}He. The concept of odd-frequency superconductivity is generally connected to either spin degrees of freedom [175] or strong electron-phonon interactions [177, 178] and it is often needed to tune the system or include many degrees of freedom for making the odd-frequency state stable against the even-frequency counterpart [179–182]. Odd-frequency superconductivity is therefore often discussed in terms of Cooper pair correlations [175]. Our focus here is different, as we are looking for a macroscopic odd-frequency phase with finite order parameter.

Here we summarize the results from Paper XIII, in which we show that, under the assumption of even parity, a moderate isotropic electron-phonon interaction within vertex-corrected Eliashberg theory leads to a coexistence of the ‘standard’ spin-singlet, even-frequency gap and a spin-triplet, odd-frequency state. After introducing an extended version of Eliashberg equations in Section 7.3.1, we benchmark our theoretical findings in Section 7.3.2, using a standard cuprate model similar to that of Section 7.1.

7.3.1 Further theoretical extension

The reason why we considered odd-frequency pairing in the first place was a simple observation: Recall that the very definition of the electron self-energy in Eq. (6.3) has no contribution in the Pauli matrix channel $\hat{\rho}_2$. On the other hand we know that we can express $\hat{\Sigma} = \hat{\Sigma}^{(1)} + \hat{\Sigma}^{(2)}$ according to the two Feynman diagrams we include in our theory. It is well known that the first order term leads to $\mathrm{Tr}[\hat{\rho}_2\hat{\Sigma}^{(1)}] = 0$, which represents the gauge freedom of the system. However, when taking into account the contributions of second order in the electron-phonon coupling, we find

$$\frac{1}{2}\mathrm{Tr}[\hat{\rho}_2\hat{\Sigma}^{(2)}_k] = T^2 \sum_{k_1,k_2} V_{k-k_1}V_{k_1-k_2}\Big[-\big(\gamma^{(\chi)}_{k_1}\gamma^{(\phi)}_{k_2} + \gamma^{(\phi)}_{k_1}\gamma^{(\chi)}_{k_2}\big)\gamma^{(Z)}_{k_2-k_1+k} \\ +\big(\gamma^{(Z)}_{k_1}\gamma^{(\phi)}_{k_2} - \gamma^{(\phi)}_{k_1}\gamma^{(Z)}_{k_2}\big)\gamma^{(\chi)}_{k_2-k_1+k} + \big(\gamma^{(Z)}_{k_1}\gamma^{(\chi)}_{k_2} + \gamma^{(\chi)}_{k_1}\gamma^{(Z)}_{k_2}\big)\gamma^{(\phi)}_{k_2-k_1+k}\Big], \quad (7.19)$$

which does not vanish in general. Due to the combination of Pauli matrices and electron Green’s functions in Eq. (6.9) the above terms are induced in the

$\hat{\rho}_2$ channel. We therefore define the order parameter $\zeta_k^{\mathrm{ind}} = \frac{1}{2}\mathrm{Tr}[\hat{\rho}_2 \hat{\Sigma}_k^{(2)}]$, with label 'ind' for induced. Note, that each summand in Eq. (7.19) has one factor $\gamma^{(\phi)}$, which is why $\zeta_k^{\mathrm{ind}} = 0$ in the normal state, and we can associate this function with superconductivity.

It is worthwhile examining the frequency symmetry of ζ_k^{ind}. To do so we focus for the moment only on the Matsubara frequency axis. Each term inside the large brackets of Eq. (7.19) is a product of $\gamma^{(Z)}$, $\gamma^{(\chi)}$ and $\gamma^{(\phi)}$, containing each factor exactly once. Let us therefore perform the analysis with a representative example

$$\beta_m = \sum_{m_1,m_2} V_{m-m_1} V_{m_1-m_2} \gamma^{(Z)}_{m_1} \gamma^{(\chi)}_{m_2} \gamma^{(\phi)}_{m_2-m_1+m}. \tag{7.20}$$

The above function β_m has fermionic Matsubara frequency dependence, therefore we can invert the index by considering β_{-m-1}. Insertion into Eq. (7.20) leads to factors V_{-m-m_1-1} and $\gamma^{(\phi)}_{m_2-m_1-m-1}$. Next, we change the summation variable to $\tilde{m}_1 = -m_1 - 1$, which is possible due to the fact that we need to sum over all integers:

$$\beta_{-m-1} = \sum_{\tilde{m}_1,m_2} V_{-m+\tilde{m}_1} V_{-\tilde{m}_1-m_2-1} \gamma^{(Z)}_{-\tilde{m}_1-1} \gamma^{(\chi)}_{m_2} \gamma^{(\phi)}_{m_2+\tilde{m}_1-m}. \tag{7.21}$$

Equivalently, we treat the second summation index as $\tilde{m}_2 = -m_2 - 1$, leading to

$$\beta_{-m-1} = \sum_{\tilde{m}_1,\tilde{m}_2} V_{-m+\tilde{m}_1} V_{-\tilde{m}_1+\tilde{m}_2} \gamma^{(Z)}_{-\tilde{m}_1-1} \gamma^{(\chi)}_{-\tilde{m}_2-1} \gamma^{(\phi)}_{-\tilde{m}_2+\tilde{m}_1-m-1}. \tag{7.22}$$

We know that the electron-phonon coupling has even bosonic symmetry, $V_l = V_{-l}$, while the remaining functions obey $\gamma^{(Z)}_{-m-1} = -\gamma^{(Z)}_m$, $\gamma^{(\chi)}_{-m-1} = \gamma^{(\chi)}_m$ and $\gamma^{(\phi)}_{-m-1} = \gamma^{(\phi)}_m$, compare Eq. (6.5). Using these relations in Eq. (7.22) gives

$$\beta_{-m-1} = -\sum_{\tilde{m}_1,\tilde{m}_2} V_{m-\tilde{m}_1} V_{\tilde{m}_1-\tilde{m}_2} \gamma^{(Z)}_{\tilde{m}_1} \gamma^{(\chi)}_{\tilde{m}_2} \gamma^{(\phi)}_{\tilde{m}_2-\tilde{m}_1+m} = -\beta_m. \tag{7.23}$$

We have therefore proven that each term in Eq. (7.19) is odd along the Matsubara frequency axis, which makes also ζ_k^{ind} an odd function. In the case of even parity and within the single band picture adopted here, this means that the induced order parameter describes spin-triplet electrons [175], which coexist with even-frequency spin-singlet Cooper pairs represented by ϕ.

So far we have characterized the induced order parameter, but it further needs to be shown that the renormalized interaction can indeed support such a state, i.e. that both even- and odd-frequency superconducting gaps can be finite simultaneously. To achieve this, we need to extend the vertex-corrected Eliashberg theory used until here, so as to include a self-consistent equation for the newly discovered order parameter. The first step is to include the symmetry channel $\hat{\rho}_2$ in the definition of the electron self-energy,

$$\hat{\Sigma}_k = i\omega_k(1-Z_k)\hat{\rho}_0 + \chi_k\hat{\rho}_3 + \phi_k\hat{\rho}_1 + \zeta_k\hat{\rho}_2, \tag{7.24}$$

leading to the Green's function

$$\hat{G}_k = i\gamma_k^{(Z)}\hat{\rho}_0 + \gamma_k^{(\chi)}\hat{\rho}_3 + \gamma_k^{(\phi)}\hat{\rho}_1 + \gamma_k^{(\zeta)}\hat{\rho}_2, \tag{7.25}$$

$$\Theta_k = [i\omega_k Z_k]^2 - [\xi_k + \chi_k]^2 - \phi_k^2 - \zeta_k^2, \tag{7.26}$$

with the definition $\gamma_k^{(\zeta)} = \zeta_k/\Theta_k$. Here we dropped the label 'ind' to stress that we are now dealing with the self-consistent version of the odd-frequency function. The standard recipe of deriving the Eliashberg equations, compare Sections 2.1 and 6.1, yields

$$Z_k = 1 - \frac{T}{\omega_k}\sum_{k_1} V_{k-k_1}\Big(\gamma_{k_1}^{(Z)} + T\sum_{k_2} V_{k_1-k_2}\vec{\gamma}_{k_2}^T Q_{k_1}^{(Z)}\vec{\gamma}_{k_2-k_1+k}\Big), \tag{7.27a}$$

$$\chi_k = T\sum_{k_1} V_{k-k_1}\Big(\gamma_{k_1}^{(\chi)} + T\sum_{k_2} V_{k_1-k_2}\vec{\gamma}_{k_2}^T Q_{k_1}^{(\chi)}\vec{\gamma}_{k_2-k_1+k}\Big), \tag{7.27b}$$

$$\phi_k = -T\sum_{k_1} V_{k-k_1}\Big(\gamma_{k_1}^{(\phi)} + T\sum_{k_2} V_{k_1-k_2}\vec{\gamma}_{k_2}^T Q_{k_1}^{(\phi)}\vec{\gamma}_{k_2-k_1+k}\Big), \tag{7.27c}$$

$$\zeta_k = -T\sum_{k_1} V_{k-k_1}\Big(\gamma_{k_1}^{(\zeta)} + T\sum_{k_2} V_{k_1-k_2}\vec{\gamma}_{k_2}^T Q_{k_1}^{(\zeta)}\vec{\gamma}_{k_2-k_1+k}\Big), \tag{7.27d}$$

where we now use four-component vectors $\vec{\gamma}_k^T = (\gamma_k^{(Z)}, \gamma_k^{(\chi)}, \gamma_k^{(\phi)}, \gamma_k^{(\zeta)})$. The 4×4 pseudo matrices are defined as

$$Q_k^{(Z)} = \begin{pmatrix} -\gamma_k^{(Z)} & \gamma_k^{(\chi)} & \gamma_k^{(\phi)} & \gamma_k^{(\zeta)} \\ \gamma_k^{(\chi)} & \gamma_k^{(Z)} & \gamma_k^{(\zeta)} & -\gamma_k^{(\phi)} \\ -\gamma_k^{(\phi)} & \gamma_k^{(\zeta)} & -\gamma_k^{(Z)} & -\gamma_k^{(\chi)} \\ -\gamma_k^{(\zeta)} & -\gamma_k^{(\phi)} & \gamma_k^{(\chi)} & -\gamma_k^{(Z)} \end{pmatrix}, \quad Q_k^{(\chi)} = \begin{pmatrix} -\gamma_k^{(\chi)} & -\gamma_k^{(Z)} & \gamma_k^{(\zeta)} & -\gamma_k^{(\phi)} \\ -\gamma_k^{(Z)} & \gamma_k^{(\chi)} & -\gamma_k^{(\phi)} & -\gamma_k^{(\zeta)} \\ -\gamma_k^{(\zeta)} & -\gamma_k^{(\phi)} & -\gamma_k^{(\chi)} & \gamma_k^{(Z)} \\ \gamma_k^{(\phi)} & -\gamma_k^{(\zeta)} & -\gamma_k^{(Z)} & -\gamma_k^{(\chi)} \end{pmatrix},$$

$$Q_k^{(\phi)} = \begin{pmatrix} -\gamma_k^{(\phi)} & -\gamma_k^{(\zeta)} & -\gamma_k^{(Z)} & \gamma_k^{(\chi)} \\ -\gamma_k^{(\zeta)} & \gamma_k^{(\phi)} & \gamma_k^{(\chi)} & \gamma_k^{(Z)} \\ \gamma_k^{(Z)} & \gamma_k^{(\chi)} & -\gamma_k^{(\phi)} & \gamma_k^{(\zeta)} \\ -\gamma_k^{(\chi)} & \gamma_k^{(Z)} & -\gamma_k^{(\zeta)} & -\gamma_k^{(\phi)} \end{pmatrix}, \quad Q_k^{(\zeta)} = \begin{pmatrix} -\gamma_k^{(\zeta)} & \gamma_k^{(\phi)} & -\gamma_k^{(\chi)} & -\gamma_k^{(Z)} \\ \gamma_k^{(\phi)} & \gamma_k^{(\zeta)} & -\gamma_k^{(Z)} & \gamma_k^{(\chi)} \\ \gamma_k^{(\chi)} & -\gamma_k^{(Z)} & -\gamma_k^{(\zeta)} & -\gamma_k^{(\phi)} \\ \gamma_k^{(Z)} & \gamma_k^{(\chi)} & \gamma_k^{(\phi)} & -\gamma_k^{(\zeta)} \end{pmatrix}. \tag{7.28}$$

As a crosscheck, in the case of $\zeta_k \equiv 0$ we get $\gamma_k^{(\zeta)} = 0$. Taking the upper left 3×3 submatrices of each $Q_k^{(\cdot)}$ leaves us with each respective $P_k^{(\cdot)}$ from Section 6.1, compare Eq. (6.12), and we therefore recover the earlier used set of Eliashberg equations. In the following Section 7.3.2 we test the just introduced formalism in a common model for Cu-based superconductors, and show that ζ_k is a robust and finite order parameter for odd-frequency superconductivity.

7.3.2 Odd-frequency state in a cuprate superconductor

We use a similar next-nearest neighbor tight-binding description as in Section 7.1.1, namely

$$\xi_{\mathbf{k}} = -t^{(1)}\left[\cos(k_x)+\cos(k_y)\right] - t^{(2)}\cos(k_x)\cos(k_y) - \mu, \qquad (7.29)$$

where we now choose the hopping energies as $t^{(1)} = 0.25\,\mathrm{eV}$ and $t^{(2)} = -0.1\,\mathrm{eV}$. The choice of chemical potential $\mu = -0.09\,\mathrm{eV}$ renders the standard Fermi surface for Cu-based superconductors, compare Fig. 7.8. With an optical phonon mode at $\Omega = 50\,\mathrm{meV}$ and an electron-phonon scattering strength of $g_0 = 150\,\mathrm{meV}$, we solve the three vertex-corrected Eliashberg Eqs. (6.11) at $T = 60\,\mathrm{K}$. Note, that in this calculation we do not include the odd-frequency order parameter self-consistently. The results for Z_k, χ_k and ϕ_k are used to calculate the induced state via Eq. (7.19). In agreement to our analysis in Section 7.3.1, we find ζ_k^{ind} to be odd along the Matsubara frequency axis. The outcomes for index $m = -1$ are shown in Fig. 7.7.

The mass renormalization function Z in Fig. 7.7(a) shows a rather strongly developed anisotropy throughout the Brillouin zone, with maximum values around 1.7 and a minimum slightly smaller than unity. The Fermi surface in the interacting state is defined by the condition

$$(\xi_{\mathbf{k}} + \chi_{\mathbf{k},m=0})/Z_{\mathbf{k},m=0} = 0, \qquad (7.30)$$

from which we get a Fermi surface projected value of ~ 1.0003 for the mass renormalization. This result is strikingly close to unity, usually indicating a weak-coupling situation. The chemical potential renormalization χ has an

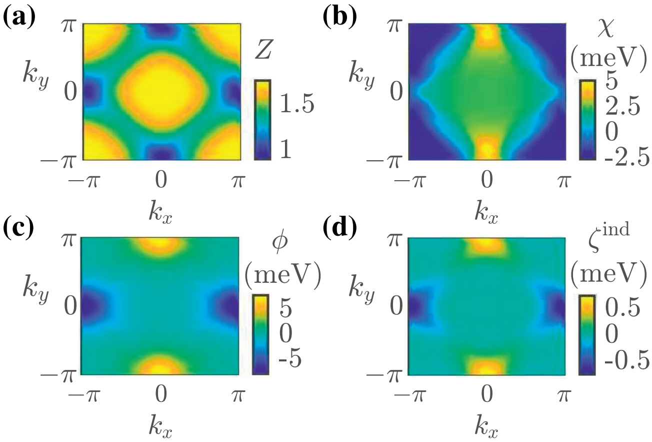

Figure 7.7. (a-c) Self-consistent zero-frequency results of Eqs. (6.11). (d) Induced order parameter ζ^{ind} at $m = -1$, calculated from Eq. (7.19). The Figure was taken from Paper XIII.

overall d-wave symmetry, which is shifted along the energy axis. This particular phenomenon is known as nematicity, which breaks the tetragonal C_4 symmetry to C_2. It needs to be stressed here that all inputs to the Eliashberg calculations are C_4 invariant, hence the symmetry breaking happens spontaneously in the self-consistent solution. For the current system parameters, χ is the only nematic function, but this can potentially change with the doping level, see Paper XI.

The even-frequency superconducting order parameter ϕ, shown in Fig. 7.7(c), has d-wave symmetry, similar to results in Section 7.1, with a maximum gap size of around 6 meV. We calculate the induced odd-frequency function ζ^{ind} from Eq. (7.19), i.e. not self-consistently at the moment. As directly apparent, the $m = -1$ component of ζ^{ind} has the same symmetry as ϕ, see Fig. 7.7(d). However, since we are dealing with an odd function in Matsubara space, the symmetry of the $m = 0$ component of ζ^{ind} differs to that of the $m = 0$ component of ϕ by a phase factor of -1. Further we note that the odd-frequency order parameter is approximately one order of magnitude smaller than its even-frequency counterpart, hence the latter is dominant. As we show in Paper XIII, but won't discuss in detail here, ζ^{ind} is non-vanishing due to a mixing of momentum space representations in Eq. (7.19).

Next, we want to compare results of one-shot and self-consistent calculations. To do so we solved the four coupled Eqs. (7.27) for the same set of input parameters as above, leading to the odd-frequency order parameter ζ_k. In Fig. 7.8(a) and (b) we plot the Fermi surface projection of ζ^{ind} and ζ, respectively, for Matsubara frequency index $m = -1$. No significant difference is detectable between the two solutions, and this similarly holds true for the entire frequency range and changing temperatures. The remaining functions Z, χ and ϕ are qualitatively not affected by a self-consistent inclusion of ζ_k. Therefore we are led to the conclusion that at least in some systems there is no need of solving the extended version of the vertex-corrected Eliashberg equations, but a single-shot calculation of the induced odd-frequency order parameter is sufficient. This is an advantage computationally speaking, as it is more costly to solve Eqs. (7.27) than Eqs. (6.11) due to an increased number of iterations and numerical steps in each cycle. Whether the similarity between ζ_k and ζ_k^{ind} is inherently generic needs further investigation.

As a commonly examined characteristic of a superconductor we use the T-dependence of the gap function $\Delta_k = \phi_k/Z_k$. The blue circles in Fig. 7.8(c) represent our numerical results for $\Delta = \max \Delta_{\mathbf{k},m=-1}$, obtained from the fully self-consistent formalism in Eq. (7.27). We fit the functional dependence via

$$\Delta(T) = \mathrm{Re}\sqrt{a - b \cdot T^c}, \tag{7.31}$$

where a, b and c are fitting parameters. It is clear from the solid blue line that the functional form of Eq. (7.31) matches our data points very accurately. It is useful to define the analogue of Δ for the induced odd-frequency state, which we name $\eta_k = \zeta_k/Z_k$. Following the temperature evolution of $\eta =$

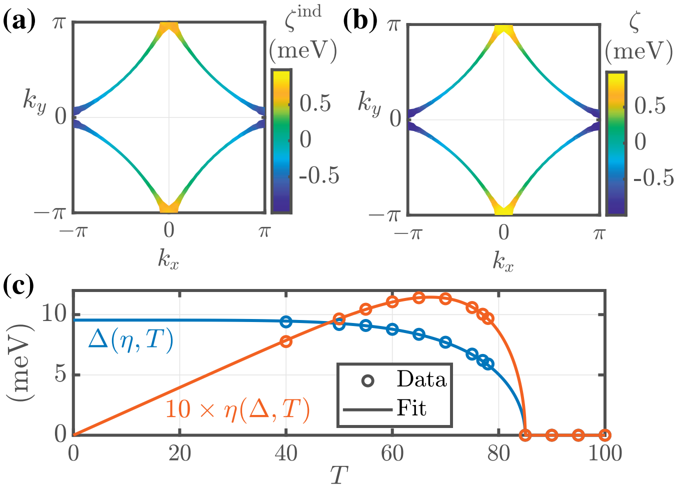

Figure 7.8. (a), (b) Frequency component $m = -1$ of the odd-frequency order parameter, projected on the Fermi surface. ζ^{ind} is obtained from a 'one-shot' calculation, ζ is the self-consistent solution. (c) Even-frequency (blue) and odd-frequency (red) superconducting gaps as functions of temperature. Figure taken from Paper XIII.

max $\eta_{\mathbf{k},m=-1}$ leads to the red open circles in Fig. 7.8(c), where we multiplied our results by a factor 10. Here, the fitting function (red solid line) is given by

$$\eta(T) = T \mathrm{Re}\sqrt{a - b \cdot T^c}, \tag{7.32}$$

where a, b and c are again parameters of the fit. What we observe is that, indeed, η is one order of magnitude smaller than the dominant gap function Δ [178, 181]. Further, the odd-frequency order parameter vanishes for small temperatures and has its maximum value at around 70 K. This shape is consistent with prior works on odd-frequency states [183, 184]. Finally, it is obvious from Fig. 7.8(c) that both odd- and even-frequency functions share the same T_c, which can be understood from the fact that η (or equivalently ζ) is describing an induced state enabled by the even-frequency pair condensate. Further it is noteworthy that the here-obtained odd-frequency d-wave spin-triplet phase is distinct from the phase originally proposed by Berezinskii [176].

The work presented in Paper XIII unambiguously shows that vertex corrections to the electron-phonon interaction induce an odd-frequency superconducting state, coexisting with its even-frequency counterpart. We successfully benchmarked our theoretical advances with a commonly employed model for Cu-based superconductors. In a broader context, it might be possible to have the roles of even- and odd-frequency order parameters interchanged. This is to be expected whenever ϕ is used to describe odd-parity Cooper pairs; in such a case we would get a dominant spin-singlet odd-frequency state, coexisting with an induced spin-triplet even-frequency order parameter.

8. Conclusions and outlook

> *Wer wartet mit Besonnenheit, der wird belohnt zur rechten Zeit. (The one who waits with prudence will be rewarded at the right time.)*
>
> Till Lindemann

In this thesis we covered many different topics within the field of superconductivity. On various levels of approximation for the theoretical description of the electron-boson interacting state we discussed some of the most important families of superconductors, model systems and real materials.

For FeSe/STO we successively developed a material specific theory of superconductivity that takes into account electron-phonon interaction (EPI) and spin fluctuations on equal footing, while considering the full electronic energy bandwidth. Besides being able to explain the observed T_c, gap magnitude on the Fermi surface (FS) and electron band replica, we discussed the gap anisotropy and symmetrization techniques in ARPES measurements. Further we predicted a temperature independence of the FS and a second order replica band, which both were confirmed later. Our findings suggest that small-$\mathbf{q}$ EPI is the cause for most characteristics of the superconducting state, as well as spectral features, while spin fluctuations stabilize a nodeless d-wave symmetry of the order parameter, and otherwise are destructive for superconductivity in this material. There are still various open questions for this system, that one could address in future projects. For example, it would be important to rigorously resolve the issue of the superconducting gap anisotropy [73]. Even though orbital selective superconductivity has been proposed as mechanism for this phenomenon [53], it is an open question how to include such a treatment in our formalism, and what the effects would be. Further, it is possibly important to include the back reaction of the electrons onto the magnon spectrum, as has recently been claimed [76]. Incorporating this aspect into our multichannel Eliashberg theory is not a conceptual problem, but rather currently not practical due to the tremendous computational costs.

In TBG we were able to explain the main characteristics of the superconducting state by using isotropic EPI within a multiband Eliashberg theory. Further, we predicted various tunneling features and electron replica bands, where the latter are expected to occur more generally for all flat band systems with dominant phonon energy scale. However, it is still not clear how to reliably describe the full range of phenomena occurring at different doping levels, such as the correlated insulating states [79–81]. It is currently not known how to include such states on equal footing with superconductivity, hence considerable theoretical advances are needed in this direction. Additionally, it would be interesting to study TBG within a multichannel theory of superconductivity, since claims about the importance of purely electronic mechanisms have been made [185, 186].

As concerns the hydrides, we made predictions of close to room temperature superconductivity in metallic atomic hydrogen and predicted a new structural phase of LaH_{10}. For both materials the experimental picture is still elusive at the time of writing, and only future measurements will determine whether our predictions prove correct. The difficulty in atomic hydrogen is that its postulated metallic phase has yet to be rigorously shown to exist. If successful, examining the details of the superconducting state adds another layer of difficulty. As for LaH_{10}, the pressure regime for which we found a new trigonal phase ($250-425\,\mathrm{GPa}$) has not yet been explored experimentally, but we are optimistic that the required measurements will be carried out in the near future, given the rapid improvement of measurement techniques in the field and the importance attributed to this material.

We introduced a scheme to increase the efficiency of Matsubara space calculations by using EPI, i.e. for a known functional form of the interaction kernel. This can be considered a mere tool for theoretical calculations, and hence does not directly offer future research opportunities on the same topic. It should be noted that a generalization to other kinds of interactions, for which the precise mathematical form cannot be determined, is straight forward by fitting the kernel to a standard shape such as a Lorentzian. We continued by providing a comprehensive overview of effects due to phonon renormalization. Here it would be interesting to extend our formalism to real frequencies, which can be done by extending our frequently used analytic continuation scheme. Such an approach would lead to more ways to compare our theoretical calculations with experiment, since we would gain access to all spectral features of the system.

The second part of the thesis aims at contributing to the discussion on the superconductivity mediators in materials with unconventional gap symmetry. To this end we developed an extended Eliashberg formalism where all second order electron-phonon scattering processes are fully taken into account without further approximations, which has not been attempted before. Our calculations show that an optical phonon mode and isotropic electron-phonon coupling in this extended theory lead to unconventional gap symmetries as they have been experimentally found in Fe-based, cuprate and heavy fermion superconductors. Since such phonon modes unambiguously exist in the real materials, our results indicate that EPI plays a more important role in unconventional superconductors than previously thought. With ThFeAsN we studied an explicit example where such second order EPI might be indispensable to explain the superconducting state, in an attempt to connect our formalism to *ab initio* calculations. Lastly, we showed that Eliashberg theory beyond Migdal's approximation leads to coexisting even- and odd-frequency superconducting states in a cuprate model system, where the odd-frequency order parameter is induced.

From these findings and the associated theory developments in the thesis there are many possible future research directions. One open question is how to efficiently connect the vertex-corrected Eliashberg theory with *ab initio* input in a self-consistent way without neglecting potentially important contributions. To a different end, what happens if we include vertex corrections in a multichannel theory of superconductivity? Such a treatment would supposedly lead to a cooperative behavior of spin fluctuations and EPI, but deserves explicit calculations. On a related note, it is still an open challenge to include higher order corrections for the spin fluctuations mechanism into a self-consistent theory. Since there is no analogue of Migdal's theorem for purely electronic mechanisms, vertex corrections might prove particularly important. Ultimately, it would also be highly advantageous to search for spectral signatures as manifestation of non-negligible vertex corrections in unconventional superconductors. To achieve this, real-frequency dependent results are required which could be calculated by an extended version of our analytic continuation scheme. As concerns our findings of odd-frequency superconductivity, the next step would be to develop ideas for proving its existence experimentally. This is not a straight forward task because the even-frequency order parameter is dominant by an order of magnitude and both T_c's are equivalent. Nevertheless, there should exist a way of distinguishing even- and odd-frequency Cooper pairing and, if successful, this would be a direct signature of effects due to vertex-corrected EPI.

Popular science summary

Superconductivity is a macroscopic quantum phenomenon that occurs in certain types of materials upon sufficient cooling. Below a material specific critical temperature the superconductor's electrical resistance disappears and external magnetic fields are expelled from its interior. The discovery of this effect dates back more than a century ago, and it took almost 50 years until the first successful microscopic theory of superconductivity was proposed. Today a vast amount of superconducting materials are known, the most prominent families being elemental/conventional, copper-based, iron-based, heavy-fermion and high-pressure superconductors. One of the main goals of experimental and theoretical research in this field is to find a compound with critical temperature close to room temperature at ambient pressure, as such a material would offer enormous potential in technological applications.

The key for explaining superconductivity is the formation of so-called Cooper pairs, which are two electrons of opposite momentum and spin that feel an attraction between each other strong enough to overcome the Coulomb repulsion. These Cooper pairs do not behave like single electrons anymore in that their entirety in a material can mathematically be described by only one quantum mechanical wave function, which makes superconductivity a macroscopic quantum effect. Collectively, it is energetically favorable for single electrons to avoid scattering on the atoms of the parent material, which explains the loss of electrical resistance. Due to the fact that the superconducting state hosts an energetic advantage to Cooper pair formation, single electrons require additional energy to be excited and retrieve their individual character. This energy difference is called a superconducting gap, and is an important quantity for characterizing superconductors.

There are different possible mechanisms that can lead to Cooper pairing, and in this thesis we focus on electron-phonon interaction, which corresponds to lattice vibrations coupling via Coulomb forces with the electrons, and on spin fluctuations, for which the electrons themselves provide the coupling mechanism. There is general consensus that phonons are the dominant driving force for conventional and hydrogen based, high-pressure superconductivity, while the roles of electron-phonon coupling and spin fluctuations in unconventional superconductors (most of the cuprates, iron-based and heavy-fermion systems) are still actively debated. One key argument used in favor of spin fluctuation theories is the symmetry of the superconducting gap function, which changes sign in momentum space for many unconventional superconductors, a behavior that cannot be reproduced via the commonly employed standard theories of electron-phonon interactions. Due to this reason it is rather widely believed that spin fluctuations mediate Cooper pairing in these systems, so much so that sometimes unconventional and spin-fluctuations-mediated superconductivity are used interchangeably.

The first successful description of Cooper pairing is BCS theory, named after its inventors Bardeen, Cooper and Schrieffer. First published in 1957, BCS theory accounted for most of the superconducting systems known at the time, which were mainly of the elemental/conventional type. Only few years later Migdal published a milestone work on electron-phonon interaction in metals, which was generalized to the superconducting state by Eliashberg. The most important difference between Migdal-Eliashberg and BCS theory is that the former explicitly considers retardation time, which is the time delay it takes two electrons to form a Cooper pair via lattice vibrations, while the latter is a static description. In fact, it is possible to derive the BCS equations from Eliashberg theory under various approximations. It is worth noting that both theories rely on the so-called Migdal approximation, which states that it is sufficient to consider only first order electron-phonon scattering, provided that the ratio between phonon and electron energy scales is small. While this assumption leads to excellent agreement between experiment and outcomes from Eliashberg theory in conventional and high temperature, hydrogen based superconductors, it is less justified and less successful for unconventional systems.

This thesis is my humble contribution to the discussion on the role of spin fluctuations and electron-phonon interactions in mainly unconventional superconductors. The work is divided into two parts, according to the level of approximation used in the theory employed. In Part I all calculations are performed under the assumption that only first-order scattering events, either for electron-phonon interaction (Migdal's approximation) or spin fluctuations, play an important role for the superconducting state. The first system that I present here is a single layer of FeSe on a $SrTiO_3$ substrate, which currently has the highest critical temperature of all iron-based superconductors. I first consider both mediators of superconductivity separately, and then in a combined way. The results show that electron-phonon interactions are likely responsible for the experimentally observed spectral features and the high critical temperature, while spin fluctuations can lead to an unconventional gap symmetry and otherwise play a subdominant role.

I continue by presenting two projects on Twisted Bilayer Graphene, in which superconductivity has recently been discovered. This system is engineered by putting two sheets of graphene together at a relative twist angle of 1.1°, and has generated enormous research interest due to a rich variety of physical effects and easy experimental tunability. In this material I studied electron-phonon interactions within Eliashberg theory, above and below the superconducting critical temperature. These calculations explained various characteristics of the superconducting state, for which the gap symmetry is found as conventional, and lead to predictions of different experimentally observable spectral properties. After the discussion on Twisted Bilayer Graphene I move on to summarize various additional projects. Besides elaborating on electron-phonon mediated superconductivity at high pressures in the predicted metallic phase of atomic hydrogen and in a new trigonal structural phase of LaH_{10}, I introduce a method for making Eliashberg calculations computationally more efficient, and give an overview of effects, which can occur when the influence of electrons onto the lattice vibrations is taken into account.

In Part II of the thesis I consider electron-phonon interactions in unconventional superconductors. By taking into account all first and second order processes of electron-phonon scattering I derive a novel set of Eliashberg equations that go beyond Migdal's approximation. It turns out that the additional contributions can lead to changes in critical temperature, superconducting gap magnitude and effective coupling strength. Most importantly, for representative examples of iron-based, cuprates and heavy fermion superconductors, unconventional symmetries of the superconducting gap are obtained, which goes against the above described common notion that only spin fluctuations can produce such results. These findings thus point to the pivotal role of phonons for unconventional superconductors. With ThFeAsN I identify a likely candidate for such effects to occur in a real material.

The last project in this thesis concerns odd-frequency superconductivity. The superconducting gap in Eliashberg theory generally depends on the time difference between two electrons forming a Cooper pair, which can also be cast as a frequency dependence. In all known superconductors the energy gap is even under exchange of these relative times, i.e. it is invariant under inverting frequencies. However, it similarly is a theoretical possibility to have an odd-frequency dependence, which means that the gap function changes sign upon inversion of relative times, provided that the involved electrons have a more complicated spin dependence. Surprisingly, such a superconducting state is found here when solving the Eliashberg equations beyond Migdal's approximation, which I prove for a cuprate model system, in which primary even- and subordinate odd-frequency Cooper pairs coexist.

Populärvetenskaplig sammanfattning

Supraledning är ett makroskopiskt kvantfenomen som förekommer i vissa typer av material vid tillräcklig kylning. Under en materialspecifik kritisk temperatur försvinner supraledarens elektriska motstånd och yttre magnetfält trängs ut från dess inre. Upptäckten av denna effekt skedde för mer än ett sekel sedan, och det tog nästan 50 år innan den första framgångsrika mikroskopiska teorin om supraledning föreslogs. Idag är en stor mängd supraledande material känd. De mest framträdande familjerna är elementära/konventionella, kuprater, järnbaserade, tung-fermion och högtryckssupraledare. Ett av huvudmålen för experimentell och teoretisk forskning inom detta område är att hitta ett material med en kritisk temperatur nära rumstemperatur vid omgivningstryck, eftersom ett sådant material skulle erbjuda enorm potential för tekniska tillämpningar.

Nyckeln för att förklara supraledning är bildandet av så kallade Cooperpar, som är två elektroner med motsatta momentum och spinn som känner en attraktion mellan varandra som är tillräcklig stark för att övervinna Coulombavstötningen. Dessa Cooperpar beter sig inte längre som enstaka elektroner då deras helhet i ett material matematiskt kan beskrivas med endast en kvantmekanisk vågfunktion, vilket gör supraledningen till en makroskopisk kvanteffekt. Sammantaget är det energimässigt gynnsamt för enstaka elektroner att undvika spridning på atomerna i värdmaterialet, vilket förklarar förlusten av elektriskt motstånd. På grund av det faktum att det supraledande tillståndet levererar en energimässig fördel för Cooperparbildning, behöver enstaka elektroner ytterligare energi för att exciteras och återta sin individuella karaktär. Denna energiskillnad kallas för ett supraledande gap, som är en viktig kvantitet för att karakterisera supraledare.

Det finns olika möjliga mekanismer som kan leda till Cooperparning. I denna avhandling fokuserar vi på elektron-fonon-interaktion, vilket motsvarar gittervibrationernas koppling via Coulombkrafter med elektronerna, och på spinnfluktuationer, för vilka elektronerna själva tillhandahåller kopplingsmekanism. Det råder en allmän enighet om att fononer är den dominerande drivkraften för konventionell och vätebaserad högtryckssupraledning, medan elektron-fonon-kopplingen och spinnfluktuationer i okonventionella supraledare (de flesta kuprater, järnbaserade och tung-fermionsystem) fortfarande diskuteras aktivt. Ett nyckelargument som ofta används till stöd för teorier om spinnfluktuationer är symmetrin i supraledande gapfunktion, som ändrar tecken i momentum för många okonventionella supraledare, ett beteende som inte kan reproduceras med de vanliga standardteorierna om elektron-fonon-interaktioner.

Av denna anledning är det ganska allmänt trott att spinnfluktuationer förmedlar Cooperparning i dessa system, i en sådan utsträckning att okonventionell och spinnfluktuationsförmedlad supraledning ibland används synonymt.

Den första framgångsrika beskrivningen av Cooperparning är BCS-teorin, uppkallad efter uppfinnarna Bardeen, Cooper och Schrieffer. Först publicerad 1957 stod BCS-teorin för de flesta av de supraledande systemen som var kända vid den tiden, som huvudsakligen var av elementär/konventionell typ. Bara några år senare publicerade Migdal ett milstolpesarbete om elektron-fonon-interaktion i metaller, som generaliserades till supraledande tillstånd av Eliashberg. Den viktigaste skillnaden mellan Migdal-Eliashberg-teorin och BCS-teorin är att den förra uttryckligen inkluderar retardationstiden, vilken är den tidsfördröjning det tar för två elektroner att bilda ett Cooperpar med hjälp av gittervibrationer, medan den senare är en statisk beskrivning utan tidsberoende. Det är faktiskt möjligt att härleda BCS-ekvationerna från Eliashberg-teorin under olika approximationer. Det är värt att notera att båda teorierna bygger på den så kallade Migdal-approximationen, som innebär att det räcker att ta hänsyn till elektron-fonon-spridning av första ordningen, förutsatt att förhållandet mellan fonon- och elektronenergivågor är litet. Även om detta antagande leder till en utmärkt överensstämmelse mellan experiment och resultat från Eliashberg-teorin i konventionella och högtemperaturvätebaserade supraledare, är Migdal-approximationen mindre motiverat och mindre framgångsrikt för okonventionella system.

Denna avhandling är mitt anspråkslösa bidrag till diskussionen om spinnfluktuationer och elektron-fonon-interaktioner i huvudsakligen okonventionella supraledare. Arbetet är uppdelat i två delar, beroende på den approximationsnivå som används i teorin. I del I utförs alla beräkningar under antagandet att endast första ordningens spridningshändelser, antingen för elektron-fonon-interaktioner (Migdal-approximation) eller spinnfluktuationer, spelar en viktig roll för det supraledande tillståndet. Det första systemet som jag presenterar här består av ett enskilt lager FeSe på ett $\mathrm{SrTiO_3}$substrat, som för närvarande har den högsta kritiska temperaturen för alla järnbaserade supraledare. Jag eftersinnar först båda medlarna för supraledning separat, och kombinerar sedan dem. Resultaten visar att elektron-fonon-interaktioner sannolikt står för de experimentellt observerade spektralfunktionerna och den höga kritiska temperaturen, medan spinnfluktuationer kan orsaka en okonventionell gapsymmetri och annars spela en underordnad roll.

Därefter följer en presentation av två projekt om Twisted Bilayer Graphene, där supraledning nyligen har upptäckts. Detta system är konstruerat genom att man har lagt ihop två ark grafen i en relativ vridningsvinkel på $\sim 1,1^\circ$. Detta har genererat ett enormt forskningsintresse på grund av en mängd olika fysikaliska effekter och enkel experimentell avstämning. I detta material studerade jag elektron-fonon interaktioner inom Eliashberg-teorin, över och under den supraledande kritiska temperaturen. Dessa beräkningar förklarade olika egenskaper hos det supraledande tillståndet, där gapsymmetrin är konventionell, och leder till förutsägelser av olika experimentellt observerbara spektralegenskaper. Efter diskussionen om Twisted Bilayer Graphene fortsätter jag med att sammanfatta några olika projekt. Förutom att utveckla elektron-fononförmedlad supraledning vid högt tryck i den förutspådda metalliska fasen av atomärt väte och i en ny trigonal strukturell fas av LaH_{10}, introducerar jag en metod för att effektivisera Eliashbergberäkningarna och ge en överblick över effekter som kan uppstå när elektronernas påverkan på gittervibrationerna beaktas.

I del II av avhandlingen behandlar jag elektron-fonon-interaktioner i okonventionella supraledare. Genom att ta hänsyn till alla första och andra ordningens processer för elektron-fononspridning härleder jag en ny uppsättning Eliashberg-ekvationer bortom Migdal-approximation. Det visar sig att andra ordningens bidrag kan leda till förändringar i kritiska temperaturer, supraledande gapstorlekar och effektiv kopplingsstyrka. Viktigast av allt, för representativa exempel på järnbaserade, kuprater och tunga fermionsupraledare, erhålls okonventionella symmetrier av supraledande gap, vilket strider mot ovan beskrivna allmänna uppfattning om att endast spinnfluktuationer kan ge sådana resultat. Detta resultat pekar alltså på fononens avgörande roll för dessa okonventionella supraledare. Med ThFeAsN identifierar jag en sannolik kandidat där sådana effekter skulle kunna inträffa i ett verkligt material.

Det sista projektet i denna avhandling handlar om udda-frekvenssupraledning. Det supraledande gapet i Eliashberg-teorin beror i allmänhet på tidsskillnaden mellan de två elektronerna som bildar ett Cooperpar, vilket också kan beskrivas som ett frekvensberoende. I alla kända supraledare är energigapet jämn under utbyte av dessa relativa tider, det vill säga att det är invariant vid inverterande frekvenser. Emellertid är det på samma sätt en teoretisk möjlighet att ha ett udda frekvensberoende, vilket innebär att gapfunktionen ändrar tecken vid inversion av relativa tider, förutsatt att de involverade elektronerna har ett mer komplicerat spinnberoende. Överraskande nog finns ett sådant supraledande tillstånd här när man löser Eliashberg-ekvationerna bortom Migdal-approximationen, vilket jag bevisar för ett modellsystem av cuprater, där primära jämna och underordnade udda-frekvens Cooperpar samexisterar.

Populärwissenschaftliche Zusammenfassung

Supraleitung ist ein makroskopisches Quantenphänomen, das in bestimmten Materialien bei ausreichender Kühlung auftritt. Unterhalb einer materialspezifischen kritischen Temperatur verliert der Supraleiter jeglichen elektrischen Widerstand und äußere Magnetfelder werden aus seinem Inneren ausgestoßen. Die Entdeckung dieses Effekts liegt mehr als ein Jahrhundert zurück und es dauerte fast 50 Jahre, bis die erste erfolgreiche mikroskopische Theorie der Supraleitung aufgestellt wurde. Heutzutage ist eine große Anzahl supraleitender Materialien bekannt, wobei elementare/ konventionelle, kupferbasierte, eisenbasierte, schwere Fermion- und Hochdruck-Supraleiter zu den Bekanntesten zählen. Eines der Hauptziele experimenteller und theoretischer Forschung auf diesem Gebiet ist es, ein Material mit einer kritischen Temperatur nahe Raumtemperatur bei Umgebungsdruck zu finden, da ein solches Material enormes Potenzial für technologische Anwendungen bieten würde.

Der Schlüssel zum Verständnis von Supraleitung ist die Bildung sogenannter Cooper Paare. Hierbei handelt es sich um zwei Elektronen mit entgegengesetztem Impuls und Spin, die sich stark genug anziehen um die Coulomb Abstoßung zu überwinden. Diese Cooper Paare verhalten sich nicht wie isolierte Elektronen, da deren Gesamtheit in einem Material mathematisch durch nur eine einzelne quantenmechanische Wellenfunktion beschrieben werden kann, was Supraleitung zu einem makroskopischen Quanteneffekt macht. Für einzelne Elektronen ist es energetisch von Vorteil, Streuung an den Atomen des Materials zu vermeiden, was den Verlust des elektrischen Widerstands erklärt. Aufgrund der Tatsache, dass der supraleitende Zustand einen energetischen Vorteil für die Cooper-Paarbildung bietet, benötigen einzelne Elektronen zusätzliche Energie, um angeregt zu werden und ihren individuellen Charakter wiederzuerlangen. Diese Energiedifferenz wird als supraleitende Lücke bezeichnet und wird oft zur Charakterisierung von Supraleitern benutzt.

Es gibt verschiedene Mechanismen, die Cooper Paare erzeugen können, und in dieser Arbeit konzentriere ich mich auf Elektron-Phonon-Wechselwirkung, die der Kopplung zwischen Gitterschwingungen und Elektronen über Coulomb Kräfte entspricht, und Spinfluktuationen, für die die Elektronen selbst den Kopplungsmechanismus liefern. Es besteht allgemeiner Konsens, dass Phononen für konventionelle und Hochdruck-Supraleitung verantwortlich sind, während die Rolle der Elektron-Phonon-Kopplung und der Spinfluktuationen in unkonventionellen Supraleitern, welche die meisten der kupferbasierten, eisenbasierten und schweren Fermionsysteme darstellen, immer noch aktiv diskutiert wird. Ein wichtiges Argument zu Gunsten der Spinfluktuationstheorien ist die Symmetrie der supraleitenden Lückenfunktion, die bei vielen unkonventionellen Supraleitern ein alternierendes Vorzeichen im Impulsraum aufweist, ein Verhalten, welches mit gängigen Theorien der Elektron-Phonon-Wechselwirkung nicht reproduziert werden kann. Aus diesem Grund wird allgemein angenommen, dass Spinfluktuationen die Cooper Paare in diesen Systemen erzeugen, so dass die Begriffe unkonventionelle und Spinfluktuationen-erzeugte Supraleitung teilweise austauschbar verwendet werden.

Die erste erfolgreiche Beschreibung von Cooper Paaren ist die BCS-Theorie, benannt nach ihren Verfassern Bardeen, Cooper und Schrieffer. Diese Theorie, erstmals veröffentlicht 1957, lieferte eine Erklärung für die meisten damals bekannten supraleitenden Systeme, welche hauptsächlich vom elementaren/konventionellen Typ waren. Nur wenige Jahre später veröffentlichte Migdal seine revolutionäre Arbeit zur Elektron-Phonon-Wechselwirkung in Metallen, die von Eliashberg für den supraleitenden Zustand verallgemeinert wurde. Der wichtigste Unterschied zwischen der Migdal-Eliashberg- und der BCS-Theorie besteht darin, dass erstere explizit die Verzögerungszeit berücksichtigt, also die Zeit, die zwei Elektronen benötigen, um ein Cooper Paar mittels Gitterschwingungen zu bilden, während letztere eine statische Beschreibung ohne Zeitabhängigkeit ist. Tatsächlich ist es möglich, die BCS-Gleichungen unter verschiedenen Annahmen aus der Eliashberg-Theorie abzuleiten. Es ist erwähnenswert, dass beide Theorien auf der sogenannten Migdal-Näherung beruhen, die besagt, dass es ausreicht, nur Ereignisse erster Ordnung bei der Elektron-Phonon-Streuung zu berücksichtigen, vorausgesetzt, das Verhältnis zwischen Phononen- und Elektronenenergieskalen ist klein. Während diese Annahme zu einer hervorragenden Übereinstimmung zwischen Experiment und Ergebnissen der Eliashberg-Theorie in konventionellen und Hochdruck-Supraleitern führt, ist sie für unkonventionelle Systeme weniger gerechtfertigt und weniger erfolgreich.

Diese Arbeit stellt meinen bescheidenen Beitrag zur Diskussion bezüglich der Rolle von Spinfluktuationen und Elektron-Phonon-Wechselwirkungen in hauptsächlich unkonventionellen Supraleitern dar. Die Arbeit gliedert sich in zwei Teile, je nach Näherungsgrad der verwendeten Theorie. In Teil I werden alle Rechnungen unter der Annahme durchgeführt, dass nur Streuereignisse erster Ordnung, entweder für die Elektron-Phonon-Wechselwirkung (Migdals Näherung) oder Spinfluktuationen, eine wichtige Rolle für den supraleitenden Zustand spielen. Das erste System, das ich hier vorstelle, ist eine einzelne Schicht aus FeSe auf einem $SrTiO_3$ Substrat, welches derzeit die höchste kritische Temperatur aller eisenbasierter Supraleiter aufweist. Ich betrachte beide Mediatoren der Supraleitung zunächst getrennt und anschließend kombiniert. Die Ergebnisse zeigen, dass Elektron-Phonon-Wechselwirkungen sehr wahrscheinlich für die experimentell beobachteten spektralen Eigenschaften und die hohe kritische Temperatur des Systems verantwortlich sind, während Spinfluktuationen zu einer unkonventionellen Lückensymmetrie führen und darüber hinaus eine untergeordnete Rolle spielen.

Ich fahre damit fort, dass ich zwei Projekte zu Twisted Bilayer Graphene vorstelle, das kürzlich als Supraleiter identifiziert wurde. Dieses System wird konstruiert, indem zwei Graphenschichten in einem relativen Drehungswinkel von $\sim 1.1^\circ$ zusammengefügt werden. Aufgrund einer großen Vielfalt an physikalischen Effekten und einer einfachen experimentellen Abstimmbarkeit hat dieses ein enormes Forschungsinteresse geweckt. In diesem Material habe ich Elektron-Phonon-Wechselwirkungen innerhalb der Eliashberg-Theorie über und unterhalb der kritischen Temperatur untersucht. Meine Berechnungen erklären verschiedene Eigenschaften des supraleitenden Zustands, für den sich die Lückensymmetrie als konventionell herausstellt und führen zu Vorhersagen verschiedener experimentell beobachtbarer spektraler Eigenschaften. Im Anschluss hierauf fasse ich verschiedene Einzelprojekte zusammen. Neben der Erörterung der Elektron-Phonon-basierten Supraleitung bei hohen Drücken in der postulierten metallischen Phase von atomarem Wasserstoff und in einer neuen trigonalen Strukturphase von LaH_{10} stelle ich eine Methode vor, um Eliashberg-Rechnungen numerisch effizienter umzusetzen und gebe eine Übersicht über Effekte, die auftreten können, wenn der Einfluss von Elektronen auf die Gitterschwingungen berücksichtigt wird.

Im Teil II dieser Arbeit betrachte ich Elektron-Phonon-Wechselwirkungen in unkonventionellen Supraleitern. Unter Berücksichtigung aller Prozesse erster und zweiter Ordnung der Elektron-Phonon-Streuung leite ich ein System von Eliashberg-Gleichungen her, das über die Migdalsche Näherung hinausgeht. Es stellt sich heraus, dass die zusätzlichen Beiträge zu Veränderungen der kritischen Temperatur, Größe der Lückenfunktion und der effektiven Kopplungsstärke führen können. Am wichtigsten ist jedoch, dass für repräsentative Beispiele von eisenbasierten, kupferbasierten und schweren Fermionen-Supraleitern unkonventionelle Symmetrien der supraleitenden Lücke aus den Gleichungen hervorgehen, was der oben beschriebenen allgemeinen Vorstellung widerspricht, dass nur Spinfluktuationen solche Ergebnisse erzeugen können. Mit ThFeAsN identifiziere ich einen wahrscheinlichen Kandidaten für das Auftreten solcher Effekte in einem realen Material.

Im letzten Abschnitt dieser Dissertation beschäftige ich mich mit ungerader Supraleitung. Die supraleitende Lücke hängt im Allgemeinen von der Zeitdifferenz zwischen zwei Elektronen ab, die ein Cooper Paar bilden, was auch als Frequenzabhängigkeit angegeben werden kann. In den meisten Supraleitern ist die Energielücke gerade unter Austausch dieser relativen Zeiten, das heißt, sie ist invariant gegenüber invertierten Frequenzen. Theoretisch besteht jedoch die Möglichkeit, eine ungerade Frequenzabhängigkeit vorzufinden, was bedeutet, dass die Lückenfunktion bei Umkehrung der relativen Zeiten das Vorzeichen ändert, vorausgesetzt, die beteiligten Elektronen haben eine kompliziertere Spinabhängigkeit. Überraschenderweise finde ich solch einen supraleitenden Zustand ausgehend von dem neuen System von Eliashberg Gleichungen, wie ich für ein Modellsystem kupferbasierter Materialien beweise, in dem Cooper Paare mit gerader und ungerader Frequenzabhängigkeit koexistieren.

Acknowledgments

> *Thank you.*
>
> Unknown

> *And now... you've become a part of me. You'll always be right here.*
>
> Chester Bennington

It goes without saying that many people have contributed to my PhD studies, either by scientific advice or on a personal level. Here I'd like to express my great gratitude to them.

Starting with my supervisors, I'm grateful to Peter for giving me the opportunity to come to Uppsala and work in his group. I benefited from his exceptional over- and foresight, as well as of his broad experience in physics. Thank you also to my second supervisor Alex, who had great patience with me in the beginning when teaching me the basics of superconductivity. During the entire four years he would often make time for fruitful discussions. His expertise in the field of superconductivity is remarkable. Further, I'd like to thank Pablo for being third supervisor, I very much enjoyed your company in the university and on the football pitch.

I'm in debt to my collaborators Fairoja, Ashok Verma and Paritosh Modak, without whom the respective projects would not have been possible. Further I would like to thank the old and current members of the group, Marco, Ashok, Ulrike, Jerome and Leandro for fruitful discussions.

I specially want to thank Raquel and Duo for their constant support and encouragement. Not only were the coffee and lunch breaks with you a true pleasure, but also any kind of activities outside university.

Thanks to the entire Materials theory division for providing such a friendly and pleasant environment. Particularly I want to mention Rafael, Renan and Alena who contributed each in their own way to make everyday life more enjoyable. Jag är också mycket tacksam mot Camilla Thulin för korrekturläsning av den svenska sammanfattning. Further I want to express my gratitude towards people outside university, Adri, Ahmed and the entire football team IK Apollon, that provided me with great company and helped to clear my head once in a while.

Ein besonderes Dankeschön an Julia und Timo, für so manches an Rat, Beistand und Ablenkung. Abschließend möchte ich meinen Eltern und meinen beiden Brüdern Jan und Pascal danken, für die endlose Geduld, bedingungslose Unterstützung und für all die Besuche und Telefonate.

References

[1] H. Kamerlingh Onnes *Commun. Phys. Lab. Leiden*, vol. 12, 1911.

[2] W. Meissner and R. Ochsenfeld, *Naturwissenschaften*, vol. 21, pp. 787–788, Nov 1933.

[3] J. Bardeen, L. N. Cooper, and J. R. Schrieffer, *Phys. Rev.*, vol. 108, pp. 1175–1204, Dec 1957.

[4] A. B. Migdal *Sov. Phys. JETP*, vol. 34, p. 996, Dec 1958.

[5] G. M. Eliashberg *Sov. Phys. JETP*, vol. 11, no. 3, p. 696, 1960.

[6] W. L. McMillan *Phys. Rev.*, vol. 167, pp. 331–344, Mar 1968.

[7] R. C. Dynes *Solid State Communications*, vol. 10, no. 7, pp. 615–618, 1972.

[8] P. B. Allen and B. Mitrović,, in *Solid State Physics,* Vol. 37 (H. Ehrenreich, F. Seitz, and D. Turnbull,, eds.), pp. 1 – 92, Academic Press, 1983.

[9] G. Webb, F. Marsiglio, and J. Hirsch, *Physica C: Superconductivity and its Applications*, vol. 514, pp. 17–27, 2015.

[10] F. Steglich, J. Aarts, C. D. Bredl, W. Lieke, D. Meschede, W. Franz, and H. Schäfer, *Phys. Rev. Lett.*, vol. 43, pp. 1892–1896, Dec 1979.

[11] K. Miyake, S. Schmitt-Rink, and C. M. Varma, *Phys. Rev. B*, vol. 34, pp. 6554–6556, Nov 1986.

[12] N. D. Mathur, F. M. Grosche, S. R. Julian, I. R. Walker, D. M. Freye, R. K. W. Haselwimmer, and G. G. Lonzarich, *Nature*, vol. 394, pp. 39–43, Jul 1998.

[13] D. J. Scalapino, E. Loh, and J. E. Hirsch, *Phys. Rev. B*, vol. 34, pp. 8190–8192, Dec 1986.

[14] T. Moriya *Proceedings of the Japan Academy. Series B, Physical and biological sciences*, vol. 82, pp. 1–16, Mar 2006.

[15] B. Keimer, S. A. Kivelson, M. R. Norman, S. Uchida, and J. Zaanen, *Nature*, vol. 518, pp. 179–186, Feb 2015.

[16] Y. J. Uemura, G. M. Luke, B. J. Sternlieb, J. H. Brewer, J. F. Carolan, W. N. Hardy, R. Kadono, J. R. Kempton, R. F. Kiefl, S. R. Kreitzman, P. Mulhern, T. M. Riseman, D. L. Williams, B. X. Yang, S. Uchida, H. Takagi, J. Gopalakrishnan, A. W. Sleight, M. A. Subramanian, C. L. Chien, M. Z. Cieplak, G. Xiao, V. Y. Lee, B. W. Statt, C. E. Stronach, W. J. Kossler, and X. H. Yu, *Phys. Rev. Lett.*, vol. 62, pp. 2317–2320, May 1989.

[17] A. V. Chubukov, A. Abanov, I. Esterlis, and S. A. Kivelson, *Ann. Phys.*, vol. 417, p. 168190, 2020.

[18] A. P. Drozdov, P. P. Kong, V. S. Minkov, S. P. Besedin, M. A. Kuzovnikov, S. Mozaffari, L. Balicas, F. Balakirev, D. Graf, V. B. Prakapenka, E. Greenberg, D. A. Knyazev, M. Tkacz, and M. I. Eremets, *Nature*, vol. 569, pp. 528 –531, 2019.

[19] E. Snider, N. Dasenbrock-Gammon, R. McBride, M. Debessai, H. Vindana, K. Vencatasamy, K. V. Lawler, A. Salamat, and R. P. Dias, *Nature*, vol. 586, p. 373, 2020.

[20] Y. Nambu *Phys. Rev.*, vol. 117, pp. 648–663, Feb 1960.

[21] J. A. Hertz, K. Levin, and M. T. Beal-Monod, *Solid State Commun.*, vol. 18, no. 7, pp. 803–806, 1976.

[22] F. Marsiglio, M. Schossmann, and J. P. Carbotte, *Phys. Rev. B*, vol. 37, pp. 4965–4969, Apr 1988.

[23] S. Mirabi, R. Boyack, and F. Marsiglio, *Phys. Rev. B*, vol. 101, p. 064506, Feb 2020.

[24] J. P. Carbotte *Rev. Mod. Phys.*, vol. 62, pp. 1027–1157, Oct 1990.

[25] D. A. Kirzhnits, E. G. Maksimov, and D. I. Khomskii, *Journal of Low Temperature Physics*, vol. 10, pp. 79–93, Jan 1973.

[26] C. R. Leavens and J. P. Carbotte, *Journal of Low Temperature Physics*, vol. 14, pp. 195–211, Jan 1974.

[27] P. B. Allen and R. C. Dynes, *Phys. Rev. B*, vol. 12, pp. 905–922, Aug 1975.

[28] N. N. Bogolyubov, V. V. Tolmachev, and D. V. Shirkov, *Fortsch. Phys.*, vol. 6, pp. 605–682, 1958.

[29] J. G. Valatin *Il Nuovo Cimento (1955-1965)*, vol. 7, pp. 843–857, Mar 1958.

[30] J. Bardeen, L. N. Cooper, and J. R. Schrieffer,, *Theory of Superconductivity*, pp. 15–44.

[31] J. P. Carbotte and F. Marsiglio,, *Electron-Phonon Superconductivity*, pp. 233–345. Berlin, Heidelberg: Springer, 2003.

[32] S. Graser, T. A. Maier, P. J. Hirschfeld, and D. J. Scalapino, *New Journal of Physics*, vol. 11, p. 025016, feb 2009.

[33] A. F. Kemper, T. A. Maier, S. Graser, H.-P. Cheng, P. J. Hirschfeld, and D. J. Scalapino, *New J. Phys.*, vol. 12, p. 073030, jul 2010.

[34] F.-C. Hsu, J.-Y. Luo, K.-W. Yeh, T.-K. Chen, T.-W. Huang, P. M. Wu, Y.-C. Lee, Y.-L. Huang, Y.-Y. Chu, D.-C. Yan, and M.-K. Wu, *Proc. Natl. Acad. Sci. USA*, vol. 105, no. 38, pp. 14262–14264, 2008.

[35] T. M. McQueen, A. J. Williams, P. W. Stephens, J. Tao, Y. Zhu, V. Ksenofontov, F. Casper, C. Felser, and R. J. Cava, *Phys. Rev. Lett.*, vol. 103, p. 057002, Jul 2009.

[36] S.-H. Baek, J. Mok, J. S. Kim, S. Aswartham, I. Morozov, D. Chareev, T. Urata, K. Tanigaki, Y. Tanabe, B. Büchner, and D. V. Efremov, *njp Quant. Mater.*, vol. 5, p. 8, 2020.

[37] A. Kreisel, P. J. Hirschfeld, and B. M. Andersen, *Symmetry*, vol. 12, no. 9, 2020.

[38] M. C. Rahn, R. A. Ewings, S. J. Sedlmaier, S. J. Clarke, and A. T. Boothroyd, *Phys. Rev. B*, vol. 91, p. 180501, 2015.

[39] D. J. Scalapino *Rev. Mod. Phys.*, vol. 84, pp. 1383–1417, Oct 2012.

[40] S. Kasahara, T. Watashige, T. Hanaguri, Y. Kohsaka, T. Yamashita, Y. Shimoyama, Y. Mizukami, R. Endo, H. Ikeda, K. Aoyama, T. Terashima, S. Uji, T. Wolf, H. von Löhneysen, T. Shibauchi, and Y. Matsuda, *Proceedings of the National Academy of Sciences*, vol. 111, no. 46, pp. 16309–16313, 2014.

[41] S. Rinott, K. B. Chashka, A. Ribak, E. D. L. Rienks, A. Taleb-Ibrahimi, P. Le Fevre, F. Bertran, M. Randeria, and A. Kanigel, *Science Advances*, vol. 3, no. 4, 2017.

[42] D. Van der Marel *Physica C: Superconductivity*, vol. 165, no. 1, pp. 35–43, 1990.

[43] G. Rietveld, M. van Veenendaal, D. van der Marel, and J. Mooij, *Physica B: Condensed Matter*, vol. 165-166, pp. 1605–1606, 1990. LT-19.

[44] L. C. Rhodes, M. D. Watson, A. A. Haghighirad, M. Eschrig, and T. K. Kim, *Phys. Rev. B*, vol. 95, p. 195111, May 2017.

[45] H. Eschrig and K. Koepernik, *Phys. Rev. B*, vol. 80, p. 104503, Sep 2009.

[46] W. Qing-Yan, L. Zhi, Z. Wen-Hao, Z. Zuo-Cheng, Z. Jin-Song, L. Wei, D. Hao, O. Yun-Bo, D. Peng, C. Kai, W. Jing, S. Can-Li, H. Ke, J. Jin-Feng, J. Shuai-Hua, W. Ya-Yu, W. Li-Li, C. Xi, M. Xu-Cun, and X. Qi-Kun, *Chin. Phys. Lett.*, vol. 29, no. 3, p. 037402, 2012.

[47] D. Liu, W. Zhang, D. Mou, J. He, Y.-B. Ou, Q.-Y. Wang, Z. Li, L. Wang, L. Zhao, S. He, Y. Peng, X. Liu, C. Chen, L. Yu, G. Liu, X. Dong, J. Zhang, C. Chen, Z. Xu, J. Hu, X. Chen, X. Ma, Q. Xue, and X. Zhou, *Nat. Commun.*, vol. 3, p. 931, July 2012.

[48] J.-F. Ge, Z.-L. Liu, C. Liu, C.-L. Gao, D. Qian, Q.-K. Xue, Y. Liu, and J.-F. Jia, *Nat. Mater.*, vol. 14, pp. 285–289, Mar. 2015.

[49] X. Liu, L. Zhao, S. He, J. He, D. Liu, D. Mou, B. Shen, Y. Hu, J. Huang, and X. J. Zhou, *J. Phys.: Condens. Matter*, vol. 27, p. 183201, apr 2015.

[50] C. H. P. Wen, H. C. Xu, C. Chen, Z. C. Huang, X. Lou, Y. J. Pu, Q. Song, B. P. Xie, M. Abdel-Hafiez, D. A. Chareev, A. N. Vasiliev, R. Peng, and D. L. Feng, *Nat. Commun.*, vol. 7, p. 10840, Mar 2016.

[51] B. Lei, J. H. Cui, Z. J. Xiang, C. Shang, N. Z. Wang, G. J. Ye, X. G. Luo, T. Wu, Z. Sun, and X. H. Chen, *Phys. Rev. Lett.*, vol. 116, p. 077002, Feb 2016.

[52] A. Linscheid, S. Maiti, Y. Wang, S. Johnston, and P. J. Hirschfeld, *Phys. Rev. Lett.*, vol. 117, p. 077003, Aug 2016.

[53] A. Kreisel, B. M. Andersen, P. O. Sprau, A. Kostin, J. C. S. Davis, and P. J. Hirschfeld, *Phys. Rev. B*, vol. 95, p. 174504, May 2017.

[54] J. J. Lee, F. T. Schmitt, R. G. Moore, S. Johnston, Y.-T. Cui, W. Li, M. Yi, Z. K. Liu, M. Hashimoto, Y. Zhang, D. H. Lu, T. P. Devereaux, D.-H. Lee, and Z.-X. Shen, *Nature*, vol. 515, pp. 245–248, Nov. 2014.

[55] S. N. Rebec, T. Jia, C. Zhang, M. Hashimoto, D.-H. Lu, R. G. Moore, and Z.-X. Shen, *Phys. Rev. Lett.*, vol. 118, p. 067002, Feb 2017.

[56] L. Rademaker, Y. Wang, T. Berlijn, and S. Johnston, *New J. Phys.*, vol. 18, no. 2, p. 022001, 2016.

[57] Y. Wang, K. Nakatsukasa, L. Rademaker, T. Berlijn, and S. Johnston, *Supercond. Sci. Technol.*, vol. 29, no. 5, p. 054009, 2016.

[58] A. Aperis and P. M. Oppeneer, *Phys. Rev. B*, vol. 97, p. 060501, Feb 2018.

[59] C. Liu, J. Mao, H. Ding, R. Wu, C. Tang, F. Li, K. He, W. Li, C.-L. Song, X.-C. Ma, Z. Liu, L. Wang, and Q.-K. Xue, *Phys. Rev. B*, vol. 97, p. 024502, Jan 2018.

[60] Q. Fan, W. H. Zhang, X. Liu, Y. J. Yan, M. Q. Ren, R. Peng, H. C. Xu, B. P. Xie, J. P. Hu, T. Zhang, and D. L. Feng, *Nat. Phys.*, vol. 11, pp. 946–952, Aug. 2015.

[61] Z. Ge, C. Yan, H. Zhang, D. Agterberg, M. Weinert, and L. Li, *Nano Lett.*, vol. 19, pp. 2497–2502, 2019.

[62] C. Liu, Z. Wang, S. Ye, C. Chen, Y. Liu, Q. Wang, Q.-H. Wang, and J. Wang, *Nano Letters*, vol. 19, pp. 3464–3472, Jun 2019.

[63] H. Zhang, Z. Ge, M. Weinert, and L. Li, *Commun. Phys.*, vol. 3, p. 75, 2020.

[64] N. Hao and J. Hu, *Phys. Rev. X*, vol. 4, p. 031053, Sep 2014.

[65] Y. Xie, H.-Y. Cao, Y. Zhou, S. Chen, H. Xiang, and X.-G. Gong, *Sci. Rep.*, vol. 5, p. 10011, June 2015.

[66] C. Zhang, Z. Liu, Z. Chen, Y. Xie, R. He, S. Tang, J. He, W. Li, T. Jia, S. N. Rebec, E. Y. Ma, H. Yan, M. Hashimoto, D. Lu, S.-K. Mo, Y. Hikita, R. G. Moore, H. Y. Hwang, D. Lee, and Z. Shen, *Nat. Commun.*, vol. 8, p. 14468, Feb. 2017.

[67] B. D. Faeth, S. Xie, S. Yang, J. K. Kawasaki, J. N. Nelson, S. Zhang, C. Parzyck, P. Mishra, C. Li, C. Jozwiak, A. Bostwick, E. Rotenberg, D. G. Schlom, and K. M. Shen, *Phys. Rev. Lett.*, vol. 127, p. 016803, Jun 2021.

[68] K. Shigekawa, K. Nakayama, G. N. Phan, M. Kuno, K. Sugawara, T. Takahashi, and T. Sato, *Journal of Physics: Conference Series*, vol. 1054, p. 012019, jul 2018.

[69] K. Kubo *Phys. Rev. B*, vol. 75, p. 224509, Jun 2007.

[70] L. Jiao, C.-L. Huang, S. Rößler, C. Koz, U. K. Rößler, U. Schwarz, and S. Wirth, *Sci. Rep.*, vol. 7, p. 44024, Mar 2017.

[71] P. O. Sprau, A. Kostin, A. Kreisel, A. E. Böhmer, V. Taufour, P. C. Canfield, S. Mukherjee, P. J. Hirschfeld, B. M. Andersen, and J. C. S. Davis, *Science*, vol. 357, no. 6346, pp. 75–80, 2017.

[72] S. Mandal, P. Zhang, S. Ismail-Beigi, and K. Haule, *Phys. Rev. Lett.*, vol. 119, p. 067004, Aug 2017.

[73] Y. Zhang, J. J. Lee, R. G. Moore, W. Li, M. Yi, M. Hashimoto, D. H. Lu, T. P. Devereaux, D.-H. Lee, and Z.-X. Shen, *Phys. Rev. Lett.*, vol. 117, p. 117001, Sep 2016.

[74] C. Tang, C. Liu, G. Zhou, F. Li, H. Ding, Z. Li, D. Zhang, Z. Li, C. Song, S. Ji, K. He, L. Wang, X. Ma, and Q.-K. Xue, *Phys. Rev. B*, vol. 93, p. 020507, Jan 2016.

[75] S. He, J. He, W. Zhang, L. Zhao, D. Liu, X. Liu, D. Mou, Y.-B. Ou, Q.-Y. Wang, Z. Li, L. Wang, Y. Peng, Y. Liu, C. Chen, L. Yu, G. Liu, X. Dong, J. Zhang, C. Chen, Z. Xu, X. Chen, X. Ma, Q. Xue, and X. J. Zhou, *Nat. Mater.*, vol. 12, pp. 605–610, July 2013.

[76] L. Rademaker, G. Alvarez-Suchini, K. Nakatsukasa, Y. Wang, and S. Johnston, *Phys. Rev. B*, vol. 103, p. 144504, Apr 2021.

[77] R. Bistritzer and A. H. MacDonald, *Proc. Natl. Acad. Sci. USA*, vol. 108, no. 30, pp. 12233–12237, 2011.

[78] E. Suárez Morell, J. D. Correa, P. Vargas, M. Pacheco, and Z. Barticevic, *Phys. Rev. B*, vol. 82, p. 121407, Sep 2010.

[79] Y. Cao, V. Fatemi, S. Fang, K. Watanabe, T. Taniguchi, E. Kaxiras, and P. Jarillo-Herrero, *Nature*, vol. 556, pp. 43–50, Apr. 2018.

[80] Y. Cao, V. Fatemi, A. Demir, S. Fang, S. L. Tomarken, J. Y. Luo, J. D. Sanchez-Yamagishi, K. Watanabe, T. Taniguchi, E. Kaxiras, R. C. Ashoori, and P. Jarillo-Herrero, *Nature*, vol. 556, pp. 80–84, Apr. 2018.

[81] M. Yankowitz, S. Chen, H. Polshyn, Y. Zhang, K. Watanabe, T. Taniguchi, D. Graf, A. F. Young, and C. R. Dean, *Science*, vol. 363, p. 1059, 2019.

[82] Y. Xie, B. Lian, B. Jäck, X. Liu, C.-L. Chiu, K. Watanabe, T. Taniguchi, B. A. Bernevig, and A. Yazdani, *Nature*, vol. 572, pp. 101–105, Aug 2019.

[83] A. Kerelsky, L. J. McGilly, D. M. Kennes, L. Xian, M. Yankowitz, S. Chen,

K. Watanabe, T. Taniguchi, J. Hone, C. Dean, A. Rubio, and A. N. Pasupathy, *Nature*, vol. 572, pp. 95–100, Aug 2019.

[84] H. S. Arora, R. Polski, Y. Zhang, A. Thomson, Y. Choi, H. Kim, Z. Lin, I. Z. Wilson, X. Xu, J.-H. Chu, K. Watanabe, T. Taniguchi, J. Alicea, and S. Nadj-Perge, *Nature*, vol. 583, pp. 379–384, Jul 2020.

[85] Y. Choi, H. Kim, Y. Peng, A. Thomson, C. Lewandowski, R. Polski, Y. Zhang, H. S. Arora, K. Watanabe, T. Taniguchi, J. Alicea, and S. Nadj-Perge, *Nature*, vol. 589, pp. 536–541, Jan 2021.

[86] T. J. Peltonen, R. Ojajärvi, and T. T. Heikkilä, *Phys. Rev. B*, vol. 98, p. 220504, Dec 2018.

[87] H. C. Po, L. Zou, T. Senthil, and A. Vishwanath, *Phys. Rev. B*, vol. 99, p. 195455, May 2019.

[88] J. M. B. Lopes dos Santos, N. M. R. Peres, and A. H. Castro Neto, *Phys. Rev. B*, vol. 86, p. 155449, Oct 2012.

[89] N. N. T. Nam and M. Koshino, *Phys. Rev. B*, vol. 96, p. 075311, Aug 2017.

[90] S. Fang and E. Kaxiras, *Phys. Rev. B*, vol. 93, p. 235153, Jun 2016.

[91] K. Uchida, S. Furuya, J.-I. Iwata, and A. Oshiyama, *Phys. Rev. B*, vol. 90, p. 155451, Oct 2014.

[92] Y. W. Choi and H. J. Choi, *Phys. Rev. B*, vol. 98, p. 241412, Dec 2018.

[93] A. I. Cocemasov, D. L. Nika, and A. A. Balandin, *Phys. Rev. B*, vol. 88, p. 035428, Jul 2013.

[94] F. Wu, A. H. MacDonald, and I. Martin, *Phys. Rev. Lett.*, vol. 121, p. 257001, Dec 2018.

[95] X. Lu, P. Stepanov, W. Yang, M. Xie, M. A. Aamir, I. Das, C. Urgell, K. Watanabe, T. Taniguchi, G. Zhang, A. Bachtold, A. H. MacDonald, and D. K. Efetov, *Nature*, vol. 574, pp. 653–657, Oct 2019.

[96] D. J. Scalapino, J. R. Schrieffer, and J. W. Wilkins, *Phys. Rev.*, vol. 148, pp. 263–279, Aug 1966.

[97] D. J. Scalapino, S. R. White, and S. C. Zhang, *Phys. Rev. Lett.*, vol. 68, pp. 2830–2833, May 1992.

[98] S. Peotta and P. Törmä, *Nature Communications*, vol. 6, p. 8944, Nov 2015.

[99] F. Marsiglio and J. P. Carbotte, *Phys. Rev. B*, vol. 43, pp. 5355–5363, Mar 1991.

[100] H. Liu, I. I. Naumov, R. Hoffmann, N. W. Ashcroft, and R. J. Hemley, *Proc. Natl. Acad. Sci. USA*, vol. 114, pp. 6990 – 6995, 2017.

[101] M. Somayazulu, M. Ahart, A. K. Mishra, Z. M. Geballe, M. Baldini, Y. Meng, V. V. Struzhkin, and R. J. Hemley, *Phys. Rev. Lett.*, vol. 122, p. 027001, Jan 2019.

[102] I. A. Troyan, D. V. Semenok, A. G. Kvashnin, A. V. Sadakov, O. A. Sobolevskiy, V. M. Pudalov, A. G. Ivanova, V. B. Prakapenka, E. Greenberg, A. G. Gavriliuk, I. S. Lyubutin, V. V. Struzhkin, A. Bergara, I. Errea, R. Bianco, M. Calandra, F. Mauri, L. Monacelli, R. Akashi, and A. R. Oganov, *Advanced Materials*, vol. 33, no. 15, p. 2006832, 2021.

[103] P. P. Kong, V. S. Minkov, M. A. Kuzovnikov, S. P. Besedin, A. P. Drozdov, S. Mozaffari, L. Balicas, F. F. Balakirev, V. B. Prakapenka, E. Greenberg, D. A. Knyazev, and M. I. Eremets,, "Superconductivity up to 243 K in yttrium hydrides under high pressure," 2019.

[104] E. Wigner and H. B. Huntington, *J. Chem. Phys.*, vol. 3, p. 764, 1935.

[105] H. K. Mao and R. J. Hemley, *Science*, vol. 244, no. 4911, pp. 1462–1465, 1989.

[106] C. Ji, B. Li, W. Liu, J. S. Smith, A. Majumdar, W. Luo, R. Ahuja, J. Shu, J. Wang, S. Sinogeikin, Y. Meng, V. B. Prakapenka, E. Greenberg, R. Xu, X. Huang, W. Yang, G. Shen, W. L. Mao, and H.-K. Mao, *Nature*, vol. 573, pp. 558 – 562, 2019.

[107] P. Loubeyre, F. Occelli, and P. Dumas, *Nature*, vol. 577, pp. 631–635, Jan 2020.

[108] N. W. Ashcroft *Phys. Rev. Lett.*, vol. 21, pp. 1748–1749, Dec 1968.

[109] J. M. McMahon and D. M. Ceperley, *Phys. Rev. Lett.*, vol. 106, p. 165302, Apr 2011.

[110] Y. Yan, J. Gong, and Y. Liu, *Phys. Lett. A*, vol. 375, no. 9, pp. 1264 – 1268, 2011.

[111] M. Borinaga, I. Errea, M. Calandra, F. Mauri, and A. Bergara, *Phys. Rev. B*, vol. 93, p. 174308, May 2016.

[112] F. Peng, Y. Sun, C. J. Pickard, R. J. Needs, Q. Wu, and Y. Ma, *Phys. Rev. Lett.*, vol. 119, p. 107001, Sep 2017.

[113] I. Errea, F. Belli, L. Monacelli, A. Sanna, T. Koretsune, T. Tadano, R. Bianco, M. Calandra, R. Arita, F. Mauri, and J. A. Flores-Livas, *Nature*, vol. 578, pp. 66–69, Feb 2020.

[114] A. M. Shipley, M. J. Hutcheon, M. S. Johnson, R. J. Needs, and C. J. Pickard, *Phys. Rev. B*, vol. 101, p. 224511, Jun 2020.

[115] J. J. Deisz, D. Hess, and J. W. Serene,, *Recent Progress in Many-Body Theories*, vol. 4. Plenum Press, New York, 1995.

[116] J. J. Deisz, D. W. Hess, and J. W. Serene, *Phys. Rev. B*, vol. 66, p. 014539, Jul 2002.

[117] N. Witt, E. G. C. P. van Loon, T. Nomoto, R. Arita, and T. O. Wehling, *Phys. Rev. B*, vol. 103, p. 205148, May 2021.

[118] F. Marsiglio *Phys. Rev. B*, vol. 42, pp. 2416–2424, Aug 1990.

[119] R. T. Scalettar, N. E. Bickers, and D. J. Scalapino, *Phys. Rev. B*, vol. 40, pp. 197–200, Jul 1989.

[120] I. Esterlis, B. Nosarzewski, E. W. Huang, B. Moritz, T. P. Devereaux, D. J. Scalapino, and S. A. Kivelson, *Phys. Rev. B*, vol. 97, p. 140501, Apr 2018.

[121] I. Esterlis, S. A. Kivelson, and D. J. Scalapino, *npj Quantum Mater.*, vol. 3, no. 1, p. 59, 2018.

[122] J. Bauer, J. E. Han, and O. Gunnarsson, *Phys. Rev. B*, vol. 84, p. 184531, Nov 2011.

[123] A. S. Alexandrov *Europhys. Lett. (EPL)*, vol. 56, pp. 92–98, oct 2001.

[124] N. C. Costa, T. Blommel, W.-T. Chiu, G. Batrouni, and R. T. Scalettar, *Phys. Rev. Lett.*, vol. 120, p. 187003, May 2018.

[125] P. M. Dee, K. Nakatsukasa, Y. Wang, and S. Johnston, *Phys. Rev. B*, vol. 99, p. 024514, Jan 2019.

[126] J. E. Moussa and M. L. Cohen, *Phys. Rev. B*, vol. 74, p. 094520, Sep 2006.

[127] A. Damascelli, Z. Hussain, and Z.-X. Shen, *Rev. Mod. Phys.*, vol. 75, pp. 473–541, 2003.

[128] L. Pietronero and S. Strässler, *Europhysics Letters (EPL)*, vol. 18,

pp. 627–633, apr 1992.

[129] M. V. Sadovskii *J. Exp. Theor. Phys.*, vol. 128, pp. 455–463, Mar 2019.

[130] P. Benedetti, C. Grimaldi, L. Pietronero, and G. Varelogiannis, *Europhysics Letters (EPL)*, vol. 28, pp. 351–356, nov 1994.

[131] L. Pietronero, S. Strässler, and C. Grimaldi, *Physica B: Condensed Matter*, vol. 204, no. 1, pp. 222 – 227, 1995.

[132] C. Grimaldi, L. Pietronero, and S. Strässler, *Phys. Rev. Lett.*, vol. 75, pp. 1158–1161, Aug 1995.

[133] E. Cappelluti, C. Grimaldi, and L. Pietronero, *Journal of Superconductivity*, vol. 10, pp. 397–403, Aug 1997.

[134] M. Botti, E. Cappelluti, C. Grimaldi, and L. Pietronero, *Phys. Rev. B*, vol. 66, p. 054532, Aug 2002.

[135] P. Miller, J. K. Freericks, and E. J. Nicol, *Phys. Rev. B*, vol. 58, pp. 14498–14510, Dec 1998.

[136] J. P. Hague *Journal of Physics: Condensed Matter*, vol. 15, pp. 2535–2550, apr 2003.

[137] J. P. Hague *Journal of Physics: Condensed Matter*, vol. 17, pp. 5663–5676, sep 2005.

[138] D. C. Johnston *Adv. Phys.*, vol. 59, pp. 803–1061, Nov. 2010.

[139] M. Grabowski and L. J. Sham, *Phys. Rev. B*, vol. 29, pp. 6132–6142, Jun 1984.

[140] J. P. Hague *Phys. Rev. B*, vol. 73, p. 060503, Feb 2006.

[141] J. P. Hague *Journal of Physics: Conference Series*, vol. 92, p. 012119, dec 2007.

[142] P. V. Bogdanov, A. Lanzara, X. J. Zhou, W. L. Yang, H. Eisaki, Z. Hussain, and Z. X. Shen, *Phys. Rev. Lett.*, vol. 89, p. 167002, Sep 2002.

[143] X. J. Zhou, T. Yoshida, S. A. Kellar, P. V. Bogdanov, E. D. Lu, A. Lanzara, M. Nakamura, T. Noda, T. Kakeshita, H. Eisaki, S. Uchida, A. Fujimori, Z. Hussain, and Z.-X. Shen, *Phys. Rev. Lett.*, vol. 86, pp. 5578–5581, Jun 2001.

[144] X. Chen, P. Dai, D. Feng, T. Xiang, and F.-C. Zhang, *National Science Review*, vol. 1, pp. 371–395, 07 2014.

[145] C. Cao, P. J. Hirschfeld, and H.-P. Cheng, *Phys. Rev. B*, vol. 77, p. 220506, Jun 2008.

[146] C. Putzke, A. I. Coldea, I. Guillamón, D. Vignolles, A. McCollam, D. LeBoeuf, M. D. Watson, I. I. Mazin, S. Kasahara, T. Terashima, T. Shibauchi, Y. Matsuda, and A. Carrington, *Phys. Rev. Lett.*, vol. 108, p. 047002, Jan 2012.

[147] J. S. Van Dyke, F. Massee, M. P. Allan, J. C. S. Davis, C. Petrovic, and D. K. Morr, *Proceedings of the National Academy of Sciences*, vol. 111, no. 32, pp. 11663–11667, 2014.

[148] K. Kuroki, S. Onari, R. Arita, H. Usui, Y. Tanaka, H. Kontani, and H. Aoki, *Phys. Rev. Lett.*, vol. 101, p. 087004, Aug 2008.

[149] M. Nakata, D. Ogura, H. Usui, and K. Kuroki, *Phys. Rev. B*, vol. 95, p. 214509, Jun 2017.

[150] M. Cyrot *Solid State Communications*, vol. 60, no. 3, pp. 253–256, 1986.

[151] T. Moriya and K. Ueda, *Reports on Progress in Physics*, vol. 66, pp. 1299–1341, jul 2003.

[152] P. Monthoux and G. G. Lonzarich, *Phys. Rev. B*, vol. 71, p. 054504, Feb 2005.

[153] P. Monthoux, D. Pines, and G. G. Lonzarich, *Nature*, vol. 450, pp. 1177–1183, Dec 2007.

[154] M. R. Norman *Science*, vol. 332, no. 6026, pp. 196–200, 2011.

[155] A. F. Kemper, M. M. Korshunov, T. P. Devereaux, J. N. Fry, H.-P. Cheng, and P. J. Hirschfeld, *Phys. Rev. B*, vol. 83, p. 184516, May 2011.

[156] A. Lanzara, P. V. Bogdanov, X. J. Zhou, S. A. Kellar, D. L. Feng, E. D. Lu, T. Yoshida, H. Eisaki, A. Fujimori, K. Kishio, J.-I. Shimoyama, T. Noda, S. Uchida, Z. Hussain, and Z.-X. Shen, *Nature*, vol. 412, no. 6846, pp. 510–514, 2001.

[157] L. Boeri, O. Dolgov, and A. Golubov, *Physica C: Superconductivity*, vol. 469, no. 9, pp. 628 – 634, 2009. Superconductivity in Iron-Pnictides.

[158] M. Zbiri, H. Schober, M. R. Johnson, S. Rols, R. Mittal, Y. Su, M. Rotter, and D. Johrendt, *Phys. Rev. B*, vol. 79, p. 064511, Feb 2009.

[159] A. A. Kordyuk, V. B. Zabolotnyy, D. V. Evtushinsky, T. K. Kim, I. V. Morozov, M. L. Kulić, R. Follath, G. Behr, B. Büchner, and S. V. Borisenko, *Phys. Rev. B*, vol. 83, p. 134513, Apr 2011.

[160] H. Martinho, P. G. Pagliuso, V. Fritsch, N. O. Moreno, J. L. Sarrao, and C. Rettori, *Phys. Rev. B*, vol. 75, p. 045108, Jan 2007.

[161] C. Tsuei and J. Kirtley, *Physica C: Superconductivity*, vol. 341-348, pp. 1625–1628, 2000.

[162] P. J. Hirschfeld, M. M. Korshunov, and I. I. Mazin, *Reports on Progress in Physics*, vol. 74, p. 124508, oct 2011.

[163] Y. Fasano, P. Szabó, J. Kačmarčík, Z. Pribulová, P. Pedrazzini, P. Samuely, and V. Correa, *Physica B: Condensed Matter*, vol. 536, pp. 798 – 802, 2018.

[164] C. Wang, Z.-C. Wang, Y.-X. Mei, Y.-K. Li, L. Li, Z.-T. Tang, Y. Liu, P. Zhang, H.-F. Zhai, Z.-A. Xu, and G.-H. Cao, *J. Amer. Chem. Soc.*, vol. 138, pp. 2170–2173, Feb 2016.

[165] D. J. Singh *J. Alloys and Compnds.*, vol. 687, pp. 786 – 789, 2016.

[166] S. Sen and G.-Y. Guo, *Phys. Rev. B*, vol. 102, p. 224505, Dec 2020.

[167] I. I. Mazin, D. J. Singh, M. D. Johannes, and M. H. Du, *Phys. Rev. Lett.*, vol. 101, p. 057003, Jul 2008.

[168] K. Kuroki, H. Usui, S. Onari, R. Arita, and H. Aoki, *Phys. Rev. B*, vol. 79, p. 224511, Jun 2009.

[169] H. Yamase and T. Agatsuma, *Phys. Rev. B*, vol. 102, p. 060504, Aug 2020.

[170] A. Aperis, P. Kotetes, G. Varelogiannis, and P. M. Oppeneer, *Phys. Rev. B*, vol. 83, p. 092505, Mar 2011.

[171] J. Bekaert, A. Aperis, B. Partoens, P. M. Oppeneer, and M. V. Milošević, *Phys. Rev. B*, vol. 97, p. 014503, Jan 2018.

[172] N. Barbero, S. Holenstein, T. Shang, Z. Shermadini, F. Lochner, I. Eremin, C. Wang, G.-H. Cao, R. Khasanov, H.-R. Ott, J. Mesot, and T. Shiroka, *Phys. Rev. B*, vol. 97, p. 140506, Apr 2018.

[173] D. Adroja, A. Bhattacharyya, P. K. Biswas, M. Smidman, A. D. Hillier, H. Mao, H. Luo, G.-H. Cao, Z. Wang, and C. Wang, *Phys. Rev. B*, vol. 96, p. 144502, Oct 2017.

[174] M. A. Albedah, F. Nejadsattari, Z. M. Stadnik, Z.-C. Wang, C. Wang, and G.-H. Cao, *J. Alloys and Compnds.*, vol. 695, pp. 1128 – 1136, 2017.

[175] J. Linder and A. V. Balatsky, *Rev. Mod. Phys.*, vol. 91, p. 045005, Dec 2019.

[176] V. L. Berezinskii *Pis'ma v Zhurnal Ehksperimental'noj i Teoreticheskoj Fiziki*, vol. 20, no. 9, pp. 628–631, Nov 1974.

[177] H. Kusunose, Y. Fuseya, and K. Miyake, *Journal of the Physical Society of Japan*, vol. 80, no. 4, p. 044711, 2011.

[178] A. Aperis, E. V. Morooka, and P. M. Oppeneer, *Annals of Physics*, vol. 417, p. 168095, 2020. Eliashberg theory at 60: Strong-coupling superconductivity and beyond.

[179] D. Kuzmanovski and A. M. Black-Schaffer, *Phys. Rev. B*, vol. 96, p. 174509, Nov 2017.

[180] A. M. Black-Schaffer and A. V. Balatsky, *Phys. Rev. B*, vol. 88, p. 104514, Sep 2013.

[181] A. Aperis, P. Maldonado, and P. M. Oppeneer, *Phys. Rev. B*, vol. 92, p. 054516, Aug 2015.

[182] C. Triola, J. Cayao, and A. M. Black-Schaffer, *Annalen der Physik*, vol. 532, no. 2, p. 1900298, 2020.

[183] A. Balatsky and E. Abrahams, *Phys. Rev. B*, vol. 45, pp. 13125–13128, Jun 1992.

[184] Y. Fuseya, H. Kohno, and K. Miyake, *Journal of the Physical Society of Japan*, vol. 72, no. 11, pp. 2914–2923, 2003.

[185] G. Sharma, M. Trushin, O. P. Sushkov, G. Vignale, and S. Adam, *Phys. Rev. Research*, vol. 2, p. 022040, May 2020.

[186] A. Fischer, L. Klebl, C. Honerkamp, and D. M. Kennes, *Phys. Rev. B*, vol. 103, p. L041103, Jan 2021.

Acta Universitatis Upsaliensis

Digital Comprehensive Summaries of Uppsala Dissertations from the Faculty of Science and Technology 2067

Editor: The Dean of the Faculty of Science and Technology

A doctoral dissertation from the Faculty of Science and Technology, Uppsala University, is usually a summary of a number of papers. A few copies of the complete dissertation are kept at major Swedish research libraries, while the summary alone is distributed internationally through the series Digital Comprehensive Summaries of Uppsala Dissertations from the Faculty of Science and Technology. (Prior to January, 2005, the series was published under the title "Comprehensive Summaries of Uppsala Dissertations from the Faculty of Science and Technology".)

ACTA
UNIVERSITATIS
UPSALIENSIS
UPPSALA
2021

Distribution: publications.uu.se
urn:nbn:se:uu:diva-451373